Pervaporation Using Graphene Oxide Membranes

by

Mindaugas Paulauskas

Submitted in accordance with the requirements for the degree of

Doctor of Philosophy

The University of Leeds

School of Chemistry

December 2015

Intellectual Property and Publication Statement

The candidate confirms that the work submitted is his own, except where work which has formed part of jointly-authored publications has been included. The contribution of the candidate and the other authors to this work has been explicitly indicated below. The candidate confirms that appropriate credit has been given within the thesis where reference has been made to the work of other.

Chapter 4 of this thesis contain theory and results presented by the author at the "2nd Fluid Flow, Heat and Mass Transfer" conference in Canada 2015.

Acknowledgements

This is thesis is one of the main outcomes of my 4 years integrated MSc and Ph.D. research activities at the University of Leeds in the Institute of the Process Research and Development (IPRD). During my studies a number of institutions and people have contributed to my research and I would like to take this opportunity to acknowledge all their good will. I would especially like to thank:

"*Lack of comfort means we are on the threshold of new insights.*"

Lawrence M. Krauss (1954, American Theoretical Physicist and Cosmologist)

Abstract

Pervaporation is a perspective fluid separation technology. Membranes are widely recognised for their energy and capital cost savings. Currently, most of the research is focused on developing new membrane material that are stable in a wide range of temperatures in a presence of organic solvents. This research is focused on a graphene oxide, a novel and highly selective membrane material. Graphene oxide has attracted a lot of academic research attention. Many researchers have demonstrated selective water removal using this material, however moving forward the data lack the scope and depth of understanding of the material performance at different process conditions and fluid systems.

Previous research has not addressed graphene oxide stability and performance in a wide range of conditions which are crucial for assessing the material's potential as a water selective membrane material for industrial applications. The purpose of this work is to investigate graphene oxide membrane pervaporation permeation flux and selectivity using common aqueous organic solvent solutions. Three industrial case studies are also investigated to determine whether the material is ready to be applied on a larger scale and has a potential to replace distillation. Previous research has also missed graphene oxide low price advantage, which stems from the cheap starting materials. This has been brought up and discussed in the final results chapter of the thesis.

The key outcome of this research is a demonstration of the graphene oxide pervaporation flux drop at elevated temperatures and the behaviour deviation from the solution-diffusion model. The membrane has also been rapidly fouled when exposed to aqueous peptide solutions. This research brings a large amount of experimental and analytical data, which points in a direction of the research avenues to be pursued in order to improve graphene oxide as a selective membrane material.

Table of Contents

List of Figures

List of Tables

Abbreviations

Abbreviation	Meaning
CRC Scheme	Carbon Reduction Commitment Energy Efficiency Scheme
BTSE	Bis(triethoxysilyl)ethane
DSC	Differential Scanning Calorimetry
DMF	Dimethylformamide
DMSO	Dimethyl sulfoxide
DMC	Dimethyl carbonate
EDX	Energy Dispersive X-ray
EtOH	Ethanol
FT-IR	Fourier Transform Infrared
GC	Gas Chromatography
G.O.	Graphene Oxide
GE	Gelatin
IPA	2-propanol
MTES	Methyltriethoxysilane
MeOH	Methanol
NRTL	Non-Random Two Liquid (model)
NMP	N-Methyl-2-pyrrolidone
PI	Process Intensification
PTFE	Polytetrafluoroethylene
PVA	Polyvinyl alcohol
PVDF	Polyvinylidene fluoride
RPM	Rotations per Minute
SEM	Scanning Electron Microscopy
TEOS	Tetraethyl orthosilicate
THF	Tetrahydrofuran
TGA	Thermogravimetric Analysis

Nomenclature

<div align="center">Variables</div>

Symbols	Units	Description
A	m^2	Surface area
$A_{antoine}$	bar	Antoine constant
$B_{antoine}$	bar K^{-1}	Antoine constant
$C_{antoine}$	K	Antoine constant
C_w	mol m^{-3}	Water molar concentration
$C_{G.O.}$	mg L^{-1}	Graphene oxide mass concentration
d	m	Spacing between graphene sheets
D_{wm}	$m^2 s^{-1}$	effective water diffusion coefficient in the membrane matrix
D_w	$m^2 s^{-1}$	Diffusion coefficient in the liquid boundary layer
E	N/A	Enrichment factor ($C_{w.P}/C_{w.B}$)
E_0	N/A	Enrichment factor without boundary layer (C_w/C_{wLM})
$E_{(Evaporation)}$	kJ	Energy required to evaporate water
$\dot{E}_{(transfer)}$	kJ s^{-1}	Thermal heat flow
$E_{pre-heat}$	kW	Energy required to preheat the process solution (thermal)
$E_{phase\ change}$	kW	Energy required to evaporate continuously fed water (thermal)
$E_{vacuum\ pump}$	kW	Energy required to run the vacuum pump (thermal)
E_{total}	kW	Total thermal energy
$\Delta H_{(Evaporation)}$	kJ kg^{-1} kJ mol^{-1}	Energy required to evaporate a set amount of water
J_v	$m^3 m^{-2} s^{-1}$ $m^3 m^{-2} h^{-1}$	Volumetric flux

J	kg m^{-2} s^{-1}	Mass flux
	kg m^{-2} h^{-1}	
k_m	kg m^2 s^{-1} bar^{-1}	Pressure normalised membrane mass transfer coefficient
	mol m^2 s^{-1} bar^{-1}	
k'_m	m s^{-1}	Pressure normalised membrane mass transfer coefficient
$k_{L.P.G.O.}$	kg m m^2 s^{-1} bar^{-1}	Pressure and membrane thickness normalised mass transfer coefficient
$k_{M.P.}$	kg m^{-2} s^{-1} bar^{-1}	Pressure normalised membrane mass transfer coefficient
	kg m^{-2} h^{-1} bar^{-1}	
k'_H	mol m^{-3} bar$_{-1}$	Product of the weight of the membrane / volume of adsorbed gas molecules and Henry's constant
$k`_{ov}$	m s^{-1}	Overall mass transfer coefficient
k'_{LM}	m s^{-1}	Liquid/membrane mass transfer coefficient
K_S^L	N/A	Liquid side partition coefficient
		$\rho_{w,ML} = K_S^L \rho_{w,LM}$
		(can also be used with molar concentrations)
K_S^G	mol bar^{-1}m^{-3}	Membrane side partition coefficient
	kg bar^{-1}m^{-3}	$\rho_{w,MS} = K_S^G P_{w.p}$
K	N/A	Adjustable parameter
k'_L	m s^{-1}	Liquid mass transfer coefficient
m	kg, g, mg	Mass of the collected permeate sample
Mi	kg mol^{-1}	Molecular weight of the component
N_t	m^{-2}	Total number of pores per effective area
n_f	mol s^{-1}	Overall mole flow velocity
$n_{permeate}$	mol s^{-1}	Permeate mole flow velocity
$P_{atmospheric}$	bar	Atmospheric pressure
$P_{permeate}$	bar	Permeate pressure

$P_{process}$	bar	Process pressure
P^*	bar	Saturated water vapour pressure
P	bar	Pressure drop
P_1	bar	Pressure at the start of the pore
P_2	bar	Pressure at the end of the pore
$P_{W.L}$	bar	is the partial vapour pressure of water in equilibrium with the feed liquid
$P_{w.P}$	bar	Water vapour partial pressure in the permeate
Q_{liquid}	mol m^{-2} s^{-1}	Molar liquid flux
Q_{vapour}	mol m^{-2} s^{-1}	Vapour molar flux
$Q_{surface}$	mol m^{-2} s^{-1}	Vapour molar flux across the surface of the pore
$Q_{w.vapour}$	mol m^{-2} s^{-1}	Water vapour molar flux
$Q_{org.vapour}$	mol m^{-2} s^{-1}	Organic compound vapour molar flux
Q_{Total}	mol m^{-2} s^{-1}	Total molar flux
R	bar m^3 K^{-1} mol^{-1}	Ideal gas constant, $8.31445*10^{-5}$
R_{total}	s m^{-1}	Total mass transport resistance
R_{liquid}	s m^{-1}	Liquid phase mass transfer resistance
$R_{membrane}$	s m^{-1}	Membrane mass transfer resistance
$R_{support}$	s m^{-1}	Membrane support mass transfer resistance
r	m	Mean pore diameter
T_{perm}	K	Permeate temperature
t	s, min, h	Time, units of time are noted in calculations
t_a	m	Thickness of the adsorbed gas layer onto a membrane
T	K	Temperature
$U_{(Overall)}$	kW m^{-2}K^{-1}	Overall heat transfer coefficient, Assumed
u	m s^{-1}	Liquid velocity
$V_{G.O.}$	L	Volume of the graphene oxide solution

V_{mol}	m^3	Molar volume
v	$m\ s^{-1}$	Convective velocity
x	N/A	Mole fraction in the liquid phase
x^*_w	N/A	Equilibrium liquid water mole fraction
X	$mol\ bar^{-1}s^{-1}\ m^{-1}$	Combined Pore-Flow model coefficient
$X_{mixture}$	$mol\ bar^{-1}s^{-1}\ m^{-1}$	Combined Pore-Flow model coefficient of a mixture fluid
Y_1, Y_2	$mol\ m^{-3}$	Liquid boundary layer integration constants
Y_{M1}, Y_{M2}	$mol\ m^{-3}$	Membrane boundary layer integration constants
y^*_w	N/A	Equilibrium vapour water mole fraction
y	m	Selected position in the boundary layer
y_a	m	Liquid filled part of the membrane
y_b	m	Vapour filled part of the membrane
y_0	m	Start of the liquid boundary layer
y_l	m	Liquid boundary layer thickness
y_m	m	Membrane layer thickness
y_p	m	Membrane support layer thickness (permeate side)
Z	$mol\ bar^{-2}s^{-1}\ m^{-1}$	Vapour transport coefficient
Z_w	$mol\ bar^{-2}s^{-1}\ m^{-1}$	Water vapour transport coefficient (Pore-Flow model)
Z_{org}	$mol\ bar^{-2}s^{-1}\ m^{-1}$	Organic compound vapour transport coefficient (Plug-Flow model)
	Variables (Greek)	
α	N/A	Membrane selectivity coefficient
γ_i	N/A	Activity coefficient of the component
γ_{gas}	N/A	Adiabatic gas expansion coefficient
η	$kg\ s^{-1}\ m^{-1}$	Fluid viscosity

η_G	kg s^{-1} m^{-1}	Adsorbed gas onto a surface viscosity
η_{vac}	N/A	Vacuum pump efficiency
Θ	°	X-ray angle
λ	N/A	Auxiliary function coefficient
λ_l	m	Wavelength
μ	J mol^{-1}	Chemical potential
ρ	kg m^{-3}	Liquid density
ρ_w^L	kg m^{-3}	Water mass concentration in the liquid
χ	N/A	Membrane tortuosity

Variables (Superscripts)

G	Gas
L	Liquid

Variables (subscripts)

B	Bulk
i	Component "i"
P	Permeate
SM	Support/membrane interface
ML	Membrane/liquid interface
LM	Liquid/membrane interface
MS	Membrane/support interface
W	water
Org	Organic component

Dimensionless groups and their definitions

N_{KN}	$\dfrac{\sigma_S}{d_p}$	Knudsen number
Pe	$\dfrac{J_v\, y_l}{D_w}$	Peclet number

1   Introduction

An increase in the global temperature and dwindling fossil fuels over the last several decades have led to the introduction of a new government legislation to combat the depletion of these valuable resources.[4] In the UK, the "Carbon Reduction Commitment Energy Efficiency Scheme" also known as the "CRC Scheme" was designed to improve energy efficiency in large public and private sector organisations. The main target of the scheme is to achieve 80% reduction in UK carbon emissions by 2050.[5] This has fuelled engineering research to focus on the development of more sustainable chemical processes.

Process intensification (PI) is a common strategy used in the chemical manufacturing industry to reduce energy usage.[6] One of the aims of PI is to increase the efficiency and competitiveness of a process. Another aim is to create a faster and more environmentally friendly processing variant by implementing or designing new technology.[7] Membrane driven separation processes match the target criteria set out by the PI principles and have been shown to result in significant energy and capital cost savings when compared to their counterpart chemical process unit operations.[7, 8] The advantages of membrane separations made legislator bodies recognise it as the best available technology (BAT).[9] The main applications of membrane processes typically involve separation of: gas mixtures, oil/water treatment, separation of organic/organic and organic/water mixtures.[10]

Membranes are categorised based on their nominal pore sizes. Classification of common membrane groupings is shown in Figure 1. Microfiltration, ultrafiltration and reverse osmosis membrane processes are well established with many different applications. Membranes in these categories are provided by multiple experienced companies.[11] Microfiltration separates small colloidal particles and bacteria within a range of 0.1-10 μm in diameter. Ultrafiltration pore size is tailored to separate dissolved macromolecules such as proteins. Reverse osmosis is mainly focused on desalination of brackish water.[12] Pervaporation/Gas separation is the most recent membrane separation category. Numerous plants are being installed worldwide, the market size is expanding and process innovations are being made.[11] Pervaporation is considered as the main technology which has potential to replace azeotropic distillation process.[11, 13] Currently, pervaporation research is focused on novel membrane materials, which exhibit high permeate selectivity and high permeate fluxes.[14]
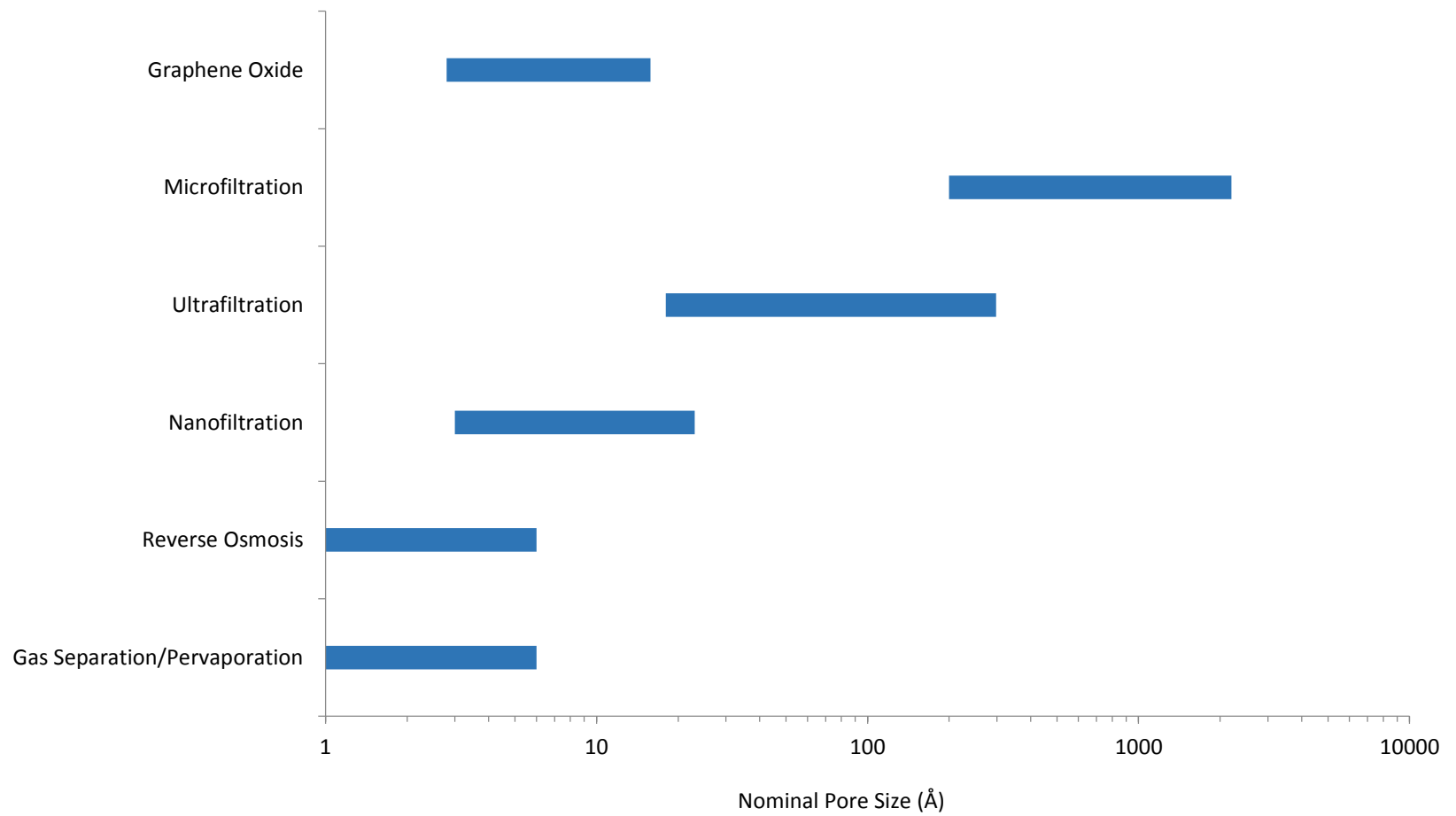
Figure 1 - Membrane classification based on the nominal pore sizes (Membrane technology and applications)

1.1 Research Strategy and Motivation

In light of the huge potential benefits which pervaporation might bring to selective fluid separations, research is focused on cheap, selective and highly permeable graphene oxide (G.O.) membrane material.[1] The main aim of this study was to investigate its applicability for large–scale pervaporation. The research was carried out in 4 stages. These stages are summarised in the following section and are also shown in a flow chart in Figure 2.

Stage 1

The first research stage was dedicated to the development of the two most fundamental parts of the pervaporation research: i) G.O. membrane and ii) Pervaporation reactor. The development of the membrane is a crucial part of the research, with various factors having been shown to influence the quality of membrane surface formation. Such examples include: differential pressure in the filtration, G.O. concentration, and type of support used.[15-17] In parallel to the membrane production, a membrane testing cell was designed and built with the following properties: i) accommodates G.O. membranes without damaging the surface, ii) stable over a wide range of temperatures, iii) compatible with organic solvents and corrosive fluids at elevated temperatures, iv) has control over vessel hydrodynamics, and v) holds a vacuum.

Stage 2

The second stage of the research involved the assembly of a fully functional conventional pervaporation setup. During this part, a laboratory scale pervaporation process was constructed which was designed to deliver reliable pervaporation data. After the successful launch of the pervaporation process, the influence of hydrodynamic conditions on the permeation flux and membrane separation performance was determined. The study was used to define the hydrodynamic conditions required to measure the rate of water permeation limited by the membrane permeability.

Stage 3

The main aim of this research stage was to acquire pervaporation flux and separation performance for common organic/water solvent systems. The organic solvents were selected based on their frequent usage in the chemical Industry: ethanol (EtOH) which is a potential biofuel, 2-propanol (IPA) which is a common organic solvent and reagent, and tetrahydrofuran (THF), a common solvent in the pharmaceutical industry. The membranes were characterised using the following analytical techniques: Scanning Electron Microscopy (SEM), Energy Dispersive X-ray Spectroscopy (EDX), Fourier

Transform Infrared (FT-IR), Differential Scanning Calorimetry (DSC), Thermal Gravimetric Analysis (TGA), X–ray Diffraction (XRD), and surface contact angle measurements.

Stage 4

The final stage of the research focussed on commercial applications. Multiple industrially relevant fluid separations were studied over a range of temperatures and water concentrations. A computational model based on the G.O. permeability data was constructed. The model estimates the required surface area of the membrane module based on the process conditions and the membrane thickness. The azeotropic IPA/water distillation process was simulated and the energy usage was compared to the pervaporation process.
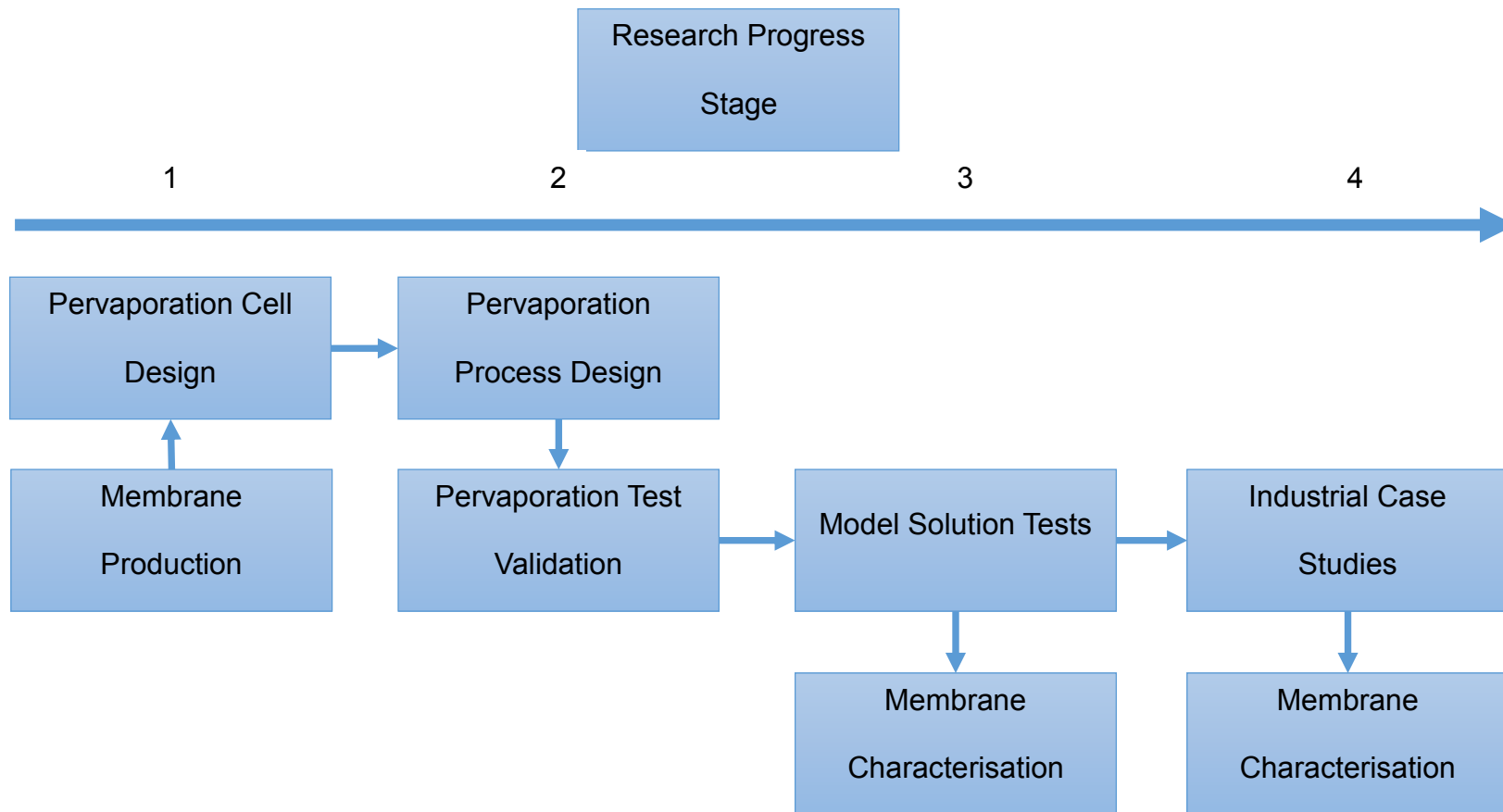
Figure 2 – Research Progress Flow Chart

1.2   Membrane Materials

Currently, research is concentrated on membrane development with the aim of improving (i) material's resistance to various solvents (THF, *N*-methyl-2-pyrrolidone (NMP)), ii) material's resistance to acid, (iii) mechanical strength, (iv) pervaporation flux and (v) separation selectivity.[14, 18, 19] To objectively compare membrane performance in the literature review several key concepts have to be defined. Typically, pervaporation data is presented in a form of flux, which is a product of a pervaporation constant and a driving force, .Equation 1. In the pervaporation flux equation the pressure on the process side is usually low and the term is frequently ignored. While flux provides very useful membrane performance information it can be misleading when comparing different membrane performance at different temperatures and water compositions.[20] Membrane permeability is a component mass/mole flux normalised with respect to the membrane thickness and the driving force Equation 2. This factors out the influence of the different water concentrations, temperatures and membrane thicknesses among different tests and is one of the best ways to compare different selective materials. If the membrane thickness is not known component mass/mole permeance is calculated, which is a component flux normalised with respect to the driving force Equation 3. These expressions accounts for different water concentrations and pervaporation temperatures. Membrane selectivity is another important parameter to be considered. It is defined as a ratio of the component permeances Equation 4.

$$Q_{vapour} = k_m(P_{w.L} - P_{w.P})$$
Equation 1

$$\frac{Q_{vapour}\, y_m}{(P_{w.L} - P_{w.P})} = D_{wm} K_S^G = \text{Permeability}$$
Equation 2

$$\frac{Q_{w.vapour}}{(P_{w.L} - P_{w.P})} = \frac{D_{wm} K_{s.mol}^G}{y_m} = \text{Permeance}$$
Equation 3

$$\alpha = \frac{\text{Permeance (water)}}{\text{Permeance (organic)}}$$
Equation 4

Where, Q_{vapour} is vapour molar flux (mol m^{-2} s^{-1}), k_m is pressure normalised membrane mass transfer coefficient (mol m^2 s^{-1} bar^{-1}), y_m is membrane thickness (m) and D_{wm} is effective water diffusion coefficient in the membrane matrix (m^2 s^{-1}) $K_{s.mol}^G$ is gas sorption coefficient (mol bar^{-1}m^{-3}), $P_{W.L}$ is the partial vapour pressure of water in equilibrium with the feed liquid (bar), $P_{w.P}$ is the permeate water vapour pressure (bar).

The membrane chemical resistance is usually determined by exposing the membrane to chemical environments expected in an industrial operation. This is followed by a careful

examination of the surface disintegration, pervaporation flux and selectivity change. The mechanical strength of a membrane is frequently tested by measuring the material stiffness and tensile strength.[21]

1.2.1 Polymeric Membrane

The first polymeric membrane use in pervaporation can be traced back to the early 20th century. It was discovered that distilled alcohol placed in a cellophane bag and left in air turned into absolute alcohol.[22]

Since then, many different polymeric membranes with high selectivity for water have come into existence. One of the most common commercial membranes is made out of polyacrylonitrile coated with a layer of cross-linked poly(vinyl) alcohol which is applied in alcohol dehydrations.[18] High water fluxes have also been demonstrated by membranes composed of cellulose, Nafion, and grafts of poly(vinyl pyrrolidone) on teflon and polyacrylonitrile.[23]

Polymers are known to be mechanically weak compared to inorganic materials[24] which limits their application range. Strength can be improved by cross-linking the structure with various additives or blending several different polymers. Alternatively, the membrane can be thermally treated to increase the level of crystallinity in the polymer matrix.[23, 25] Unfortunately, the increase in structural integrity usually leads to a decrease in water permeation flux and an increase in membrane brittleness, thus both cross–linking and thermal treatment should be controlled.[23]

Yang *et.al.* (2000) have prepared a blend of cellulose and alginate, which was cross-linked by Ca^{2+}. The membrane demonstrated an increase in tensile strength while preserving water permeation flux and selectivity.[26] Xianshe *et al*. studied sericin/PVA blend membranes cross–linked by dimethylolurea. As expected, cross–linked membranes had high water selectivity and were able to concentrate 8.5wt% water in the process solution to 94wt% in the permeate. These membranes were compared to a blend of sericin and PVA without a cross–linking agent, which were only thermally annealed at 120°C for 30 minutes. Thermally annealed membranes demonstrated lower performance in terms of water selectivity and were able to increase water concentration from 6wt% in the feed to 82wt% in the permeate.[27]

A major drawback in polymeric membranes is poor resistance to different organic solvents at elevated temperatures.[28] Livingston, *et al.* have investigated polyimide membrane stability in organic solvents and demonstrated that the polyimide without cross-linking agent dissolved in NMP, dimethylformamide (DMF) and dimethyl sulfoxide (DMSO). The polymer was successfully redesigned with cross-linking agents to

withstand the organic solvents.[29] Typical polymeric membrane pervaporation rates are shown in Table 1.

Table 1 – Dehydration of alcohols using polymeric membranes [23, 30, 31]

Mixture (mass ratio)	Support	Separation layer	Cross-linker or modification	Separation factor	Permeance (kg m^{-2} h^{-1} bar^{-1})	Reference
EtOH/H_2O (50/50)	PVA	PVA	Amic acid	100	3.5	[32]
EtOH/H_2O (90/10)	Chitosan	Chitosan	H_2SO_4	1791	5.15	[33]
EtOH/H_2O (80/20)	PVA	PVA	Fumaric acid	211	2.32	[34]
EtOH/H_2O (90:10)	Nylon-4	Nylon-4	N/A	4.5	249	[35]
EtOH/H_2O (90:10)	Sodium alginate (Na-Alg)/PVA	Na-Alg/PVA	N/A	30,000	2.12	[36]
IPA/H_2O (90:10)	PVA/chitosan 20:80	PVA/chitosan 20:80	Glutaraldehyde and thermal cross-link	9,000,000	8.59	[31]

1.2.2 Inorganic membranes

Inorganic membranes are typically made from silica (SiO_2) and (α,γ)-alumina (Al_2O_3).[14] The construction of such a membrane usually consists of two parts: the support and the separating layer. The support is made out of a single plate, hollow-fibre or honeycomb structure ceramics, and the separating layer can be composed of porous or dense structure made out of single phase or composite ceramics. The pore sizes are split into several categories: microporous (<2nm), mesoporous (2-50nm) or macroporous (>50nm), which are selected based on the application.[37, 38]

Studies show that ceramics are thermally stable materials with melting points of over 1000°C and are can operate in any organic solvent over a wide pH range.[14, 30] Furthermore, it is demonstrated that an inorganic membrane permeation flux increases with temperature while retaining inherent material high selectivity for water.[30, 39]

Interest in using inorganic membranes has recently increased, due to the commercialisation of the narrow pore size distribution ceramic membranes.[30] It is thought that the advantages of longer lifetime and higher temperature tolerance brought about by the inorganic materials can compensate for their higher module costs compared to their polymeric counterparts on an industrial scale.[40] Table 2 shows typical membranes used in alcohol dehydrations.

Table 2-Dehydration of alcohols using inorganic membranes

Mixture (mass ratio)	Support	Separation layer	Separation factor	Permeance (kg h^{-1}m^{-2} bar^{-1})	Reference
EtOH/H$_2$O (91:9)	γ-Alumina	Silica	50	2.71	[41]
IPA/H$_2$O (90:10)	α-Alumina	Silica/zircoinium 10 mol%	300	4.84	[42]
EtOH/H$_2$O (95:5)	α-Alumina	Al$_2$O$_3$:SiO$_2$:Na$_2$O:H$_2$O 1:2:2:120, zeolite NaA	16,0000	10.48	[43]
EtOH/H$_2$O (95:5)	Mullite, Al$_2$O$_3$, cristobalite	NaA Zeolite	>5000	10.21	[44]

1.2.3 Mixed matrix and hybrid materials

Mixed matrix membranes contain an inorganic compound, which is locked into a polymer matrix. Typically, an inorganic material improves the mechanical properties of the membrane and diminishes the free volume in the polymer matrix through which molecules may diffuse. Usually, mixed matrix membranes are made from polyvinyl alcohol (PVA) doped with inorganic material (clay, zeolite, tetraethyl orthosilicate (TEOS)).[14]

Hasegawa *et al.* (2010) investigated zeolite membrane stability in the presence of the sulphuric acid and found that even slightly acidic conditions destroyed membrane separation ability.[45] Currently, the lowest pH level of ≈ 2 can be tolerated by the commercial HybSi membrane.[46] A list of permeation fluxes and selectivities of mixed matrix and hybrid material membranes is shown in Table 3. Private communications with industry have drawn attention that the pH tolerance and mechanical properties of current membranes are not good enough for large-scale membrane processes in the field of speciality chemicals and further improvements in these areas have to be made.

Hybrid materials are made by crosslinking organic fragments with inorganic materials into one uniform matrix. For example, HybSi membranes hybrid nature lies in the fact that each silicon atom is connected not only to oxygen, as in the regular silica material, but also to an organic fragment. The organic part functions as a bridge between other silica atoms.[47] The stable structure given by the hybrid material allows the membrane to withstand various organic solvents without swelling or losing selectivity.[48]

Recently, hybrid membranes composed of methyltriethoxysilane (MTES) and bis(triethoxysilyl)ethane (BTESE) were commercialised by Pervatech BV.[46] Precursors used to make the HybSi membrane selective layer are shown in Figure 3.

BTESE   MTES
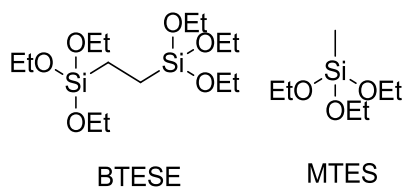
Figure 3-Precursors used for the HybSi membrane

Van Veen *etal.* have demonstrated HybSi membrane performance, in the presence of 3% water and 97% n-butanol, in over 1000 days of operation at 150°C.[46] The membrane retained the selectivity over the whole experimental period, and stability

during the shutdown and start-up operations also remained constant. The membrane was stable in aqueous nitric acid solutions down to pH 2.3.

Table 3 - Dehydration of alcohols using mixed matrix or hybrid membranes

Mixture (mass ratio)	Support	Separation layer	Separation factor	Permeance ($kg\,h^{-1}m^{-2}\,bar^{-1}$)	Reference
EtOH/H_2O (80:20)	PVA with 11wt% NaX zeolite	PVA with 11wt% NaX zeolite	8.5	4.73	[49]
EtOH/H_2O (90:10)	PVA with 5wt% γ-aminopropyl-triethoxysilane (APTEOS)	PVA with 5wt% (APTEOS)	1580	1.415	[50]
IPA/Water (90:10)	Chitosan with 40wt% TiO_2	Chitosan with 40wt% TiO_2	4728	6.87	[51]
EtOH/H_2O (85:15)	PVA with TEOS (cross-linked at 160 ℃)	PVA with TEOS	329	1.2	[52]

1.3 Industrial use of pervaporation

Pervaporation process scale–up has many challenges. Problems mainly arise from the distribution of physical variables: pressure, temperature and fluid flow.[11] In addition, the quantity of the process solution increases dramatically, which impacts on process safety, size of equipment used and the time required to carry out an experiment or industrial operation. A conventional pervaporation process scale–up procedure can be subdivided into the following steps[53]:

1. Define the fluid system of interest
2. Set economic targets
3. Identify the membrane capable of separating the components
4. Demonstrate the separation on a small scale
5. Conduct a pilot–plant study
6. Demonstrate long term performance
7. Design large scale pervaporation unit based on the collected information
8. Build a commercial system

The first large–scale pervaporation process using tubular NaA zeolite membranes was built in 1999. The plant consisted of 16 pervaporation modules; each module composed of 125 tubes with 12 mm outside diameter and 80 cm in length, resulting in a total surface area of $\approx$ 60 m^2. The process was designed to deliver i) EtOH, ii) IPA, and ii) MeOH solvents with less than 0.2wt% water in the final solution. The industrial operation was set to operate at 120°C with 10wt% water in the initial process solution. [54]

Process trials were run at $\approx$ 600 L h^{-1} flow rate using 10wt% water in IPA. The large-scale results were very similar to the design specifications apart from the permeate water concentration. It was estimated that the average water content in the permeate will be $\approx$78wt%. The large–scale membrane operation delivered an average of 70wt% water on the permeate side; this indicates a significant loss of alcohol to the permeate side, which will impact on the process economics. This also indicates a need to develop a more selective membranes at low water concentration.[54]

Esters have a wide range of applications such as coatings, adhesives, perfumes and plasticizers.[55] Due to high demand, the production is carried out on a multi-ton scale worldwide. Esterification reaction conversion is limited by a chemical equilibrium. In industry, reaction equilibrium is usually shifted towards product formation by adding an excess reactant or continuously removing one of the reaction products from the solution.[56]

Waldburger and Fritz have compared the production of ethyl acetate between the conventional and a membrane-assisted process. The traditional process contained one reaction distillation column, two azeotropic distillation columns, several condenser-mixers and a settler

Figure 4 (a).[56] The continuous membrane assisted esterification unit consisted of three pilot plant scale loop tube membrane reactors

Figure 4 (b).
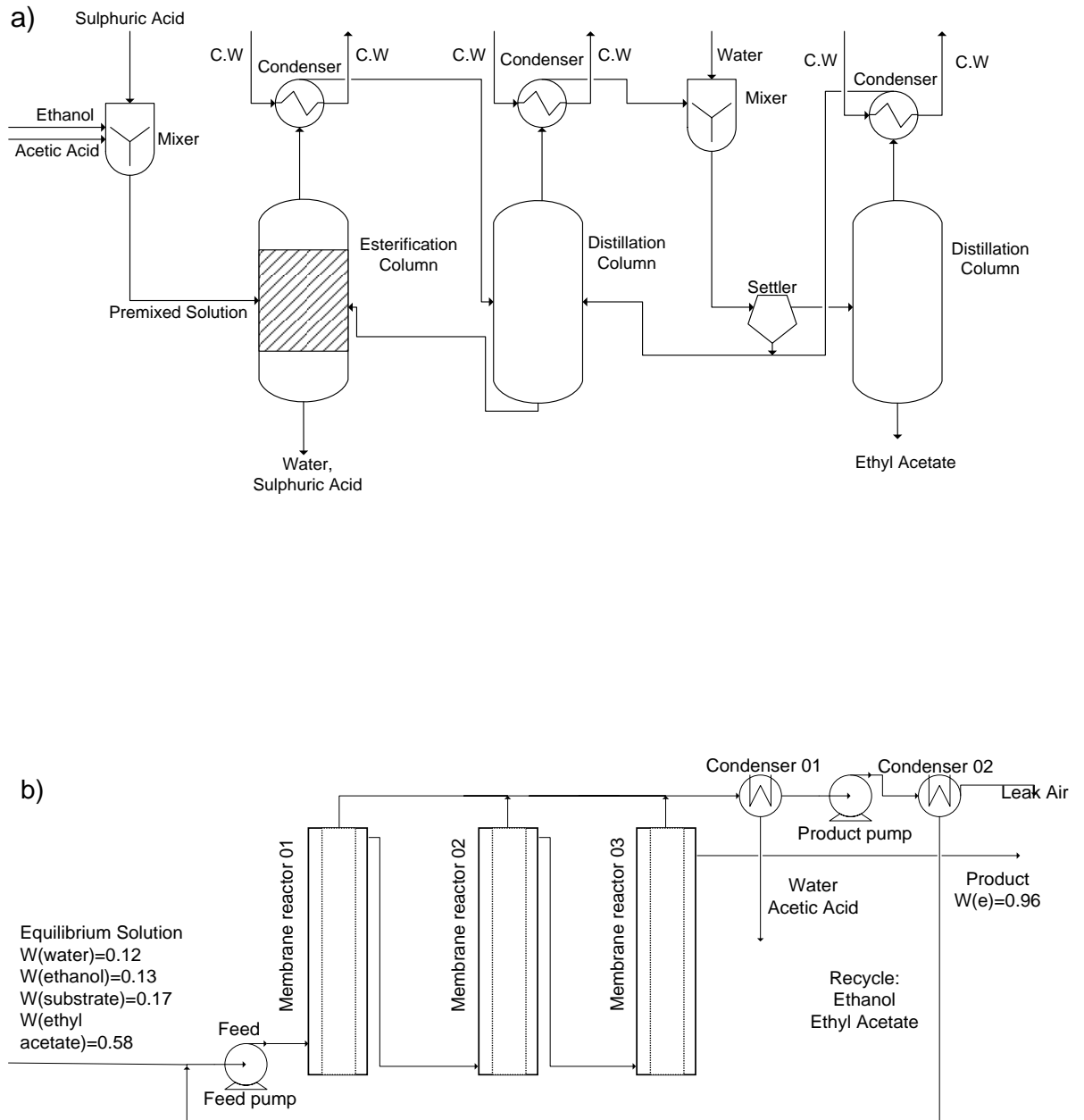
Figure 4 – a) Conventional ethyl acetate production, b) membrane assisted ethyl acetate production
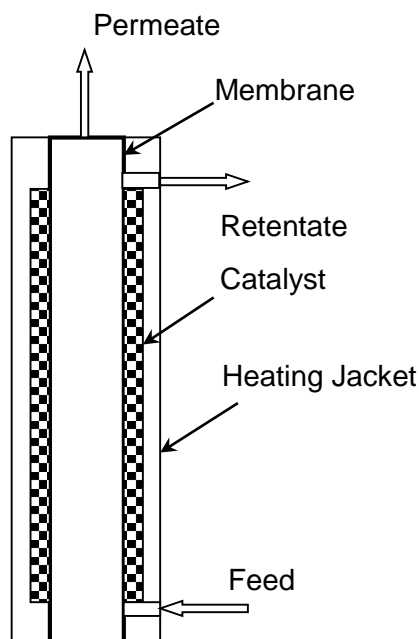
Figure 5 - Membrane reactor

The membrane reactor was constructed as a concentric set of tubes welded together Figure 5. A polyvinyl alcohol membrane was used to selectively remove water from the process liquid. Heterogeneous ion exchange polymer catalyst was placed between the membrane and the heating jacket. The yield of ethyl acetate was optimised by changing the following variables: flow rate, temperature and permeate pressure. The reaction yield at the optimum conditions increased from the equilibrium conversion of 71% to 98.7%.[56]

The group also compared the economic aspects of these two processes, with the simulation based data showing that the pervaporation assisted esterification using polyvinyl alcohol membranes, with an assumed lifetime of one year, can offer an energy input reduction reaching 75% and cuts in capital investment and operating costs as high as 50%.

Waldburger and Fritz have identified several other reactions which may benefit from this technology: ethers, enamines, Schiff bases, acetals, ketals, alcoholates, enzyme catalysed reactions and separation of racemates by stereoselective esterification.[56]

1.4   G.O. a selective membrane material

G.O. is a modern water selective membrane material. On a fundamental level, it is a mono-layer-thick and two-dimensional nanomaterial; the exact chemical structure of G.O. has been debated for decades. The debate has mostly focused on the types and distribution of the functional groups anchored to the basal plane.[57] In recent years, a generic model has been proposed by Lerf–Klinowski, which has been widely accepted

by the scientific community, Figure 6. [57, 58] The material structure was determined by several different techniques: i) solid state nuclear magnetic resonance (NMR) spectroscopy,[59] ii) elemental analysis, iii) X-ray diffraction analysis, iv) FT-IR spectroscopy [60] and iv) material reactivity.[57] The molecule is decorated with oxygen containing groups such as: epoxy, hydroxyl and carboxylic acid.[60, 61] Large amounts of oxygen on the basal plane of the G.O. typically results in a 2 to 3 C/O ratio.[60]
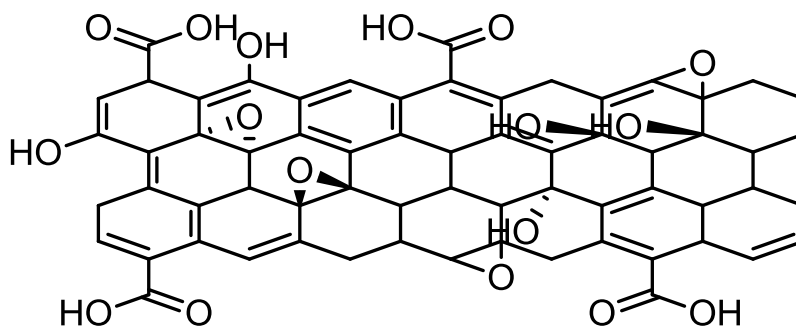
Figure 6 –Variation of the Left-Klinowski G.O. model [57]

Oxygen functional groups decorating the graphene sheet gives a set of unique properties to the material. It allows G.O. to produce stable suspensions without stabilising agents in water and other organic compounds such as DMSO, THF and N-Methyl-2-pyrrolidone (NMP).[62] The stable suspension gives an opportunity for easy production of thin graphene oxide assemblies.[58] A high concentration of functional groups on the G.O. surface produce amorphous regions which result in nanoscale wrinkles and surface defects of large G.O. assemblies. These surface features provide primary entry points for the water molecules between the G.O. sheets.[3]

Initially, selective water transport through G.O. was attributed to the frictionless flow of a monolayer of water through a two dimensional capillary formed by two parallel graphene sheets, spaced with the help of oxygen containing functional groups. The permeation of other molecules was assumed to be hindered by water clogging up the capillaries and the G.O. sheet narrowing at low humidity conditions.[1, 63] More recently, it was proposed that the water transport across a G.O. membrane predominantly occurs *via* the following routes: i) interlayer, ii) interedge spaces, iii) wrinkles and iv) pores or defects introduced to graphite by the oxidation process, Figure 7. Recent molecular dynamic simulations showed that while oxygen groups on the basal plane indeed act as an intersheet spacers, they also reduce the rate of water transport across the G.O. membrane by interacting with the water molecules *via* hydrogen bonding.[64] The molecular simulations were supported by experimental evidence where copper hydroxide nanostrands were introduced to act as sheet spacers instead of oxygen functional groups. The membrane was tested in a nanofiltration mode before and after the reduction of the functional groups by hydrazine. The reduced membrane exhibited significantly better performance, thus indicating the negative effects of the oxygen functional groups on the rate of permeation. [64] Another property which influences water permeation through a G.O. membrane is the materials sensitivity to the water concentration in the fluid.[1] A significant interlayer expansion was observed and measured when G.O. was exposed to water or organic liquids.[63] G.O. membrane and graphite powder were placed in water/EtOH solution at different water concentrations and the interlayer spacing was monitored by synchrotron X–ray diffraction. The spacing decreased linearly from 12.3 Å at 90vol% water in ethanol to 9.3 Å at 10vol% water in
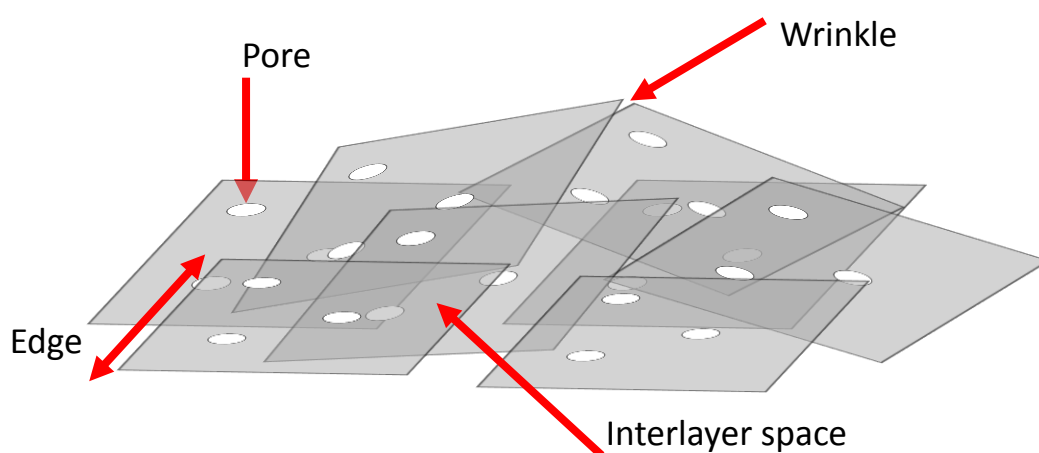
Figure 7 – Simplistic representation of a G.O. membrane stacking and potential water entrance points[3]

ethanol. Interestingly, at 100vol% ethanol, the interlayer spacing increases to 10 Å. The change in interlayer expansion/contraction was attributed to the varying number of water monolayers intercalating G.O. material at different concentrations. This could explain the varying rate of water permeation with respect to the relative humidity studied previously.[1, 63]

To get a complete in depth model of water permeation through a G.O. membrane is very challenging. The main issue stems from the aforementioned lack of understanding of the exact G.O. chemical structure. Furthermore, a full permeation model should take into account the physical microstructure of the material such as: sheet size, layer-by-layer stacking, pores and wrinkles of the surface, which are difficult to define and vary among membranes.[3]

1.4.1   Membrane manufacturing

An overview of the individual steps necessary for the production of G.O. membranes is provided below and shown in the Figure 8. Typically, graphite powder is oxidised using Hummer's method [57], followed by exfoliation of the graphite powder using sonication in deionised water. The suspension can then be coated on a wide range of ceramic or polymeric supports by spray, spin, or filtration coating techniques.[1, 16, 58, 65] The resulting film is water selective graphene oxide membrane.

Figure 8 – Overview of the G.O. membrane production process

1.4.2 Brodie's Method

The first graphene oxide was produced in 1859 by a British scientist while he was investigating the structure of graphite. [66] One of the reactions involved adding "potash chlorate", potassium chlorate ($KClO_3$), to a slurry of graphite and nitric acid. The success of the oxidation was determined by measuring the product weight increase after the reaction and separation. After 5 consecutive oxidation repeats the weight had stopped increasing and the graphite was deemed to be fully oxidised. The graphite oxide was able to disperse in deionised water and alkaline solutions, but did not dissolve in acids.[66]

1.4.3 Hummers Method

In 1957, Brodie's method was improved by S. Hummer and E. Offeman. The concentrated nitric acid was replaced by sulphuric acid and the oxidising agent, potassium chlorate, was replaced by potassium permanganate ($KMnO_4$). [67] The exact mechanism of the oxidation is still not clear, however it is postulated that the oxidative species, dimanganese heptoxide **1**, Scheme 1, intercalates between graphite plates and oxidises the basal plane of the graphene.

$$KMnO_4 \ + \ 3H_2SO_4 \longrightarrow \ \overset{\oplus}{K} \ + \ \overset{\oplus}{MnO_3} \ + \ \overset{\oplus}{H_3O} \ + \ 3\overset{\ominus}{HSO_4}$$

$$\overset{\oplus}{MnO_3} \ + \ \overset{\ominus}{MnO_4} \longrightarrow \ Mn_2O_7$$
$$\mathbf{1}$$
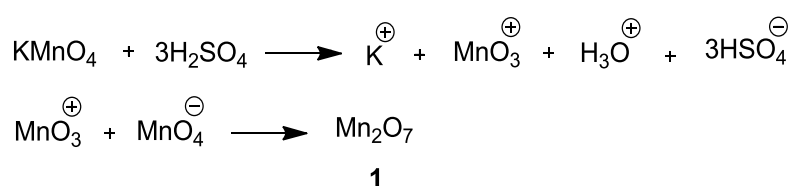
Scheme 1-Dimanganese heptoxide formation[57]

Dimanganese heptoxide is a more reactive form of the potassium permanganate, which is known to explode if heated above 55°C or in contact with organic materials. Therefore, the process temperature has to be strictly monitored during the oxidation.[57, 67] The resulting graphite oxide exfoliates in water very well with the help of a sonic bath.[1, 61]

1.4.4 Improved Hummers method

A recent explosion in graphite research has also led to improvements in G.O. synthesis. Improved methods are based on the previously described Hummer's method.[68, 69] The main improvement involves excluding sodium nitrate ($NaNO_3$) [69] and introducing phosphoric acid into the mixture.[68] The exclusion of $NaNO_3$ eliminated the production of toxic gases without loss of the oxidation in terms of functionality and overall yield.[69]

1.4.5 Coating

The coating procedure is a crucial part of the membrane manufacturing process. Initial G.O. membrane research conducted at the University of Manchester used spin and spray coating techniques on a heated 25 µm copper foil to produce a uniform G.O. membrane layer. Later, the copper foil was chemically etched away to expose a free standing G.O. layer for experimentation.[1]

By far the most common coating procedure is vacuum filtration, with this technique being used by a large number of researchers for G.O. membrane preparation Figure 9.[16] The method involves a three-piece vacuum filter. The G.O. suspension is loaded in the top part of the apparatus and is allowed to pass through a support. The filtration differential pressure is usually kept at approximately 1 atm.
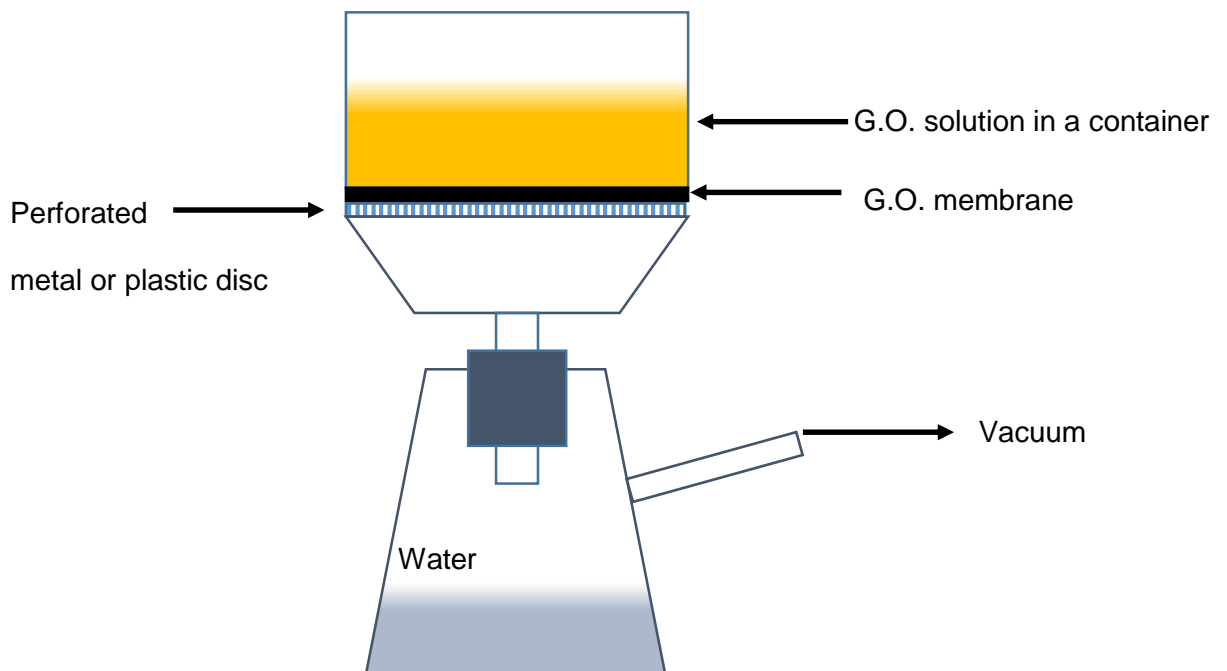
Figure 9 – Typical three piece vacuum filter

1.5 G.O. Membranes Selective Water Separations

The first recorded graphite oxide use as a water selective membrane was published in a patent in 1969. The graphite oxide was prepared using Hummers method, but not exfoliated by sonication. Instead graphite oxide was used it its particle form to produce a thin film on cellulose paper. The thin graphite oxide layer was then coated with a cyanoethylated polyvinyl alcohol polymer and post process baking at 150°C for 30 min. The resulting 5 μm membrane was tested in a reverse osmosis laboratory apparatus at ≈ 69bar trans- membrane pressure using 3.5wt% NaCl solution. The membrane selectivity was low with 72% of salt going through the membrane. After 24h operation a sample was taken and an average pervaporation flux was estimated as 1.1 L $h^{-1}m^{-2}$.[70]

1.5.1 Polymer supported and free standing G.O. membranes

In 2012, Nair et al. exfoliated graphite oxide in water and produced graphene oxide suspension. The suspension was then used to produce a graphite oxide thin film on a copper metal surface. The copper was chemically etched away, which exposed a freestanding membrane. The membrane was used in vapour permeation tests of various liquids and gases at a room temperature.

Initial tests were conducted on a submicrometer thick G.O. membrane at room temperature using helium and hydrogen gas. The experimental setup is shown in Figure 10 a). Helium permeation was studied using a mass spectrometer. The permeation experiments showed no detectable loss of helium, thus the rate of permeation was assumed to be lower than the accuracy of the mass-spectrometer, which resulted in an estimated rate of permeation of $3.6*10^{-8}$ kg $h^{-1}m^{-2}bar^{-1}$. A 12 μm thick polyethylene terephthalate film was used as a reference barrier. The leakage rate resulted in $3*10^{-5}$ kg $h^{-1}m^{-2}bar^{-1}$ the rate of permeation, which was ≈ 833.3 times higher. Similar results were found using hydrogen gas with no meaningful rate of permeation measured; although it has to be noted that the accuracy of detection was three orders of magnitude lower.[1]

To test liquid vapour rate of permeation the experimental setup was changed, Figure 10 b). The vapour permeation was measured by recording the weight loss of the vessel placed on a computerised balance. A vessel covered with a 1 µm thick G.O. film did not show any weight loss after several days for hexane, acetone, decane, propanol and interestingly ethanol; with a detection limit of 1 mg. However, a large weight loss was
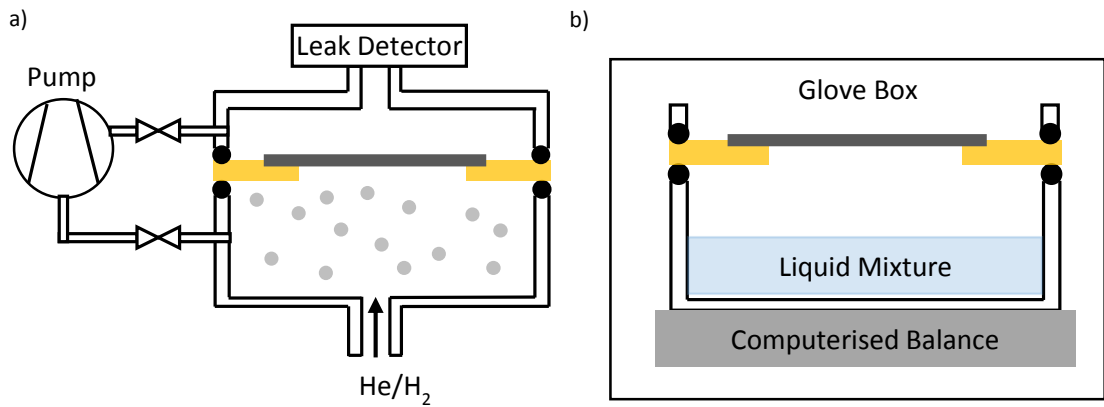
Figure 10 – Permeation experiments a) gas experiment setup b) water experiment setup[1]

observed when the container was filled with water. The rate of water loss through the G.O. membrane was the same as the weight loss without a membrane, under the same experimental conditions. A summary of the liquid and gas fluid rates of permeation is shown in Table 4.[1]

Table 4-Summary of fluid permeation experiments at room temperature [1]

Membrane	Fluid	Rate of permeation
<1 μm	Helium	$3.6*10^{-8}$ kg $h^{-1}m^{-2}bar^{-1}$
<1 μm	Hydrogen	$3.6*10^{-5}$ kg $h^{-1}m^{-2}bar^{-1}$
1 μm	Water	0.48 kg $h^{-1}m^{-2}$
Open apparatus	Water	0.54 kg $h^{-1}m^{-2}$
1 μm	Hexane	N/A
1 μm	EtOH	N/A

Further permeation studies at the University of Manchester investigated G.O. membranes supported on different polymeric and inorganic supports.[16] A G.O. layer was coated on a hydrophobic PTFE support, resulting in a very low separation performance. A submicrometer membrane exposed to a 60wt% water in IPA solution did not exhibit any preferential water permeation, Table 5. In fact, alcohol preferentially permeated through the membrane, with similar results being obtained for a 1 μm membrane. Preferential water permeation was obtained only with a 3 μm thick membrane. In all instances, rate of permeation was significantly lower than pure water permeation through a free standing membrane, 0.48 kg $h^{-1}m^{-2}$.[16]

Table 5-Water permeation through G.O. (PTFE support)

Membrane	Fluid	Total Flux	Permeate Water Purity
<1 μm	IPA/Water (Water 60wt%)	0.136 kg $h^{-1}m^{-2}$	31wt%
1 μm	IPA/Water (Water 60wt%)	0.05 kg $h^{-1}m^{-2}$	51wt%
3 μm	IPA/Water (Water 60wt%)	0.036 kg $h^{-1}m^{-2}$	73wt%

A G.O. layer showed a significantly better separation performance when it was coated on a hydrophilic support. Three different supports were investigated: alumina, PVDF and cyclopore polycarbonate. The patent does not explicitly state which of the three different

materials were used as a support for the tabulated pervaporation results, Table 6. The selectivity of the membranes was significantly better and water enrichment in the permeate was obtained with micrometre thick membranes.[16]

Table 6-Water permeation through G.O. (hydrophilic support) [16]

Membrane	Fluid	Total Flux	Permeate Water Purity
<1 µm	IPA/Water (Water 60wt%)	0.042 kg h^{-1}m^{-2}	52wt%
1 µm	IPA/Water (Water 60wt%)	0.038 kg h^{-1}m^{-2}	78wt%
5 µm	IPA/Water (Water 60wt%)	0.027 kg h^{-1}m^{-2}	66wt%

It is important to note that all experiments were conducted at room temperature in a vapour permeation mode. The membrane testing apparatus limited the ability to examine a wider scope of temperatures. Furthermore, no agitation was present at the surface of the membrane, which is known to negatively influence the rate of permeation and membrane selectivity.[11]

T. Yeh *et al.* investigated a multi-layered G.O. membrane performance in a pervaporation mode; liquid in contact with a membrane. Membranes were tested using permeation cell manufactured by Sulzer Chemtech.[71, 72]

The G.O. layer was coated on a thin film nanofibrous composite support. The support was composed of the following three parts:

1. Cellulose-an ultrafine nanofibrous top layer (in direct contact with G.O.)
2. Polyacrylonitrile-an electro spun nanofibrous middle layer
3. Polyethylene terephthalate-nonwoven microfibrous support

An ultrafine cellulose was able to hold a flaw-free G.O. layer over a wide range of thicknesses, 97-618 nm. As a model test solution, 20wt% water in EtOH at 70°C was selected for the study. The highest permeation flux of water, 2.2 kg $h^{-1}m^{-2}$, was obtained using 97nm G.O. layer. The permeate purity was slightly lower, 98.7wt%, when compared to the thicker, ≈ 620 nm, membrane which resulted in a 99.0wt% permeate purity. The higher permeate quality produced by a thicker membrane came at the expense of a significantly lower rate of permeation,0.9 kg $h^{-1}m^{-2}$, Table 7 Entry 1 and 2.[71]

Liu R et al. studied selective water permeation using a number of different aqueous alcohol mixtures.[73] The G.O. was coated on a PTFE polymeric support and the selective fluid separation was tested by placing the membrane into a three-piece filter. The bottom part of the filter was connected to a vacuum pump while the top part was loaded with the liquid of interest at room temperature.[73] In all instances, 5 μm thick membranes were used. It is important to note that the permeation fluxes were expressed as a function of water vapour pressure and a membrane thickness in the original publication.[73] The results shown in the Table 7 Entry 3 and 4 were converted to a form comparable with the results in the previous and the remainder of the document.

The permeation rate measured was considerably higher than that reported in the previous research at room temperature with higher water content and thinner or comparable thickness membranes Table 5 and Table 6. The selectivity of the membranes was also better than the membranes tested at the University of Manchester.[16] The separation magnitude and the permeation fluxes were closer to the

G.O. membranes tested in a pervaporation cell at higher temperatures Table 7 Entry 1 and 2.

Table 7-Organic compound dehydration using G.O. membrane.

Entry	Membrane	Fluid	Total Flux	Permeate Water Purity	Reference
1	0.093 µm	EtOH/Water (Water 20wt%)	2.2 kg $h^{-1}m^{-2}$	98.4wt%	[71]
2	0.62 µm	EtOH/Water (Water 20wt%)	0.9 kg $h^{-1}m^{-2}$	99wt%	[71]
3	5 µm	EtOH/Water (Water 25wt%)	1.23 kg $h^{-1}m^{-2}$	≈ 80wt%	[73]
4	5 µm	IPA/Water (Water 25wt%)	1.44 kg $h^{-1}m^{-2}$	≈ 90wt%	[73]

Tang. Y. P. *et al.* studied membrane fabrication pressure influence on separation performance. All membranes were assembled and tested in a dead end pressurised system.[74] The pervaporation rig was set up to provide rapid agitation above the membrane surface, which allowed minimisation of the concentration polarization, which may have been present in the previous pervaporation tests. All tests were performed at room temperature using mainly 2 µm thick G.O. selective layer. Aqueous ethanol solution was selected as a test fluid.[17]

It was found that membrane permeation flux and selectivity were sensitive to the membrane assembly pressure, Table 8. The highest permeate purity, 98wt%, water, was recorded for a membrane assembled under 5 bar pressure. However, the same membrane also exhibited the lowest permeation flux, 0.26 kg $h^{-1}m^{-2}$. Interestingly, a much higher permeation flux, 0.34 kg $h^{-1}m^{-2}$, was measured using a membrane assembled under 20 bar pressure. This came at the cost of a significantly reduced permeate quality, which dropped to 89.8wt%. It was postulated that the highest membrane coating pressure produced rapid G.O. deposition leading to multiple surface flaws, thus resulting in a lower permeate purity.[17]

Table 8-EtOH dehydration using G.O. membrane at a room temperature.[17]

Membrane	Fluid	Total Flux	Permeate Water Purity
2 µm (5 bar)	EtOH/Water (Water 15 wt%)	0.26 kg h^{-1}m^{-2}	98 wt%
2 µm (20 bar)	EtOH/Water (Water 15 wt%)	0.34 kg h^{-1}m^{-2}	89.8 wt%

Zhao. J. *et al.* have produced a composite gelatin (GE) and G.O. membrane on a hydrolysed polyacrylonitrile support. The polymeric support was dip coated in a GE and G.O. solutions multiple times Figure 11. The resulting membrane had a stable multilayer
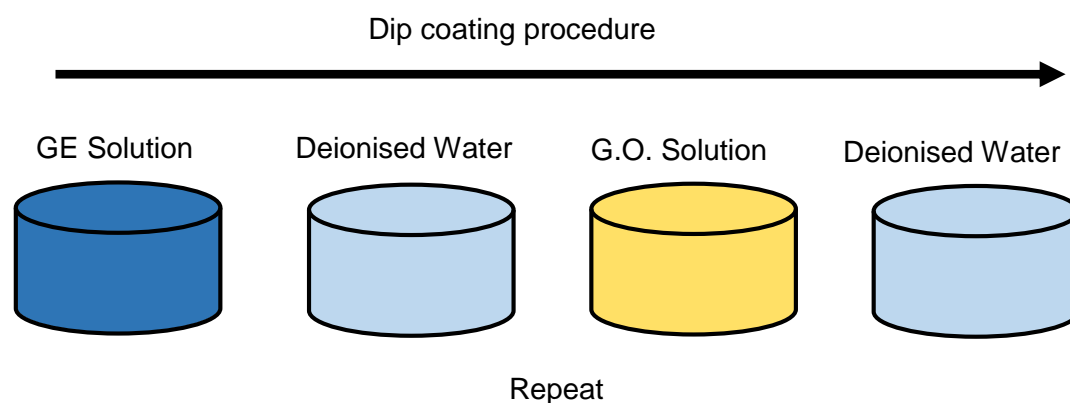
Figure 11 – Dip coating procedure.

G.O. and GE architecture.

The inner most and outer most layers were composed of GE. Pervaporation tests were conducted in a professional membrane testing rig CELFA P-28 manufactured by CM-Celfa AG Company in Switzerland.[15] The composite structure of membrane allowed the assembly of ultra-thin (115 nm) flaw-free membranes. Pervaporation flux and selectivity were evaluated using aqueous EtOH solution with membranes with different number of bilayers Table 9.[15] The highest rate of permeation, 3 kg h^{-1}m^{-2}, was observed using a membrane with only 2.5 bilayers. As anticipated, the membrane had the lowest water selectivity and enriched the process fluid from 10wt% water to 88wt% in the permeate. The lowest permeation flux, 1.8 kg h^{-1}m^{-2}, was recorded using a membrane with 10.5 bilayers (115 nm thick). However, a large number of bilayers rejected a lot of the EtOH in the stock solution and produced 97wt% water permeate.

Table 9-EtOH dehydration using G.O. membrane at 77°C.[15]

Membrane	Fluid	Total Flux	Permeate Water Purity
2.5 (bilayers)	EtOH/Water (Water 10 wt%)	3 kg h^{-1}m^{-2}	88 wt%
4.5 (bilayers)	EtOH/Water (Water 10 wt%)	2.4 kg h^{-1}m^{-2}	92 wt%
6.5 (bilayers)	EtOH/Water (Water 10 wt%)	2.2 kg h^{-1}m^{-2}	93 wt%
8.5 (bilayers)	EtOH/Water (Water 10 wt%)	2 kg h^{-1}m^{-2}	95 wt%
10.5 (bilayers)	EtOH/Water (Water 10 wt%)	1.8 kg h^{-1}m^{-2}	97 wt%

1.5.2 Ceramic Supported Graphene Oxide

Huang. K. *et al.* have coated a ceramic hollow fibre membrane with G.O. by vacuum suction. The ceramic tube coated with G.O. was tested by submerging it into a vessel filled with 97.4-99wt% dimethyl carbonate (DMC) and water solution at 25-40°C. Several selected results are shown in Table 10. An extraordinary fast water permeation, 1.1 kg h^{-1}m^{-2}, was observed at only 2wt% in DMC at 25°C. To the best of our knowledge, this is the best-recorded rate of permeation for a room temperature operation at 2wt%.

Table 10-DMC dehydration using G.O. membrane.[75]

Membrane	Fluid	Total Flux	Permeate Water Purity
1.5 µm (25°C)	DMC/Water (Water 2wt%)	1.1 kg h^{-1}m^{-2}	92wt%
1.5 µm (30°C)	DMC/Water (Water 2wt%)	1.25 kg h^{-1}m^{-2}	92wt%
1.5 µm (35°C)	DMC/Water (Water 2wt%)	1.3 kg h^{-1}m^{-2}	91wt%
1.5 µm (40°C)	DMC/Water (Water 2wt%)	1.4 kg h^{-1}m^{-2}	90wt%

1.6   Summary of Pervaporation Membranes

It is difficult to directly compare membrane performance data coming from a wide range of different research groups. For example, concentration polarisation is a hydrodynamic phenomenon affecting permeation flux which is equipment dependent.[11] Unfortunately, without experimental data, the effect of concentration polarisation cannot be factored out. In turn, it makes it difficult to comprehensively compare membrane performance data among researchers using different pervaporation equipment.[15, 16, 75] Furthermore, if the initial water concentration in the process solution is not the same across all experiments it has to be factored into the permeate purity calculation. This is typically done by calculating dimensionless membrane selectivity (Equation 6), which was described previously.

While comparing a range of different membranes and processes, pervaporation flux has to be normalised with respect to the membrane thickness and water vapour partial pressure, which is a function of temperature.

Previously published or known (from private communications) aqueous ethanol dehydration using commercial and G.O. membranes were compared and are shown in Figure 12. Three polymeric membranes commercialised by Sulzer Chemtech (PERVAP 1210, PERVAP 2210 and PERVAP 2510) occupy the centre of the figure. Membrane selectivity ranged from 14 to 72. Pervaporation was between 3.7 and 8.9 kg μm $h^{-1}m^{-2}bar^{-1}$.[34, 76] Recently, hybrid silica membranes sold by Pervatech (Dense HybSi) showed extremely high selectivity, 277.9. However, the normalised rate of permeation, 2.5 kg μm $h^{-1}m^{-2}bar^{-1}$, was slightly lower than that of the polymeric membranes. Dense HybSi, predecessor of HybSi membranes, demonstrated higher normalised flux, 3.5 kg μm $h^{-1}m^{-2}bar^{-1}$. Selectivity and normalised pervaporation flux were dominated by the state-of-the-art G.O. membranes, with selectivity ranging from 12 to 369 and normalised permeation rate 1-269 kg μm $h^{-1}m^{-2}bar^{-1}$. This broad range with huge potential in outperforming current commercial membranes has motivated us to pursue research in the field of hydrophilic G.O. membranes.
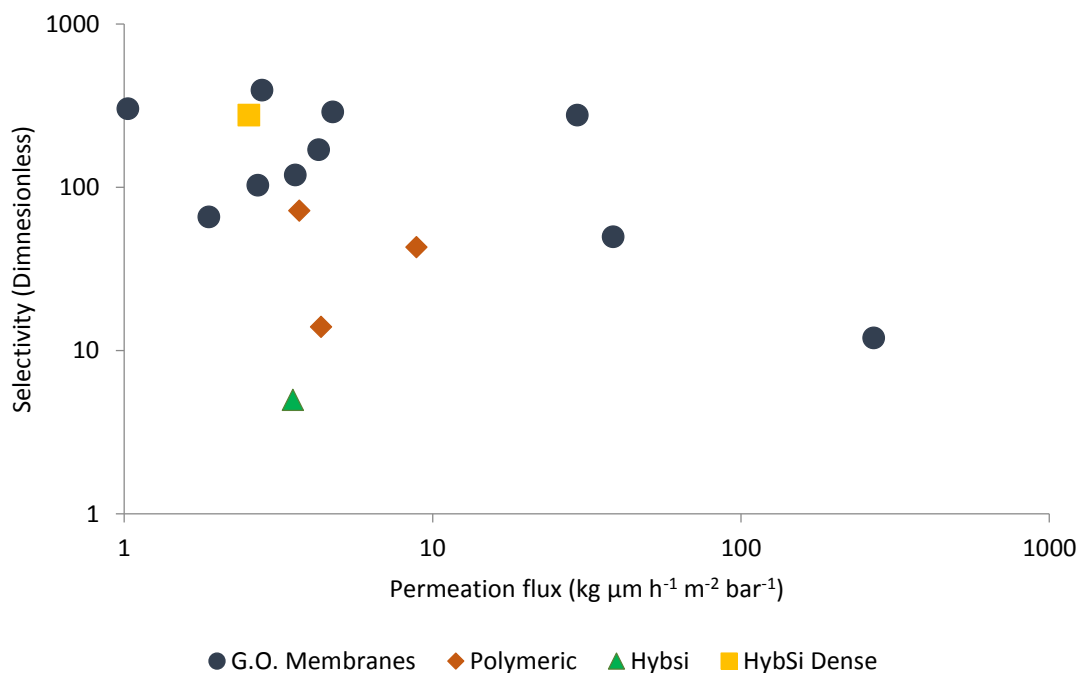
Figure 12-Aqueous ethanol mixture dehydration using different membranes

2 Pervaporation Modelling

To understand and predict pervaporation technology feasibility on a large scale it is essential to be able to model the process computationally. To do so, it is crucial to understand principles of water transport through dense membranes. This chapter will focus on the pervaporation mathematical modelling a process analysis. Predominantly, two different models have been applied for pervaporation modelling i) the pore-flow model, and ii) the solution-diffusion model. The pore-flow model is discussed briefly in this chapter by proving the main concept of the model and the governing equations. The solution-diffusion model is analysed in detail and is used in the further chapters for the pervaporation through G.O. membranes modelling. The model was also used to create a pervaporation simulation tool, which estimates the required membrane area for a desired water/organic compound separation problem.

2.1   Pore-flow model

One of the main models, pore-flow model, is based on the following assumptions: i) part of the pore is initially filled with liquid where liquid phase diffusion takes place, ii) liquid changes into vapour inside the pore, iii) the permeant is transported through the vapour filled portion of the pore to the permeate side.[77]

The main difference between the pore-flow model and the solution-diffusion model is the pressure gradient inside the membrane Figure 13 a). In the pore-flow model, the pressure drop (P) across the membrane produces a change in the chemical potential (μ), which results in the separation driving force. The solvent activity ($\gamma_i C_w$) remains unchanged throughout the membrane. In the solution–diffusion model, the pressure remains the same in the membrane and the concentration change produces a chemical potential gradient.

The pore-flow model assumes that there is a number of straight cylinder shaped pores of a length y penetrating the selective membrane layer from the process to the permeate side at isothermal conditions.[77] Figure 13 b) shows a schematic representation of the pore-flow model. The pore is partially filled with the permeating liquid without any separation. The distance of the penetration is denoted as a y_a. In the liquid filled section the permeant flows by liquid phase transport. The liquid section is followed by a vapour section with a length y_b. In this section, the permeant flows by vapour phase transport. The evaporation of the permeant takes place at the interface of a liquid-vapour boundary in the pore of the membrane. These assumptions allow pervaporation to be modelled as a combination of the liquid phase and vapour phase transport in series. [78]

a)

High pressure   Membrane   Low pressure

solution   vapour

Chemical potential, μ_i

Pressure, P

Solvent activity, $\gamma_i C_i$

b)

Membrane

y_m

y_a y_b

Process fluid (liquid)   Permeate (vapour)

$x_{w,}{}^*$ $y_{w,}{}^*$

P^*

P_1 P_2

$x_{w,1}$ $y_{w,2}$
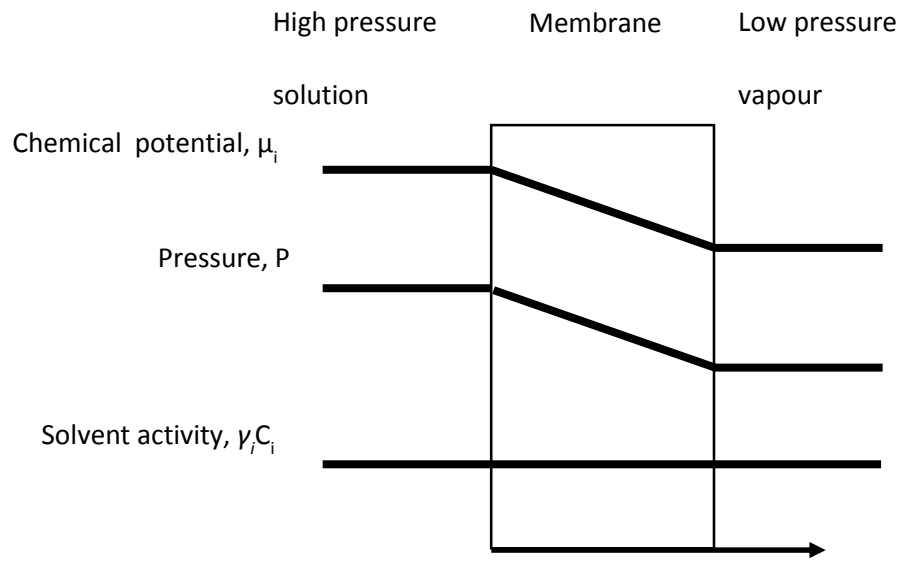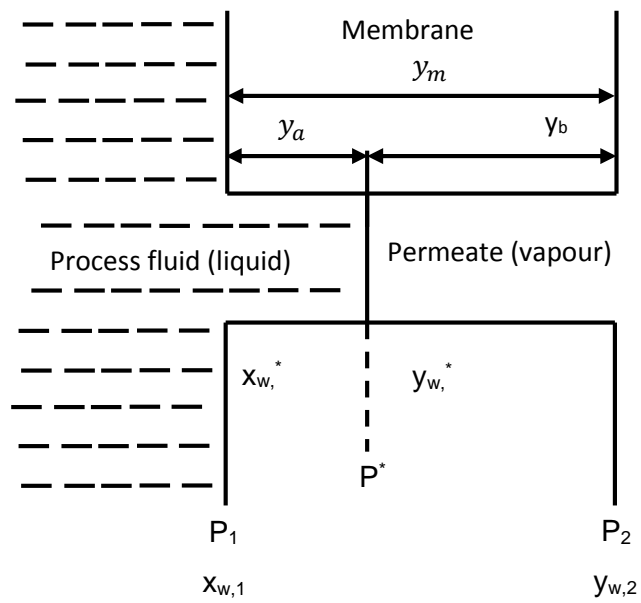
Figure 13-Pore-flow model a) depiction of the core concepts, b) schematic representation of the model.[2, 77]

The mass transport of a single component in the liquid phase is described by Darcy's Law shown in Equation 5 and Equation 6.

$$Q_{liquid} = \frac{X}{y_a}(P_1 - P^*)$$ Equation 5

$$X = \frac{\pi r^4 \rho N_t}{8\eta_L M_i}$$ Equation 6

Where, Q_{liquid} is molar liquid flux (mol m^{-2}s^{-1}), X is combined pore-flow model coefficient (mol bar^{-1}s^{-1} m^{-1}), r is the mean pore diameter (m),ρ is the fluid density (kg m^{-3}),N_t is the total number of pores per effective membrane area (m^{-2}),η_L is viscosity of the fluid (kg m^{-1} s^{-1}), and M_i the molecular weight of the component (kg mol^{-1}). The driving force in the liquid filled region is expressed as a pressure difference between the liquid, P_1 (bar), and saturated vapour pressure in the pore, P^* (bar).

For the vapour transport in the pore, several other assumptions are made. The pore is assumed to be so small that vapour adsorbed onto the surface of the pore occupies almost the entire space. This assumption means that all vapour transport is conducted *via* the surface flow mechanism, a gas flow model originally defined and applied by Gilliland.[77, 79]

This assumption of the vapour flow sets an upper pore size limit, 1^{-10}-1^{-9} m, where this model is valid. If the pore is large enough to accommodate Knudsen flow the model becomes inapplicable. Also, the validity of Henry's law is assumed. Based on the assumptions of the vapour phase transport the molar flux can be calculated using Equation 7 and Equation 8.

$$Q_{Vapour} = Q_{Surface} = \frac{Z}{y_b}((P^*)^2 - (P_2)^2)$$ Equation 7

$$Z = \frac{\pi(2rt_a - t_a^2)^2 t_a N_t}{8r}\frac{RT}{\eta_G}(k_H')^2$$ Equation 8

Where, Q_{Vapour} is vapour molar flux (mol m^{-2}s^{-1}),t_a Is the thickness of the adsorbed monolayer of the gas (m),R is the ideal gas constant (m^3 bar K^{-1}mol^{-1}),T is temperature (K),η_G is viscosity (kg m^{-1} s^{-1}), and k_H' is the product of the weight of the membrane/volume of adsorbed gas molecules and Henry's constant (mol m^{-3}bar^{-1}). The vapour phase driving force is a square pressure difference between saturated vapour pressure and the permeate pressure respectively.

The combination of the liquid flow, Equation 5, and vapour flow, Equation 7, leads to the total molar flux expression Equation 9

$$Q_{total} = \frac{X}{y}(P_1 - P^*) + \frac{Z}{y}((P^*)^2 - (P_2)^2) \qquad \text{Equation 9}$$

There are several variations of the Equation 9 that are important to note. Equation 9 is valid only when $P_2 < P^*$. If the pressure of the permeate side is greater than the saturated liquid vapour pressure, $P_2 \geq P^*$ the entire pore fills up with a liquid permeate. In this instance the permeation equation can be reduced to the liquid phase transport resistance (Equation 10).

$$Q_{total} = \frac{X}{y_a}(P_1 - P_2) \qquad \text{Equation 10}$$

For a binary mixture the equation has to be changed to include individual rates of permeation. A binary pair liquid phase, for instance water and organic component, transport rate remains the same (Equation 11).

$$Q_{liquid} = \frac{Z_{mixture}}{y_a}(P_1 - P^*) \qquad \text{Equation 11}$$

However the rate of vapour transport model has to be changed to reflect different rates of permeation of each component, Equation 12 and Equation 13.

$$Q_{w,Vapour} = \frac{Z_w}{y_b}((P_w^*)^2 - (P_{w,2})^2) \qquad \text{Equation 12}$$

$$Q_{org,Vapour} = \frac{Z_{org}}{y_b}((P_{Org}^*)^2 - (P_{Org,2})^2) \qquad \text{Equation 13}$$

A total molar permeate flux is then expressed by a combination of the Equation 11, Equation 12 and Equation 13, which yields Equation 14.

$$Q_{Total} = \frac{X_{mixture}}{y_a}(P_1 - P^*) + \frac{Z_w}{y_b}((P_W^*)^2 - (P_{W,2})^2) + \frac{Z_{org}}{y_b}((P_{Org}^*)^2 \qquad \text{Equation 14}$$
$$- (P_{Org,2})^2)$$

According to the pore-flow model, the membrane separation power stems from the different rates of adsorbed layer permeation. The permeate purity, vapour mole fraction, can be calculated by estimating the rate of permeation ratio (Equation 15). The expression requires partial vapour pressure of both components, which are usually known for a typical binary system. To calculate individual component enrichment in the

permeate individual permeation constant does not have to be known. A ratio of the vapour permeability coefficients B_{org} and B_W, can be assumed.

$$\frac{Q_{W,Vapour}}{Q_{W,Vapour} + Q_{Org,Vapour}}$$

<div align="right">Equation 15</div>

$$= \frac{(P_W^*)^2 - \left(P_{W,2}\right)^2}{((P_W^*)^2 - \left(P_{W,2}\right)^2) + \frac{Z_{Org}}{Z_W}\left((P_{Org}^*)^2 - \left(P_{Org,2}\right)^2\right)}$$

$$= y_{W,2}$$

The effects of different vapour permeability coefficient ratios of the Water/IPA pair are shown in Figure 14. The partial water and IPA pressures were calculated at 50°C using Aspen plus. The mixture vapour-liquid equilibrium line is shown as a guideline for separation effectiveness.

As the ratio of the $\frac{Z_{Org}}{Z_W}$ decreases the water mole fraction in the vapour phase increases, leading to strongly enriched water in the vapour phase. The permeate water mole fraction is exceptionally sensitive to the water mole fraction in the liquid phase when a permeability constant less than 0.01. For the intermediate ratios of the $\frac{Z_{Org}}{Z_W}$ (0.01 − 0.1) the enrichment of water in the vapour phase drops significantly. When the permeability constant ratio drops below 1 IPA becomes enriched in the vapour phase permeate.
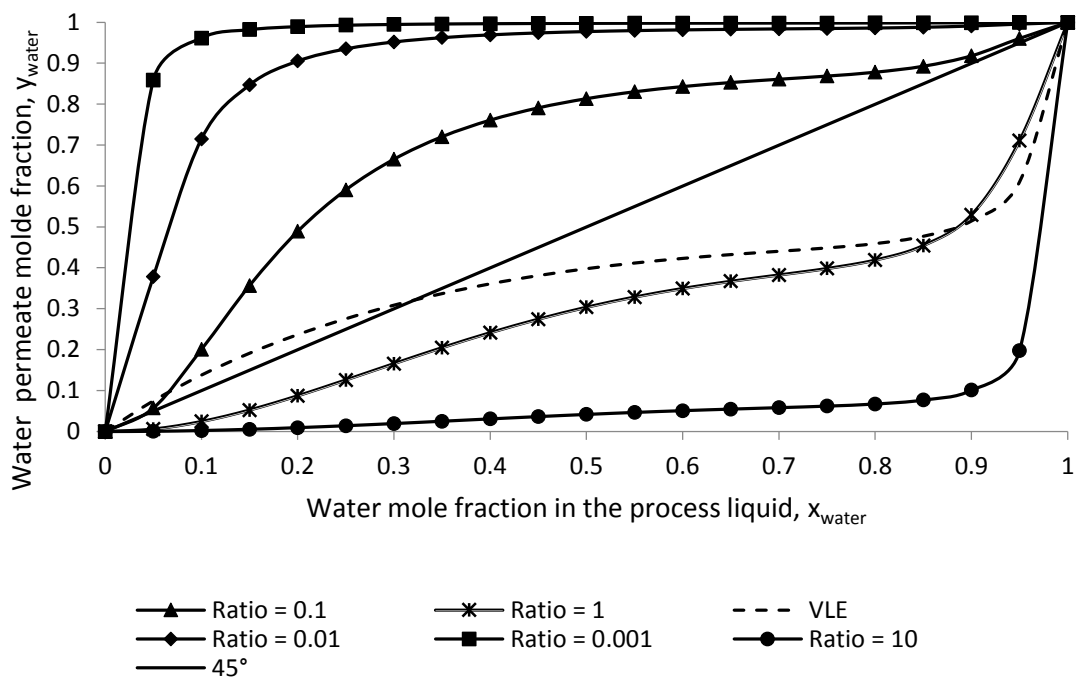
Figure 14 – Pore-flow model predictions of permeate water mole fraction[77]

The pore-flow model is valid for membranes with small pores in the range of $1^{-10} - 1.5^{-9}$ m.[77] G.O. falls in this range by having an approximate pore size of 3.49^{-10} m and an intersheet spacing of 6.89^{-10} m, thus pore-flow model should be applicable.[80] For a more detailed pore-flow model derivation the reader is referred to the original publication.[81]

2.2 Solution-diffusion model

Currently, solution-diffusion is the main model used to explain the pervaporation process.[18] The model is based on the assumption that the permeating species dissolves in the membrane material and then diffuses through the thickness of the membrane.[2] The rate of permeation is based on the concentration gradient, which is mathematically related to the chemical potential. The selectivity of a membrane is the result of different partitioning coefficients of the compounds into the membrane matrix. A simplified image of the main concepts behind the solution-diffusion model are shown in Figure 15. The solution-diffusion model assumes that a pressure applied across a dense membrane is distributed everywhere evenly and is constant across the thickness of the membrane. In this model, the driving force is expressed as a concentration gradient within the membrane, which is linked to the chemical potential and in turn can be mathematically expressed as a partial pressure of the permeating component. [2]
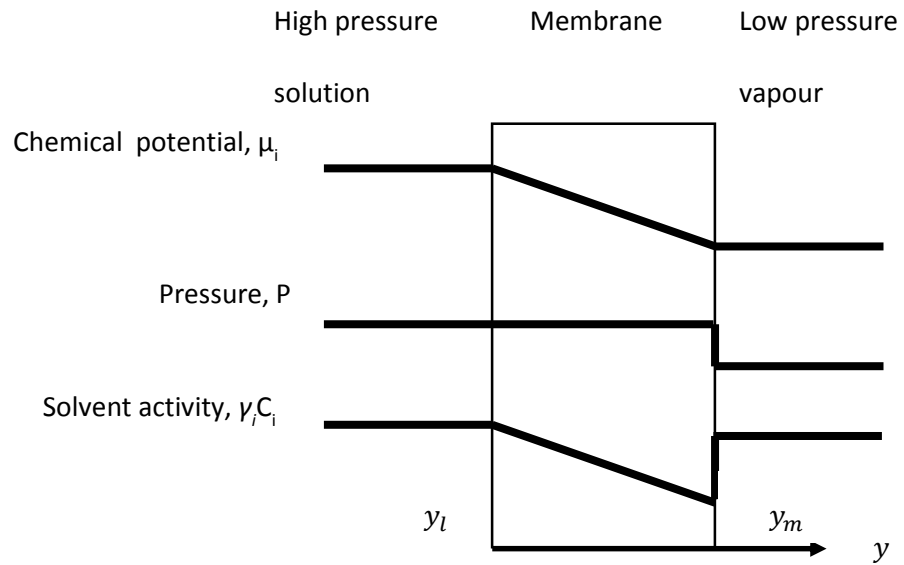
Figure 15 – Schematics of the solution diffusion concepts[2]

The mass flux through a dense membrane is expressed by Fick's law, Equation 16:

$$J = -D_w \frac{d\rho_w}{dy_m}$$

Equation 16

Where, J is the mass flux of the permeating species (kg $m^{-2}s^{-1}$), D_w is the diffusion coefficient (m^2s^{-1}), and δ_m is the thickness of the membrane (m).

$$\rho_w = C_w M_w x_w$$

Equation 17

The ρ_w is mass concentration (kg m^{-3}), C_w is molar concentration (mol m^{-3}), M_w is the molecular weight (g mol^{-1}), and x_w is the mole fraction (mol mol^{-1}).

Upon integration over the thickness of the membrane Equation 16 leads to Equation 18.

$$J = \frac{D_w(\rho_{w,ML} - \rho_{w,MS})}{y_m}$$

Equation 18

The Equation 18 is a fundamental expression relating mass concentration on the process side next to the membrane surface ($\rho_{w,ML}$) and the permeate leaving the membrane and entering the support layer ($\rho_{w,MS}$) to the pervaporation flux (J) with respect to the membrane thickness (y_m).

The general expression, Equation 18, is derived from the chemical potential differential Equation 19. The expression links the change of the chemical potential to the mole fraction and pressure changes.

$$d\mu_W = RTdln(\gamma_W x_W) + V_{mol}dP \qquad \text{Equation 19}$$

It is assumed that at the liquid/membrane interface the chemical potential of the liquid is the same as the chemical potential in the membrane ($\mu_{LM} = \mu_{ML}$).

The full expression:

$$\mu°_{W,LM} + RTln(\gamma_{w,LM}\, x_{w,LM}) + V_{mol}(P_{w.L} - P^*) \qquad \text{Equation 20}$$
$$= \mu°_{W,ML} + RTln(\gamma_{W,ML} x_{w,ML}) + V_{mol}(P_{w.L} - P^*)$$

Where $\mu°_w$ is the chemical potential of the pure component at the reference point P^*. When rearranged Equation 20 leads to an expression for the concentration on the process side Equation 21:

$$\rho_{w,ML} = \frac{\gamma_{LM} C_{ML}}{\gamma_{ML} C_{LM}} \rho_{w,LM} = K_S^L \rho_{w,LM} \qquad \text{Equation 21}$$

Where K_S^L is the liquid side sorption or partition coefficient.[2]

At the membrane/gas interface, the pressure drops from the pressure in the membrane to the pressure in the gas, thus the molar volume changes. Equation 19 is modified using an ideal gas equation to correct for the molar volume change and integrated to give Equation 22.

$$\mu°_{W.SM} + RTln(\gamma_{SM} x_{w,SM}) + RT\ln(\frac{P_{w.L}}{P^*}) \qquad \text{Equation 22}$$

Again, it is assumed that the chemical potential at the membrane/gas interface is at the equilibrium Equation 23.

$$\mu°_{W,MS} + RTln(\gamma_{MS} x_{w,MS)}) + V_{mol}(P_{w.L} - P^*) \qquad \text{Equation 23}$$
$$= \mu°_{W,SM} + RTln(\gamma_{SM} x_{w,SM}) + RT\ln(\frac{P_{w.L}}{P^*})$$

Rearranging Equation 23 gives Equation 24.

$$x_{w,MS} = \frac{\gamma_{SM} x_{w,SM}}{\gamma_{MS}} \frac{P_{w.L}}{P^*} e^{\frac{-V_{mol}(P_{w.L} - P^*)}{RT}} \qquad \text{Equation 24}$$

The exponential term is known to be close to 1, thus it can be ignored.[2] This simplifies Equation 24 to Equation 25

$$x_{w,MS} = \frac{\gamma_{SM} x_{w,SM}}{\gamma_{MS}} \frac{P_{w.L}}{P^*}$$

<div align="right">Equation 25</div>

The product of the $x_w \gamma_{SM} P_{w.L}$ can be replaced by a partial pressure term on the permeate side P_p and simplified to Equation 26

$$\rho_{w,MS} = M_w C_{w,MS} \frac{\gamma_{SM}}{\gamma_{MS} P^*} P_{w.p} = K_S^G P_{w.p}$$

<div align="right">Equation 26</div>

Where $K_S^G = M_w C_{wMS} \gamma_{SM} \gamma_{MS}^{-1} P^{*-1}$ is the gas phase sorption coefficient.

The concentration change across the membrane is now fully defined. The driving force gradient in Fick's law, Equation 18, can now be replaced to derive the membrane flux Equation 27.

$$J = \frac{D_w(K_S^L \rho_{w,LM} - K_S^G P_{w.p})}{y_m}$$

<div align="right">Equation 27</div>

However, Equation 21 contains the liquid sorption coefficient while Equation 26 has gas sorption coefficient. The interconversion of these coefficients is handled by considering a hypothetical vapour-liquid equilibrium Equation 28. [82]

$$\mu_W^\circ + RTln(\gamma^L x_w^L) + V_{mol}(P_{w.L} - P^*)$$
$$= \mu_W^\circ + RTln(\gamma^G x_w^G) + RT \ln(\frac{P_{w.L}}{P^*})$$

<div align="right">Equation 28</div>

Using the same rearrangement as in Equation 23, Equation 24, Equation 25 and Equation 26 the vapour liquid equilibrium become Equation 29.

$$\rho_w^L = M_w C_w \frac{\gamma^G}{\gamma^L P^*} P_{w.L} = \frac{K_S^G}{K_S^L} P_{w.L}$$

<div align="right">Equation 29</div>

Where $P_{W.L}$ is the partial vapour pressure of water in equilibrium with the feed liquid. It is worth noting that the term $M_w C_w \gamma^G \gamma^{-1(L)} P^{-1(*)}$ is also known as Henry's law coefficient, H.

Combining, Fick's law, Equation 27 and Equation 29, results in a pressure normalised pervaporation flux Equation 30.

$$J = \frac{D_w K_S^G (P_{w.L} - P_P)}{y_m} = k_{M.P}(P_{w.L} - P_{w.P})$$

Where $k_{M.P}$ (g m^{-2}bar^{-1}s^{-1}) is a pressure normalised pervaporation coefficient. By selecting a partial vapour pressure as a driving force, the normalized permeability coefficient becomes $k_{M.P} = k_{L.P.GO}/y_m$, where $k_{L.P.GO}$ is the permeability constant (g m bar^{-1}m^{-2}s^{-1}) and δ_m is membrane thickness (m). The change in the feed composition and the temperature is reflected by the change in partial vapour pressure.[71, 83]

The process liquid was considered as non-ideal solution. The vapour pressure was calculated using Equation 31. The water activity coefficient was calculated using Aspen Plus software.

$$P_{w.L} = P_w^* x_w \, \gamma_w$$

The saturated vapour pressure of pure component was calculated using the Antoine Equation 32

$$\log_{10} P^* = A_{antoine} - \frac{B_{antoine}}{C_{antoine} + T}$$

Where *A*, *B* and *C* are material constants (Table 11) and T (K) is temperature.

Table 11-Antoine constants for water in the temperature range 273-303 K [84]

Parameter	Value
$A_{antoine}$ (bar)	5.40
$B_{antoine}$ (bar K^{-1})	1838.68
$C_{antoine}$ (K)	-31.74

2.3 Concentration polarisation

The main membrane performance criteria are permeation flux and selectivity. A rate of the permeating species through a membrane is affected by a number of different parameters and is assumed to be a function of the following steps: i) mass transport through the liquid boundary layer, ii) preferential sorption of the permeating species into a membrane matrix, iii) diffusion through the membrane layer, iv) desorption from the membrane, v) vapour transport through the porous support layer, and vi) mass transport through a vapour boundary layer. A detailed concentration distribution in a pervaporation operation is shown in Figure 16
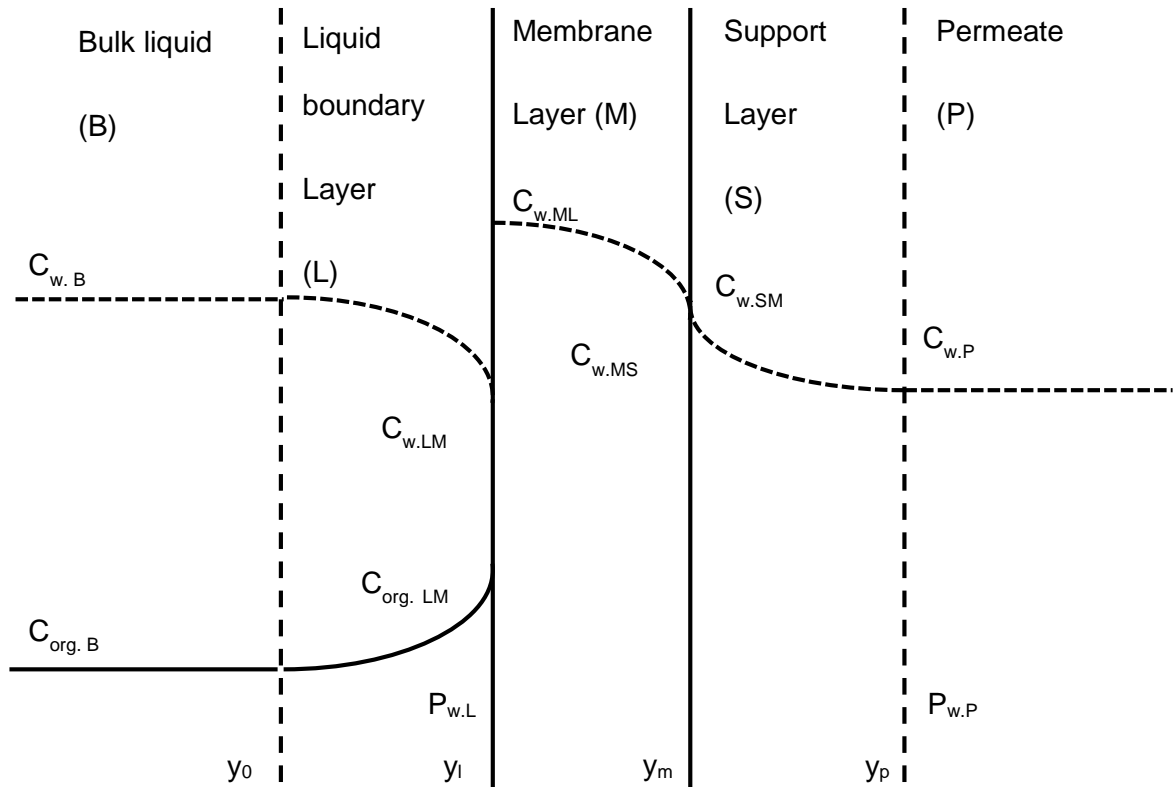
Figure 16 – Detailed resistance in series model

The key to modelling membrane separation behaviour is in the understanding of the hydrodynamics and physicochemical properties effect on the overall mass transfer coefficient k_{ov} [85] In this study boundary layer is assume to be fully developed and is time independent.

In the pervaporation separation process one liquid component is in contact with the membrane and is being enriched in the permeate stream. The depletion of a single component at the membrane surface creates an increase in the concentration of the species that does not permeate through the membrane and a reduction in the concentration of the species that does pass through the membrane compared to the bulk liquid on the process side. This creates a concentration difference between the membrane surface and the bulk fluid. In the membrane research literature thus the phenomena on the concentration distribution is regarded as concentration polarization.[11] The concentration polarization leads to a decrease in the driving force across the membrane of the more permeating species and increase in the driving force of the less permeating compound. This leads to a decrease in the separation power of the membrane. In pervaporation of a liquid containing small particulates and large molecules concentration polarization may inflict fouling, precipitation or gelation of the

rejected compound on the membrane surface. This in turn, results in a slower permeation flux and a decrease in the membrane selectivity.[86, 87]

The concentration polarization process can be analysed mathematically. In the liquid boundary layer the water flux, $J_v C_{w,P}$, is equal to the convective flux, $J_v C_w$, and diffusive flux, $-D_w(dC_w/d\delta_l)$. This leads to a mass balance expression, Equation 33.[88]

$$J_v C_w - D_W \frac{dC_w}{dy_l} = J_v C_{w,P}$$

Equation 33

Equation 33 can be integrated across the liquid boundary layer to give Equation 34 known as concentration polarization equation.

$$\frac{C_{w,LM} - C_{w,P}}{C_{w,B} - C_{w,P}} = \exp(J_v y_l / D_W)$$

Equation 34

Where $C_{w,LM}$ is the concentration of water at the membrane surface, $C_{w,P}$ is the concentration of water in the permeate and $C_{w,B}$ is water concentration in the bulk solution; J_v is volumetric permeation flux (m^3 $m^{-2}s^{-1}$), y_l is liquid boundary layer film thickness (m) and D_W is the diffusion coefficient (m^2 s^{-1}). An alternative form of the concentration polarization equation replaces concentration terms with enrichment factors E defined as $C_{w.P}/C_{w.B}$ and E_0, an enrichment present without liquid boundary layer, defined as $C_{w.P}/C_{w.LM}$, also called an intrinsic enrichment factor.[88] The concentration polarization expression is then rewritten as Equation 35.

$$\frac{\frac{1}{E_0} - 1}{\frac{1}{E} - 1} = \exp(J_v y_l / D_W)$$

Equation 35

In the pervaporation process, the enrichment factor is larger than unity. This implies that minor component in the solution is being depleted at the membrane surface and is selectively permeating to another side. The ratio of the concentration of the permeating species at the membrane surface and the bulk solution $C_{w.LM}/C_{w.B}$ is called polarization modulus. When concentration polarization modulus is 1 there is no concentration polarization present. If the modulus deviates from unity, its effect on the pervaporation flux and selectivity becomes important. Rearrangement of the Equation 34 and Equation 35 leads to Equation 36.

$$\frac{C_{w.LM}}{C_{w.B}} = \frac{e^{\left(\frac{J_v y_l}{D_W}\right)}}{1 + E_0(e^{\left(\frac{J_v y_l}{D_W}\right)} - 1)}$$

<div align="right">Equation 36</div>

$$Pe = \frac{J_v y_l}{D_w}$$

<div align="right">Equation 37</div>

Equation 36 shows factors involved in the concentration polarization: i) boundary layer thickness (y_l), volumetric pervaporation flux (J_v), and diffusion coefficient D_w. A change in any of these variables will affect the concentration polarization. The expression can be simplified by introducing Peclet number in the exponential term, Equation 37.

The easiest way to control the concentration polarization is to change the liquid boundary layer thickness. As the liquid boundary layer thickness, y_l, decreases the polarisation modulus decreases exponentially, Equation 36. The liquid boundary can be decreased by increasing turbulent mixing at the membrane surface. In the membrane module design the increase in the turbulence is achieved *via* an increase in the fluid velocity. Other techniques involve placing a membrane spacer to promote mixing or pulsing the feed solution. [89, 90]

The concentration polarization is also linked to the membrane selectivity. If the membrane is completely unselective, $E_0 = 1$, the concentration at the membrane surface and the components passing through the membrane does not change. In turn, concentration polarization layer is not generated.

The balance between the convective and diffusive transport in the liquid boundary is characterised by $J_v y_l/D_w$. This term is a ratio of the convective transport, J_v, and diffusive transport, y_l/D_w, and is commonly referred as the Peclet (Pe) number in the research literature.[83] By varying the Peclet number and an enrichment factor for a hypothetical membrane separation process a degree of concentration polarization can be calculated. The extent of the concentration polarization for a given Pe number and an intrinsic enrichment factor is shown in Figure 17. As expected, in a process where liquid boundary layer is thicker or diffusion is lower the concentration polarization is larger. In addition, an increase in the total permeate flux depletes more permeating species at the membrane surface faster, thus it can also contribute towards the increase of the concentration polarization. At high Pe numbers >10 the concentration polarization reaches its maximum ($1/E_0$) value.
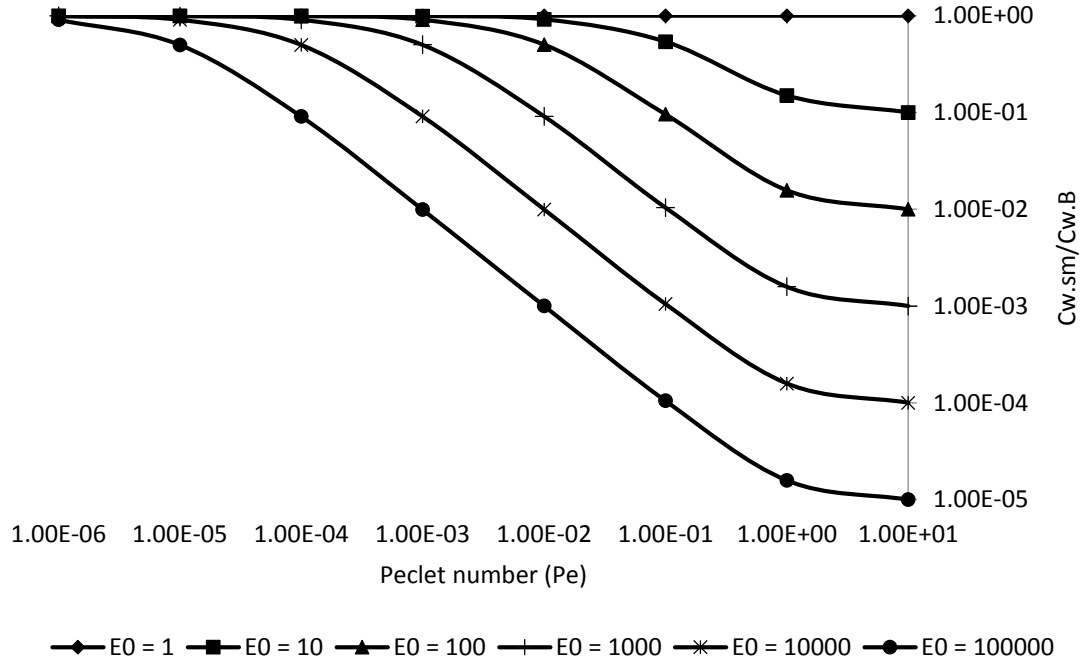
Figure 17 - Concentration polarization [83]

2.3.1 Liquid and membrane layer concentration polarization

A general solution of the mass transfer through a liquid boundary layer and a membrane can be expressed by two second order differential mass balance equations Equation 38, Equation 39.

$$v \frac{dC_w}{dy_l} - D_w \frac{d^2 C_w}{dy_l^2} = 0 \qquad 0 \leq y \leq y_l \qquad \text{Equation 38}$$

$$D_{w.m} \frac{d^2 C_{w.M}}{dy_m^2} = 0 \qquad y_l \leq y \leq y_l + y_M \qquad \text{Equation 39}$$

Where v is convective velocity (m s^{-1}). After integration of Equation 38, Equation 39 the concentration distribution in the liquid and membrane boundary layers respectively is then given by Equation 41 and Equation 45.

To solve 2nd order linear homogenous differential Equation 38 it was assumed that the solution was proportional to exponential function, Equation 40.

$$C_w = e^{\lambda y} \qquad \text{Equation 40}$$

Using the exponential function assumption differential mass transport equations were solved as follows:

$$v \frac{d}{dy_l}(e^{\lambda y}) - D_w \frac{d^2}{dy_l^2}(e^{\lambda y}) = 0$$

72

The differential terms are then evaluated:

$$\frac{d}{dy_l}\left(e^{\lambda y}\right) = \lambda e^{\lambda y} \text{ and } \frac{d^2}{dy_l^2}\left(e^{\lambda y}\right) = \lambda^2 e^{\lambda y}$$

The unknown function parameter, λ, is then expressed found.

$$v\lambda e^{\lambda y} - D_w \lambda^2 e^{\lambda y} = 0$$

$$e^{\lambda y}\left(v\lambda - D_w \lambda^2\right) = 0$$

$$\lambda = 0 \text{ or } \lambda = \frac{v}{D_w}$$

Once the unknown parameter, λ, is expressed full concentration expression can be written, .

$$C_{w.B} = Y_1\ e^{\frac{vy}{D_w}} + Y_2 \qquad 0 \le y \le y_l \tag{Equation 41}$$

Equation 42 describes mass transport in the membrane layer.

$$D_{w.m}\frac{d^2 C_{w.M}}{dy_m^2} = 0 \qquad y_l \le y \le y_l + y_M \tag{Equation 42}$$

If the concentration is assumed to be proportional to an exponential function, Equation 43.

$$C_{w.M} = e^{\lambda y} \tag{Equation 43}$$

The mass transport equation has only single answer to the variable

$$D_{w.m}\lambda^2 e^{\lambda y} = 0$$

$$\lambda^2 = 0$$

The general solution to a differential equation with a repeated root is, Equation 44.

$$C_{w.M} = Y_{M1}y e^{\lambda y} + Y_{M2}e^{\lambda y} \tag{Equation 44}$$

The final form of the developed Equation 42 is then Equation 45.

$$C_{w.M} = Y_{M1}y + Y_{M2} \qquad y_l \le y \le y_l + y_M \tag{Equation 45}$$

Where Y_1 and Y_2 are general solution constants of the liquid boundary layer and Y_{M1} and Y_{M2} are general solution constants of the membrane layer. To solve the equations, boundary conditions have to be applied, which lead to Equation 46, Equation 47, Equation 48 and Equation 49.[91]

$$Y_1 + Y_2 = C_{aq.B} \text{ at } y = 0 \tag{Equation 46}$$

$$v * Y_2 = -D_M * Y_{M1} \text{ at } y = y_l \tag{Equation 47}$$

$$K_S^L(Y_1 \exp Pe + Y_2) = Y_{M1} * \delta_M + Y_{M2} \text{ at } y = y_l \qquad \text{Equation 48}$$

$$Y_{M1}(y + y_M) + Y_{M2} = C_{MS} \text{ at } y = y + y \qquad \text{Equation 49}$$

These equations can be rearranged to give a water flux through the liquid and membrane layers with respect to a Pe number Equation 50.[11]

$$Q = k'_{LM} * \left(C_{w.B} e^{Pe} - \frac{C_{w.MS}}{K_S^L} \right) \qquad \text{Equation 50}$$

Where

$$\frac{1}{k'_{LM}} = \frac{1}{\frac{k'_L * Pe}{e^{Pe} - 1}} + \frac{1}{k'_M K_S^L} \qquad \text{Equation 51}$$

Equation 51 relates overall (liquid boundary layer and the membrane) mass transfer coefficient to Pe number and the selective component sorption into the membrane matrix.[91] The significance of this expression is the relationship between the Pe number and the combined mass transfer coefficient, k_{LM}.

The concentration polarization, $C_{w,LM}/C_{w,B}$, for a pervaporation process modelled using liquid and membrane transport phenomena is shown in Equation 52.

$$\frac{C_{w.LM}}{C_{w.B}} = \frac{Ne^{Pe} + (e^{Pe} - 1)C_{w,P}/(C_{w,B}K_S^L)}{e^{Pe} - 1 + N} \qquad \text{Equation 52}$$

Where,

$$N = \frac{k'_l Pe}{k'_m K_S^L} = \frac{J_v}{k'_m K_S^L} \qquad \text{Equation 53}$$

The difference between concentration polarization expression Equation 36 and Equation 52 is the intrinsic enrichment factor. In the Equation 36 the intrinsic enrichment factor has to be assumed, while Equation 52 does not require the intrinsic enrichment factor, which generally is not known. [91] The permeate concentration on the vacuum side is often also not known. However, relatively low pressure, < 5mbar, is usually applied, which makes permeate water concentration tend to decrease close to zero value.

The concentration polarization with respect to changing Pe number and assumed N value is shown in Figure 18. The polarization decreases with the decrease in the Pe number. A decrease in the N value leads to an increase in polarization, which means that an increase in the membrane permeability or an increase in the Henry coefficient (permeating component solubility in the membrane matrix) creates a more polarized boundary layer.
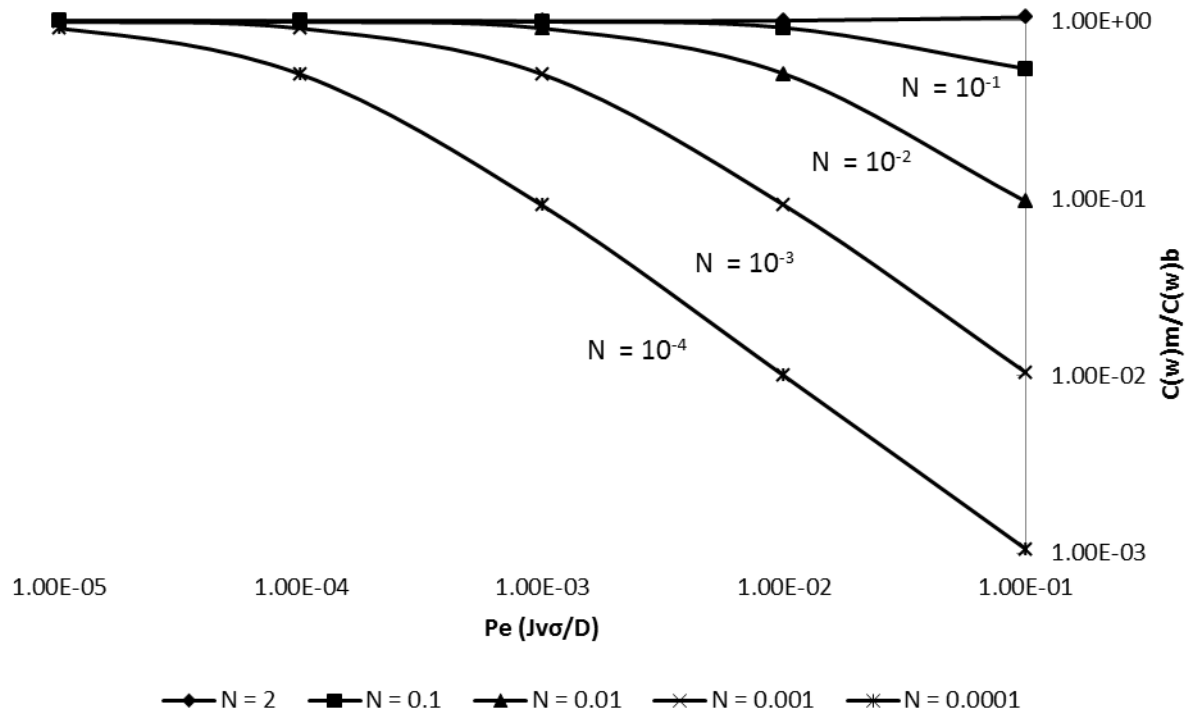
Figure 18-Concentration Polarization with respect to N value[91]

Typically, Pe is in a range of 10^{-3}-10^{-4} [83], which leads to expression Equation 54.

$$\frac{1}{k'_{LM}} \approx \frac{1}{k'_L} + \frac{1}{k'_M} \qquad \text{Equation 54}$$

2.3.2   Desorption of water at the membrane/support interface and diffusion through the porous support

Once water passes the semi-permeable membrane the pressure drops to a vacuum level ≈ 5mbar. The permeate molecules evaporate from the membrane/support interface and proceed to diffuse through a support layer. In the research literature, this step is considered as fast and does not produce a significant amount of mass transfer resistance. [92]

In small capillaries gasses can travel one of three ways which is determined by the Knudsen number Equation 55.[93]

$$N_{kn} = \frac{y_p}{r} \qquad \text{Equation 55}$$

Three different mass transport mechanistic models are summarised in the

Table 12

Table 12-Vapour transport in porous media

Knudsen number	Mechanism of flux
$N_{kn} > 10$	Knudsen flow
$0.01 < N_{kn} < 10$	Transient flow
$N_{kn} \leq 0.01$	Viscous flow

In this study the support layer has ≈ 0.2µm nominal pore size and is 125µm thick. It is hard to estimate the tortuosity of the channels to predict a mean free path. However, it is anticipated that N_{kn} will be much greater than 10. Therefore, the water vapour transport mechanism should follow the Knudsen flow model Equation 56.

$$J = \frac{2}{3} * \frac{d_p * \varepsilon}{y_p * \chi} * \left(\frac{8 * R * T}{\pi * M}\right)^{\frac{1}{2}} * \frac{M}{R * T} * (P_{w.SM} - P_{w.P})$$

Equation 56

2.3.3 Transport through the vapour boundary layer

The vacuum side is typically set at ≈ 5mbar this leads to an assumption that as soon as vapour leaves the membrane support it is taken away and thus presents no mass transport resistance. Typically, this assumption is made by researchers when studying pervaporation using high vacuum.[92, 94] However, this is not the case when nitrogen swept gas is applied to remove the permeate vapour.[94]

2.3.4 Combined mass transfer model

Overall pervaporation mass transfer resistance can be considered as a sum of all resistances in series. By combining Equation 57, Equation 58 and Equation 59 an overall mass transfer coefficient is derived Equation 60.

$$R_{Liquid} = \frac{1}{\frac{k'_L * Pe}{e^{Pe} - 1}}$$

Equation 57

$$R_{Membrane} = k`_M$$

Equation 58

$$R_{Support} = \frac{1}{\frac{2}{3} * \frac{d_p * \varepsilon}{\delta_s * \chi} * \left(\frac{8 * R * T}{\pi * M}\right)^{\frac{1}{2}} * \frac{M}{R * T}}$$

Equation 59

$$\frac{1}{R_{total}} = \frac{1}{R_{Liquid} + R_{Membrane} + R_{Support}}$$

Equation 60

Using resistance in series model pervaporation flux is then expressed as a product of the total resistance and the difference of the permeating species concentration.

$$J = \frac{1}{R_{Liquid} + R_{Membrane} + R_{Support}} * K_S^G * (P_{w.B} - P_{w.P})$$

Equation 61 is a rigorous membrane model mainly because it encapsulates every parameter involved in the pervaporation phenomena. Furthermore, each resistance can be changed individually if any of the membrane parameters change. For in depth variable examination reader is referred to the original publication.[92]

3 Methods and Materials

3.1 Membrane Coating

A circular hydrophilic polyvinylidene fluoride (PVDF) membrane (GVWP04700 Durapore, purchased from Millipore) was placed in the middle of a three piece Whatman filter funnel (70mm diameter, 210mL reservoir volume). The funnel was filled with 20 ± 1mL of DI water to pre-wet the PVDF membrane followed by initiation of a water aspirator. Once the water passed through the filter the vacuum was switched off and the funnel was filled with a desired amount of G.O. suspension (± 1mL for 2.1 μm and ± 4 mL for ≤ 1 μm) obtained from Graphene Supermarket (50 mg/L diluted with deionised water). To filter the G.O. suspension vacuum was applied using water aspirator (0.460 bar); the vacuum was measured using manometer (FB57057 Fisher Scientific). As the liquid passed through the PVDF a graphene oxide film was deposited on the surface. On completion of the filtration, the three piece filter funnel was disassembled and the membrane was dried for at least 2 days at room temperature. This produced golden-brown graphene oxide coating on a PVDF polymeric support. The thickness of the membrane was controlled by changing the amount of the G.O. used to produce the film.

The concentration of the G.O. suspension was determined by measuring the weight gain of a membrane support after G.O. coating with a known volume of G.O. suspension. A fresh PVDF membrane was weighted using a Mettler Toledo AB 304 S microbalance with an accuracy of ±0.1mg before and after the coating process described in Membrane Coating section. The concentration of the GO solution was calculated using Equation 62:

$$C_{G.O.} = \frac{\Delta m}{V_{GO}}$$ Equation 62

Where Δm is the weight difference (mg), $V_{G.O.}$ is the suspension volume used to produce a membrane (L), and $C_{G.O.}$ is the concentration of the G.O. solution (mg L^{-1}).The thickness of the films was calculated by dividing the mass placed on the support polymer by the surface area coated and the G.O. density (1.8 g cm^{-3}).[61]

3.2   Pervaporation Cell

In-house built pervaporation cell (Figure 19 and Figure 20) consists of two chambers, permeate (1) and process (7), separated by a membrane (5). The process side is fitted with two 1/16" tubes which serve as inlet and outlet. The membrane saddle disk (6) was designed to accommodate a G.O. membrane and a 1.5 mm thick rubber O-ring (5), porous stainless steel disk (4) and a perforated stainless steel support (3). Upon assembly all parts sit at the same height as the top of the membrane saddle disk. Stainless steel support is then gently compressed by O-rings located in a compression disk (2). The main core is sandwiched by permeate side (1) and compressed using screws. The part breakdown is shown in Figure 20. A detailed set of pervaporation cell drawings is shown in Appendix C.
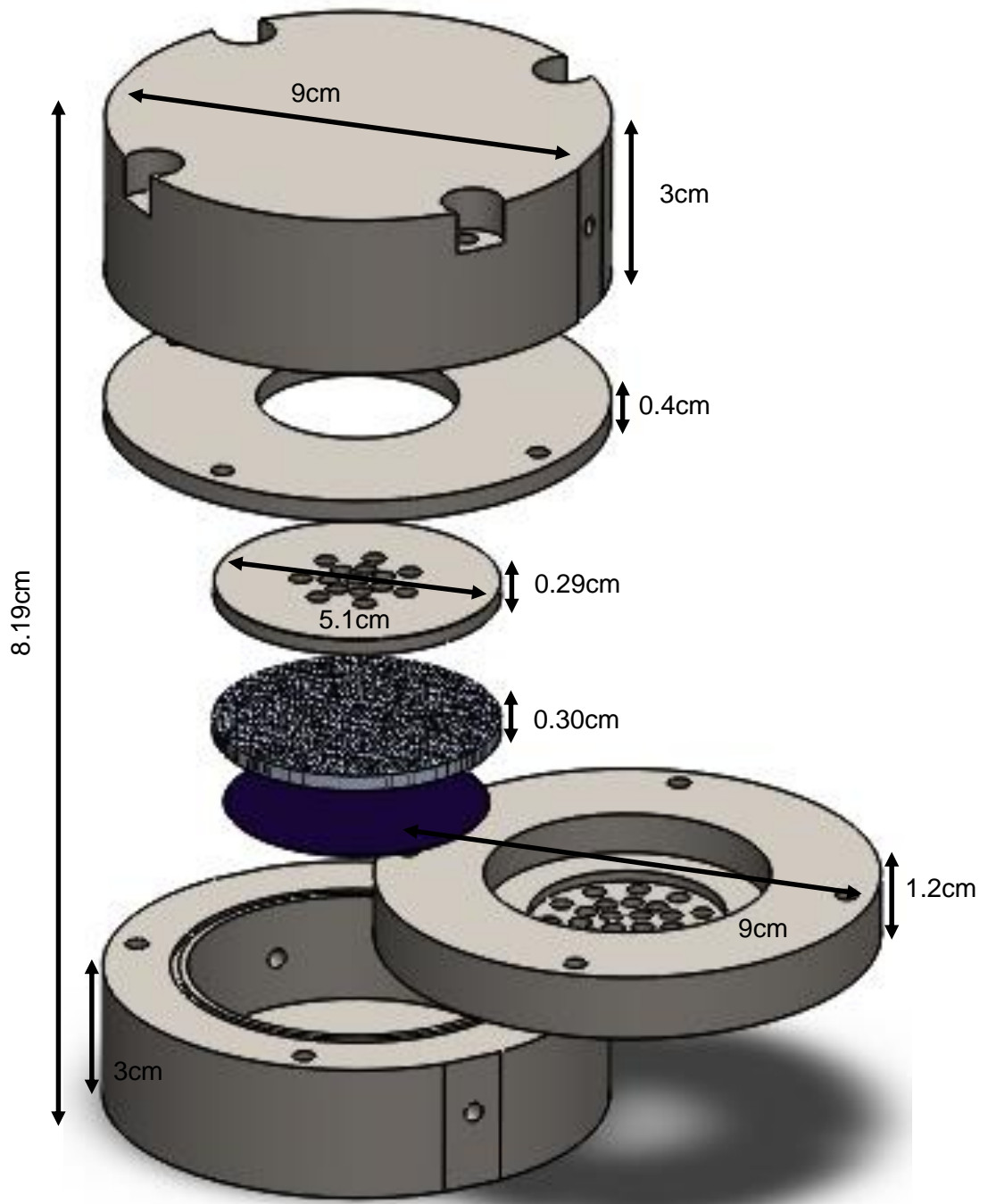
Figure 19 Pervaporation cell computer design

Figure 20 – Pervaporation cell disassembled view

Table 13-Pervaporation cell component list

Notation	Description
1	Permeate side
2	Compression disk
3	Stainless steel support
4	Porous stainless steel disk
5	G.O. membrane
6	Membrane saddle
7	Process side

It is important to mention that G.O. membranes are brittle and apparatus must be assembled with extreme care. Sizeable applied force deviations around the membrane produce cracks on the periphery. The quality of the membrane surface and the seal around can be quickly checked by applying vacuum on the permeate side. If a vacuum cannot be produced the membrane in use most likely has a crack inflicted by an over tightening the pervaporation cell.

3.3   General Procedure

The pervaporation setup diagram used in all experiments is shown in Figure 21, an image of a laboratory pervaporation setup is shown in Figure 22. The experimental setup was composed: i) a conical flask (250 mL) which was used as a feed tank (T1) ii) a pump P1, (Knauer Smartline two piston pump) to circulate the fluid through the cell, iii) a back pressure regulator BPR (2.8-5.2 bar) was used to keep the system from boiling, (iv) in-house developed agitated stainless steel pervaporation cell PERVAP (74 mL, 9.1 cm^2 active membrane surface area). Agitation in the cell was provided by a magnetic stirrer bar rotating at 900 rpm and iv) the permeate side was connected to two cold traps TRAP1 and TRAP2 which were set up in parallel allowing two separate vacuum lines to be open independently, which ensured continuous operation. Liquid nitrogen was used as a cooling liquid for the permeate condensation (-195°C). The vacuum side pressure was set at <5 mbar at all times using vacuum pump P2, (EDWARDS RV3).

A conical flask, T1, was filled with the desired amount and composition solution ±2 mL followed by an initiation of vacuum on a permeate side using EDWARDS RV3 vacuum pump, P2. Once < 5mbar pressure was reached on the vacuum side of the pervaporation cell the process fluid pump (P1) was used to fill the process side with the solution of interest at 15 mL min^{-1}. Fully assembled pervaporation cell was then placed in a hot oil or water bath set at an experimental temperature. This was followed by approximately 1 hour of pre-equilibrium stage, allowing pervaporation cell to reach process temperature and pervaporation flux gain steady state. Thereafter, samples were taken every 1-3 hours and water content was determined using the analytical equipment described in the 3.9 section. A detailed description of standard operating procedures (SOP) can be found in Appendix D.

The rate of permeation was measured using the following expression Equation 63.

$$J = \frac{m}{A \, \Delta t}$$

Equation 63

Where, J is the permeation flux (kg h^{-1} m^{-2}), A is membrane surface area (m^2), and Δt is a time of pervaporation (h). It is important to note that the pervaporation time interval did not affect the mass concentration on the process side to a meaningful extent, thus the concentration can be assumed to be constant unless stated otherwise.

Pervaporation temperature is one of the several critical parameters in a dehydration process. To keep pervaporation cell isothermal heat transfer has to be adequate to provide energy for water evaporation. This is investigated by considering a THF dehydration study at 70 °C, which resulted in one of the highest permeation fluxes in this pervaporation research.

Table 14-Energy required to evaporate 2.69g of water over 60min of operation

Notation	Value
$E_{(Evaporation)}$ (kJ)	N/A
$\Delta H_{(Evaporation)}$ (kJ kg^{-1})	2206
m (kg)	0.00269

$$E_{(Evaporation)} = m \, \Delta H_{(Evaporation)}$$

Equation 64

Table 15-Heat transfer rate from hot oil bath the pervaporation cell

Notation	Value
$\dot{E}_{(transfer)}$ (kJ s^{-1})	N/A
$U_{(Overall)}$ (kW m^{-2}K^{-1}), Assumed	0.2
A (m^2)	0.0069
ΔT (K), Assumed	2

$$\dot{E}_{(transfer)} = U_{(Overall)} A_{(Area)} \Delta T$$

Equation 65

Table 16-Summary of the heat requirements in a pervaporation process

Notation	Value
$E_{(Evaporation)}$ (kJ)	5.93
$\dot{E}_{(transfer)}$ (kJ s^{-1})	0.0028
t (min)	35

A facile calculation of heat transfer shows that for 60min pervaporation operation 35min are required to provide all the necessary energy to maintain isothermal conditions. Thus, the transfer rate was deemed to be sufficient.
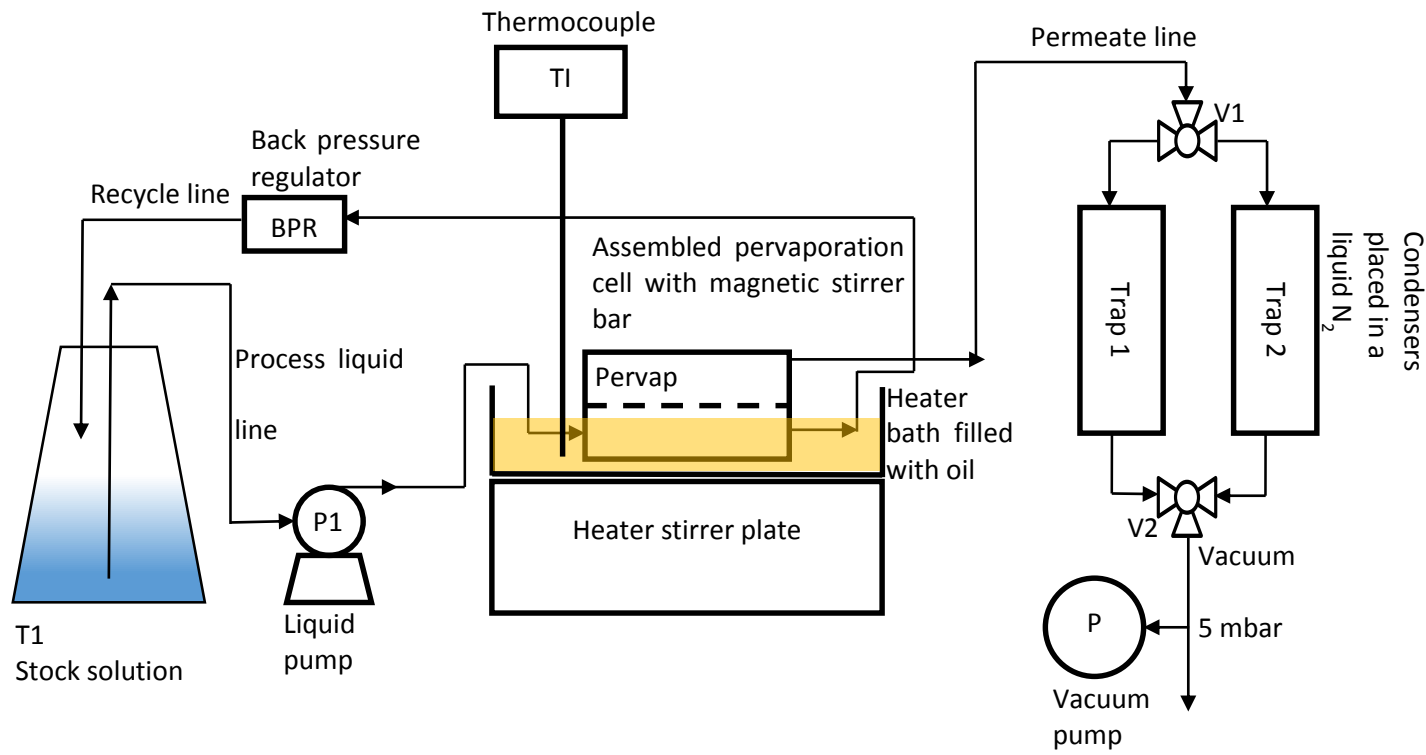
Figure 21 – Detailed pervaporation process drawing
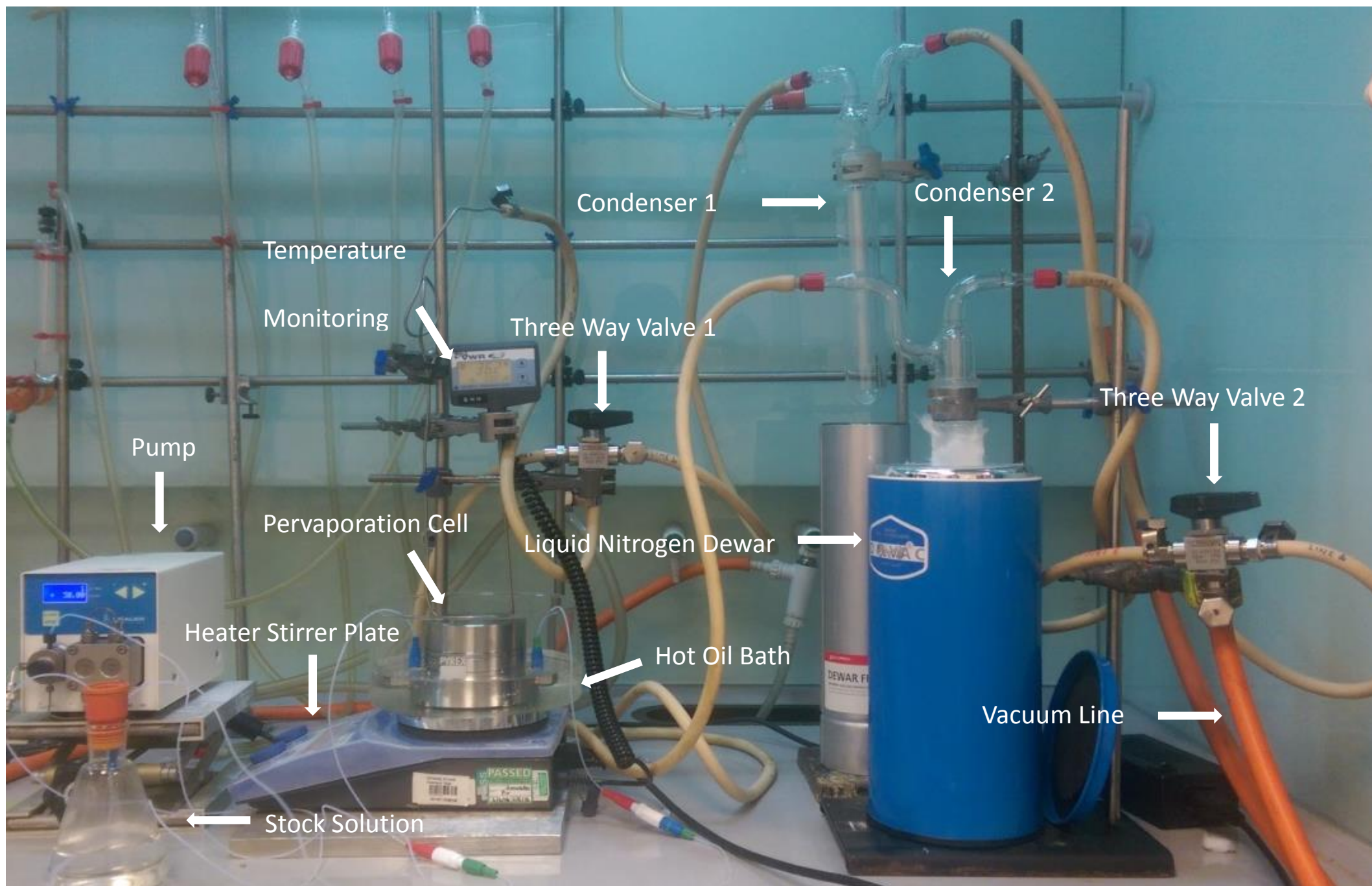
Figure 22 – Laboratory pervaporation setup

3.4 Liquid side mass transfer coefficient study

In the liquid mass transfer coefficient study a general procedure was followed to preload 65 g (65 ± 1 mL) of deionised water and 150 g (190.8 ± 1 mL) IPA resulting in a 30 wt% water/IPA solution. The temperature was set at 50°C for all experiments. The rate of agitation (digitally displayed on the heater stirrer plate) was varied between 0 to 900 rpm. Permeation was measured using three separate membranes. At least 3 samples at each degree of agitation were taken.

3.5 Water/Organic and Organic/Organic separations

All separation studies of the Water/Organic and Organic/Organic components were conducted using the general procedure. The following organic solvents were used in this study: IPA (>99.5wt%, Fischer Scientific), EtOH (HPLC grade, ≥99.8wt%, Sigma Aldrich), THF (>99.5wt%, Fischer Scientific), MeOH (HPLC grade, ≥99.9wt%, VWR International), n-Hexane (95wt%, Fischer Scientific). Selected organic solvent and water were loaded into a conical flask (250 mL) to make up the desired composition mixture with a total volume of 250 mL. Summary of the experimental conditions investigated is shown in Table 17. Multiple membranes were used to determine pervaporation performance at every set of conditions. The supplier and the grade of the chemicals used is summarised in Table 18.

Table 17-Summary of the Water/Organic and Organic/Organic separations

Entry	Estimated membrane (μm)	Component1 (wt%)	Component2 (wt%)	Temperature (°C)
1	0.56-2.1	Water (0-100)	IPA (0-100)	50-80
2	1-2.1	Water (30)	EtOH (70)	50-80
3	1-2.1	Water (30)	THF (70)	50-80
4	2.1	Water (10-30)	MeOH (70-90)	60
5	2.1	MeOH (10-60)	n-Hexane (40-90)	60-80

Table 18-Materials used in the research

Material	Grade	Source
Water	N/A	Deionised
IPA	>99.5wt%	Fischer Scientific
EtOH	≥99.8wt%	Sigma Aldrich
THF	>99.5wt%	Fischer Scientific
MeOH	≥99.9wt%	VWR International
n-Hexane	95wt%	Fischer Scientific

3.6 Peptide dewatering

Peptide dewatering study was conducted following the general pervaporation procedure. In this series of experiments 100 ±1 mL of the selected peptide type and concentration was loaded into a 100 ±1 mL measuring cylinder. During pervaporation process the reduction in the solution volume was compensated by adding DI water amount matching that of the permeate.

In experiments where peptide solution had to be pre-concentrated water was removed using a Heidolph rotary evaporator. The concentrated solution was then used in a pervaporation experiment as described above. Summary of the materials used is shown in Table 19, pervaporation experimental condition are summarised in Table 20.

Table 19-Materials used in the peptide dewatering process

Material	Initial concentration	Source
	Solids in water (wt%)	
Peptide 1	2-8	Industrial Product
Peptide 2	5	Industrial Product
Peptide 3	2	Industrial Product

Table 20-Summary of the peptide dewatering experiments

Peptide	Concentration (wt%)	Temperature (°C)
Peptide 3 (pH = 5.5)	2	70
Peptide 1 (pH = 4)	2	80
Peptide 2 (pH = 9.8)	5	80

3.7   Esterification

A 2.1 µm G.O. membrane was prepared as described in the Membrane Coating section. The membrane was placed in a pervaporation cell followed by a full assembly of the apparatus. A vacuum pump (EDWARDS RV3) was initiated, which produced <5 mbar pressure on a permeate side. Air leakage through the membrane was tested by measuring the pressure (FB57057 Fisher Scientific manometer) on the process side 10-20 min after the initiation of the vacuum pump.

The stock solution vessel was loaded with a 194.96 ± 2 mL (0.719 mol) of long chain carboxylic acid (Croda Product) and 55 ± 1 mL (0.7919 mol) of IPA at room temperature. The liquid was thoroughly mixed followed by addition of 2.05 ± 0.01 g of p-toluenesulfonic acid catalyst. When catalyst was completely dissolved in the reaction mixture the liquid was loaded into a pervaporation cell at room temperature using two piston pumps (Knauer Smartline). Once the liquid was circulating the pervaporation cell was placed in a pre-heated (100°C) hot oil bath with agitation set at 1200 rpm; the stock solution was placed on a stirrer plate set at 300 rpm without heating.

The reaction was analysed by taking 1 ±0.03 mL of stock solution using 0.5-5 mL Eppendorf pipette. The drawn reaction mixture was immediately placed in a 30 mL room temperature IPA loaded with phenolphthalein indicator. The reaction mixture was titrated dropwise with a 0.1 M NaOH aqueous solution and the amount of titrant required to induce a colour change was recorded. The analysis was conducted at the start of every experiment and every hour afterwards.

3.8   Material characterisation

3.8.1   FT-IR

Surface functional groups were determined using an Alpha Bruker spectrometer (Platinum ATR). Prior to the use of the spectrometer the scanning window was thoroughly cleaned with dichloromethane. A sample was placed on an ATR window and clamped down. At least three runs at different membrane locations were taken with each spectra composed of 16 scans which were averaged. Between every sample measurement the equipment was cleaned and background was rescanned.

In preparation of the ATR all membranes were washed with DI water and IPA. Membranes were allowed to dry for at least 4 days at room temperature unless stated otherwise.

A G.O. only sample was prepared by removing water with a rotary evaporator from highly concentrated G.O. solution (5 g L^{-1}, 0.5-5 µm flake size, 79 wt% Carbon, 21 wt% Oxygen, >60% single sheets) purchased from Graphene-Supermarket.

3.8.2   Thermal Properties

Thermal properties were studied using DSC (TA instruments Q20) and TGA (TA instruments, Q50). The samples were weighted using Mettler Toledo (AB304-s) microbalance (±1mg). Both analyses were conducted at a 5°C min^{-1} heating rate.

3.8.3   SEM and EDX

Visual analysis of the G.O. membrane was performed using SEM (Hitachi SU8230 coupled with Oxford instruments Aztec EDX). A small piece of used G.O. membrane was ascertained by cracking the membrane in a liquid nitrogen. The collected samples were placed on a number of SEM holder plates. One side of the sample was covered by a carbon glue connecting the surface of the membrane to the metal support of the SEM holder. All membranes were kept in a desiccator (30 mbar) for at least 4 days prior to imaging to remove all of the residual solvents.

3.8.4   Contact Angle

Prior to analysis membrane surface was cleaned using DI water and IPA. Clean membranes were allowed to dry for at least 4 days prior to the contact angle measurements. In its natural state used G.O. membranes were slightly bent, this was rectified by gluing the bottom of the G.O. membrane surface (PVDF) onto a glass slide using double sided tape. Once the measurement device was calibrated a glass slide with a G.O. membrane was placed on a sample stage and at least 5 drops of DI water were placed on a surface for the measurements using Cam 200 KSV tensiometer.

3.9   Water Analysis

3.9.1   Karl Fischer analysis

Karl Fischer (Mettler Toledo, DL38) was coupled with Hydranal 5 titrant and Hydranal solvent (Fluka analytical). The apparatus had 5 mL burette capable of analysing water content in a range of 1-100 wt%. Prior to analysis the equipment was calibrated using 100 mg of DI water or 1 mL of Hydranal Water Standard 10 (1 wt% water in an organic solvent). The calibration samples and permeate samples were weighted using Mettler Toledo (AB304-s) microbalance (±1mg). Every sample was analysed at least three times and the average was tabulated as a water concentration.

3.9.2   GC analysis

Gas chromatographer (HP6890 Series) was used to determine the concentration of the organic component. The analytical equipment was equipped with a HP 5 column, 30 m length, 0.32 mm diameter, and 0.25 µm film thickness. Sample (1 µL at 1:100 split). The sample was injected at 250°C followed by a hold at 40°C for 5 minutes, the temperature was then raised by 50°C min^{-1} to 200°C and held for 1 min.

Prior to the analysis of the permeate samples a calibration curve was prepared. Permeate sample organic component response area was then compared against the calibration curve and the amount of the organic compound was ascertained. From this result water concentration in the permeate was calculated.

3.9.3   Refractometer

Water concentration in the permeate was also measured using refractive index using a refractometer (Bellingham and Stanley). Several drops of the permeate were placed on the refractometer glass which then clamped with a metal lid at room temperature. The concentration was determined by measuring the deviation of the refractive index from the 1.3333 value.

4   Organic Solvent Dehydration

Organic solvent recovery is a pressing issue in many different industries: pharmaceutical, bulk chemical, speciality chemicals and electronics. Two strong arguments can be made regarding the need to develop safe, clean and efficient ways to recover organic solvent waste streams. There is a large commercial benefit associated with the solvent recovery which is especially prominent in industries where copious amount of organic solvent is used, and its price places is a significant contribution to the overall final product cost. [95] The second argument is concerned with the environmental legislation which is becoming stricter regarding chemical industry emissions. Naturally, the recovery of the waste solvent stream would minimise the chemical process impact on the environment.

Typically, distillation is used to recover organic components. However, water/organic compound solutions often form azeotropic mixtures, which have identical vapour and liquid compositions at a set boiling point. This makes it impossible to separate compounds by traditional distillation and requires a more complicated process to be applied. Pervaporation is seen as an energy efficient and cheap alternative to distillation, which is not limited by the azeotrope formation.

This chapter is focused on the G.O. membrane pervaporation experimental setup and solution-diffusion model validation. The experimental setup is validated by studying liquid turbulence effects on the liquid mass transfer coefficient using a Water/IPA solution. The mathematical solution-diffusion model is investigated by varying i) process fluid temperature, ii) membrane thickness, and iii) mole fraction of water in the process fluid. This chapter covers three common aqueous organic solvent mixtures: i) IPA, ii) EtOH, and iii) THF.

4.1   Experimental setup validation

There is a close connection between the overall rate of the mass transfer in a membrane process and the hydrodynamic conditions in the system. The governing equations linking hydrodynamics and the overall mass transfer have been reviewed previously in Chapter 2. [11, 86, 88, 91, 96, 97] Before measuring pervaporation performance it is crucial to establish the conditions where the rate of permeation is limited by mass transfer through the membrane. In this research, influence of hydrodynamics on the rate of pervaporation was investigated using a 2.1 μm thick G.O. membrane. The process solution was composed of 30wt% water in IPA at 50°C. The turbulence of the fluid on the process side was assumed to be predominantly controlled by two factors i) rate of agitation and ii) pump flow rate. The liquid flow rate was kept constant and it was assumed to have

negligible effects on the total fluid turbulence in the presence of agitation. Furthermore, the liquid concentration was kept constant by replenishing the depleted water in the process solution by adding fresh DI water. It was assumed that the pervaporation was not heat transfer limited as the amount of water permeating was small (1 – 2g) and the operation time was between 1 – 2 hours.

To study the effects of turbulence on the permeation the rate of agitation was altered. The rate of permeation was plotted as a function of agitation as shown in Figure 23. The rate of permeation gradually increased from an average value of 0.16 kg h^{-1} m^{-2} to 0.73 kg h^{-1} m^{-2} while increasing the RPM from 0 to 550 respectively. The increase was associated with the shifting rate of mass transfer limiting step. At a low rate of agitation, the rate of pervaporation was dominated by the liquid side mass transfer coefficient. As the rate of agitation was increased the liquid side mass transfer boundary layer shrank. [95] At higher rates of agitation (>550 RPM) the rate of permeation has gained a steady value of $\cong$ 0.74 kg h^{-1} m^{-2}. This marked a region where the rate of permeation was limited by the membrane mass transfer coefficient, an inherent property of the material. It is impossible to completely eliminate the liquid side mass transfer coefficient and even in completely turbulent conditions a laminar sub layer exists. [95] However, in the region of high agitation (>550 RPM) it was assumed that the liquid mass transfer coefficient becomes insignificant. The resistance of the porous support layer was also assumed to be insignificant.
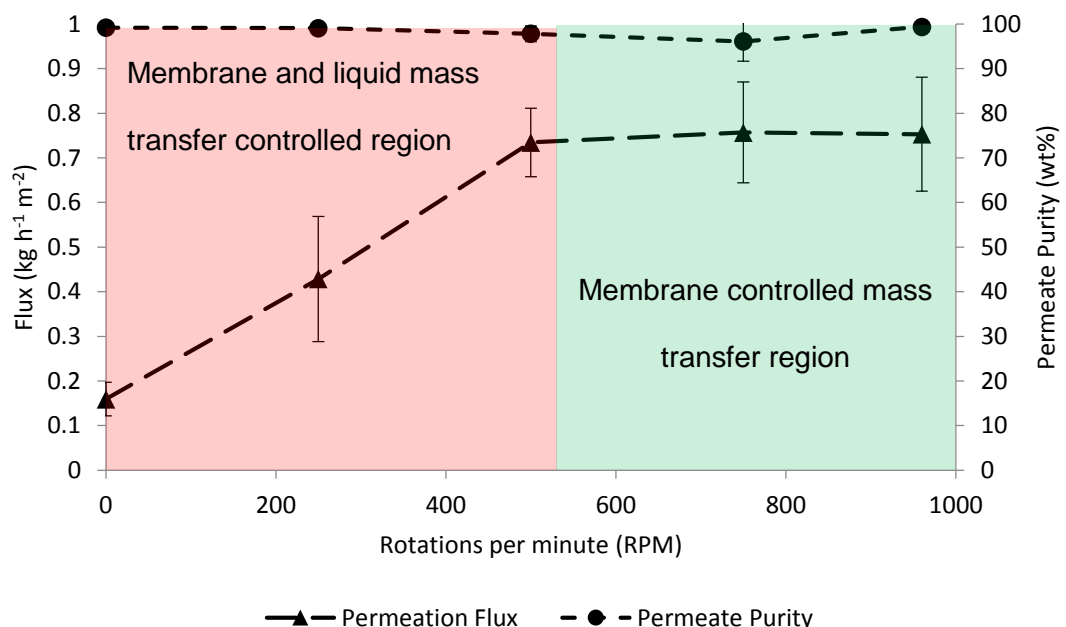
Figure 23-Pervaporation flux change with respect to the change in agitation, water/IPA (30 / 70wt%), 50°C, 2.1μm.

To calculate individual mass transfer coefficients of the pervaporation process, several assumptions are made: high agitation region (>550 rpm) is controlled by the membrane mass transfer, thus the liquid boundary layer resistance becomes irrelevant and cannot be separately determined. This assumption simplifies previously shown resistance in series model to Equation 66

$$J = \frac{1}{R_{Membrane}} K_s^G (P_{w.L} - P_{w.P}) = k_{m.p}(P_{w.L} - P_{w.P})$$

<div align="right">Equation 66</div>

$$k_{m.p} = \frac{D_{wm} K_s^G}{y_m}$$

<div align="right">Equation 67</div>

Where, $k_{m.p}$ is membrane mass transfer coefficient (kg bar^{-1}s^{-1}m^{-2}), y_m is membrane thickness (m) and D_{wm} is effective water diffusion coefficient in the membrane matrix (m^2 s^{-1}) K_s^G is gas sorption coefficient (kg bar^{-1}m^{-3}).

To determine conventional mass transfer coefficient, the water vapour partial pressure term is replaced by mass concentration as a driving force. The expression is then further simplified by ignoring the water concentration on the permeate side resulting in a final expression Equation 68. The simplified expression was then used to calculate membrane mass transfer resistance.

$$J = \frac{D_{wm} K_s^L}{y_m} \rho_{w,LM}^L = k`_m \rho_{w,LM}^L$$

<div align="right">Equation 68</div>

Where, K_s^L is liquid partition coefficient (dimensionless), $k`_m$ is membrane mass transfer coefficient (m s^{-1}), and $\rho_{w,LM}$ is water concentration in the bulk solution (kg m^{-3}). For the ease of calculation, the liquid partition coefficient from here onwards is combined with the mass transfer coefficient.

At the lower rates of agitation (<550 rpm) the liquid boundary layer becomes a large part of the overall resistance and thus can no longer be ignored. The pervaporation flux

equation then has to be extended to include liquid boundary layer resistance Equation 69.

$$J = \frac{1}{\frac{1}{k_l} + \frac{y_m}{D_{w_m}}} \rho_{w,LM} = \frac{1}{\frac{1}{k_l} + \frac{1}{k_m}} \rho_{w,LM}^L = k_{ov}\rho_{w,LM}^L \qquad \text{Equation 69}$$

When the overall and the membrane mass transfer coefficients are known the liquid boundary layer mass transfer coefficient can be calculated using

$$k_l = \frac{k_{ov}k_m}{k_m - k_{ov}} \qquad \text{Equation 70}$$

Water mass transport coefficients in the liquid and membrane layers were calculated from experimental data and are shown in Table 21. It is interesting to note that the initial research has pointed out that G.O. membrane held no resistance to water diffusion.[1] Unfortunately, this was only an interpretation of limited pervaporation experimental data. The water mass transfer coefficient in the membrane matrix at 50°C is of a typical magnitude found in pervaporation processes. Water diffusion in the liquid boundary layer was also of a similar value found in the previous diffusion research.[98] The distribution of the mass transfer coefficients show a very strong influence of a water boundary layer resistance when no agitation is present.as the agitation is increased the liquid boundary layer mass transfer coefficient increases from $2.21*10^{-7}$ m s^{-1} to $2.75*10^{-5}$ m s^{-1}and presents only 3% resistance to the overall mass transfer in a pervaporation operation.

Table 21- Mass transfer coefficients, water/IPA (30 / 70wt%), 50°C, 2.1μm.

Agitation (rpm)	Flux (kg h^{-1}m^{-2})	$k_{ov} \times 10^{-7}$ (m s^{-1})	$k_m \times 10^{-7}$ (m s^{-1})	Resistance (%)	$k_l \times 10^{-7}$ (m s^{-1})	Resistance (%)
0	0.16	1.74	8.24	21.14	2.21	78.86
250	0.43	4.67	8.24	56.68	10.78	43.32
500	0.73	8.00	8.24	97.09	274.6	2.91

It is frequently suggested that it is important to continue making ever thinner pervaporation membranes.[15, 17, 58, 99] However, the liquid boundary layer mass transfer limitation is often not considered at the membrane design stage. Assuming the liquid boundary layer mass transfer coefficient stays constant and the membrane mass transfer coefficient reduces linearly with a decrease in the membrane thickness. It is possible to calculate how thin the G.O. membrane can be until the liquid boundary layer resistance starts dominating the mass transfer process. The membrane mass transfer resistance contribution to the overall mass transfer process at different membrane thicknesses is shown in Figure 24. A hypothetical pervaporation process is dominated by the membrane mass transfer from 2.1 to 1µm membrane thickness. At a smaller membrane thicknesses liquid boundary layer resistance has a significant contribution. Up to date, the thinnest G.O. membrane tested in a commercial pervaporation unit had 0.097µm thick selective layer.[100] If the membrane would be used in this experiment the liquid boundary layer resistance contribute 39% of the total resistance.
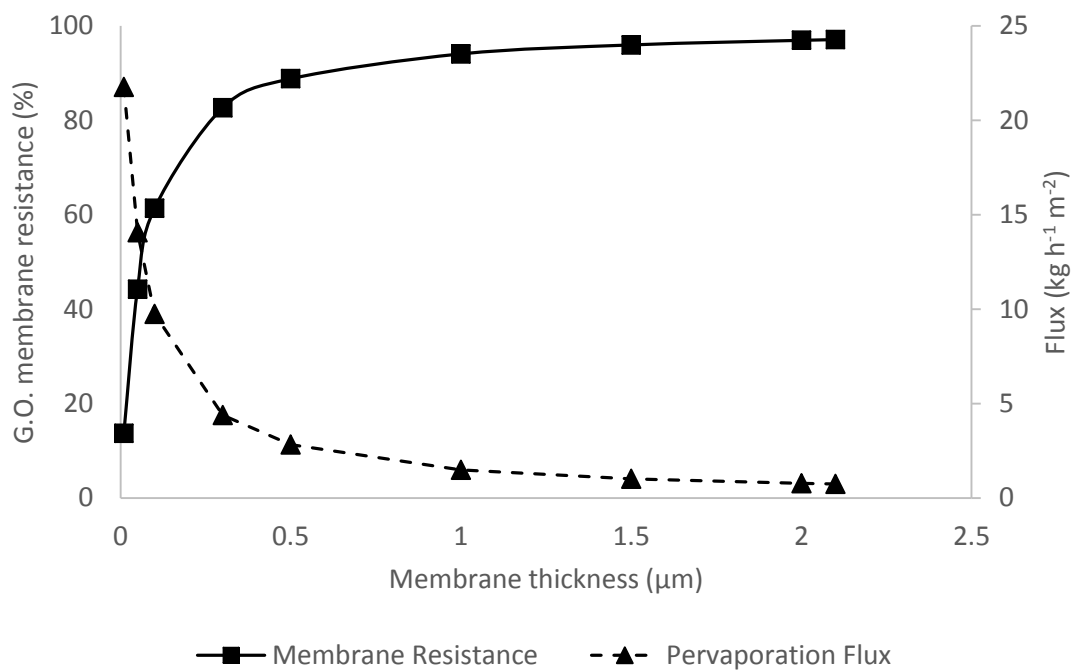
Figure 24- Mass transfer resistance (%) change with respect to the change in membrane thickness, water/IPA (30 / 70wt%), 50°C, 2.1 – 0.01µm

An empirical methodology used to validate the performance of pervaporation equipment is well known.[11] However, the transferability of the liquid side mass transfer coefficient expression is very limited. A similar curve at identical conditions will be obtained only in a similar geometry and size pervaporation cell. A significantly different pervaporation cell design, would require a repeat of all experiments to determine a new membrane limited mass transfer zone.

4.2   G.O. membrane long term performance

The stability of the G.O. membrane was investigated by exposing a 2.1 µm thick G.O. membrane to a 20wt% water in IPA solution at 80°C for 40 hours. The entire study was subdivided into a 7-day consecutive pervaporation experiments. The average and measured values of the permeation flux and permeation purity are shown in Figure 25. The measured pervaporation flux values were scattered probably due to the temperature fluctuations and sample extraction error; thus, the permeation rates were averaged. The declining trend became apparent. During the entire course of the study permeation flux has declined from an average value of 1.28 to 0.82 kg h^{-1} m^{-2}, which corresponds to a loss of 36 % of permeation rate, Figure 26. The permeate purity produced an inclining trend and remained very high in the region of 95.2-99.0 wt%.
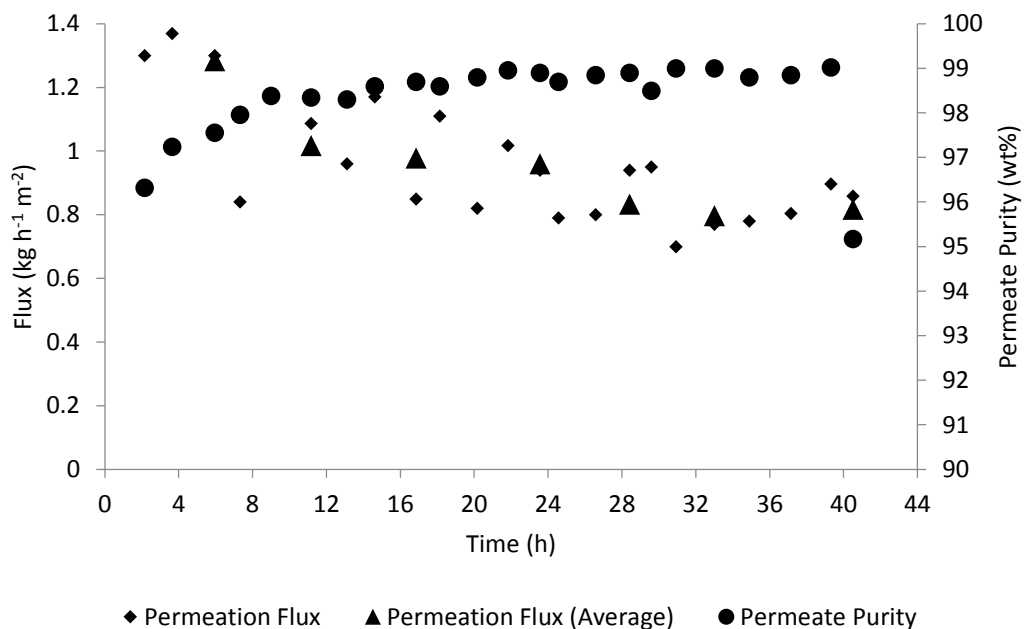
Figure 25-Membrane stability over 7 day period, water/IPA (20 / 80wt%), 80°C, 2.1µm.

▲ Average Permeate Flux   ● Average Permeate Purity
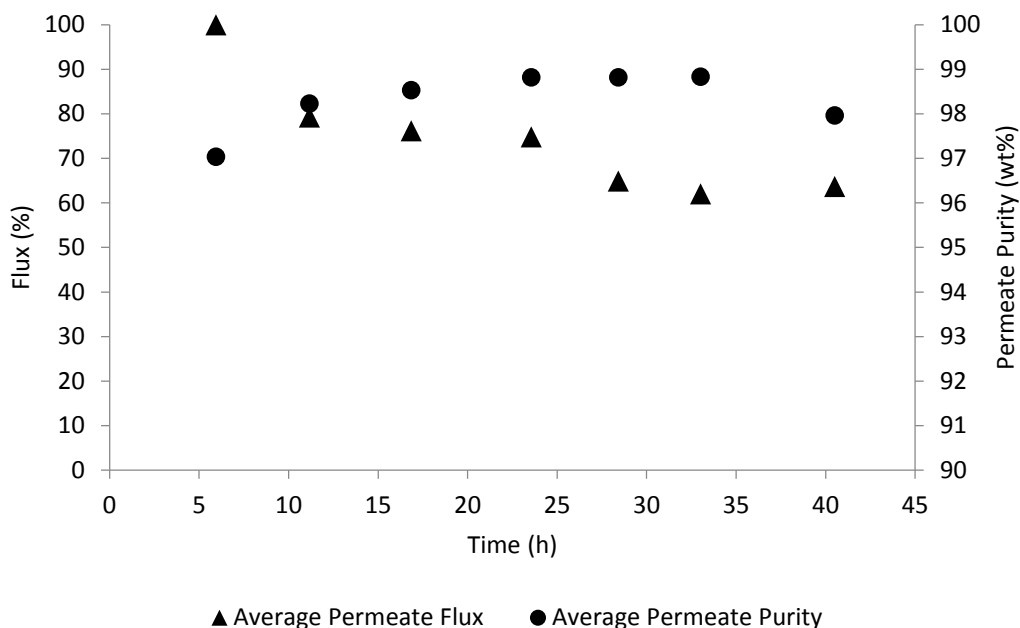
Figure 26-Membrane stability over 7 day period (percent permeation flux values), water/IPA (20 / 80wt%), 80°C, 2.1μm.

The reasons behind the drop in the rate of permeation are not clear. Best to our knowledge, there is no reported case of the G.O. membrane pervaporation degradation in the presence of a water and alcohol. To investigate this in more depth the membrane physical and chemical property changes are studied after exposing the membrane to an alcohol and water mixture. Various analytical techniques were used to study the property change and are discussed in the following sub-section.

4.3 Visual analysis

G.O. membrane surface resistance to an alcohol/water mixture was studied using SEM. Images of a fresh G.O. membrane are shown in Table 22 Entry 1.a and 1.b. The membrane exhibited ridged surface structure and was analogous to the previous research.[101] SEM images were taken of a membrane exposed to a 90% ethanol and 10% water mixture shown in Table 22 (2a, b). The images show a clear surface structure resemblance to unused membrane Table 22 (1a, b), although they appear to be considerably smoother. This suggests that a freshly coated membrane surface contains many poorly adhered graphene oxide sheets which wash away upon exposure to a liquid. However, it does not appear to have any dramatic changes which could be associated with a membrane degradation.

Table 22 - Visual G.O. Characterisation

Experiment Reference.	Conditions and comments	SEM image
1.a	Fresh membrane $(0.21\ mg/cm^2)$ magnified 500 times.	
1.b	Fresh membrane $(0.21\ mg/cm^2)$ magnified 5000 times.	
2a	A G.O. membrane exposed to ethanol water mixture for several hours in a pervaporation cell. Note sharp looking ridges smoothed out. Magnified 500 times	
2.b	A G.O. membrane exposed to ethanol water mixture for several hours in a pervaporation cell. Magnified 5000 times	
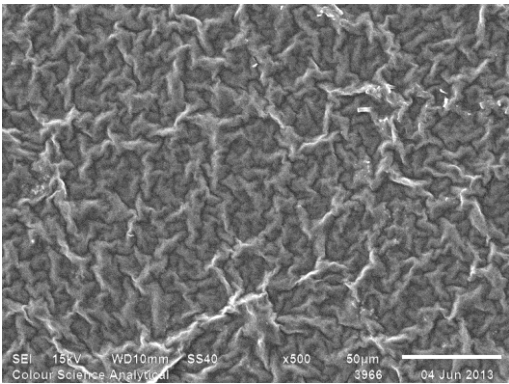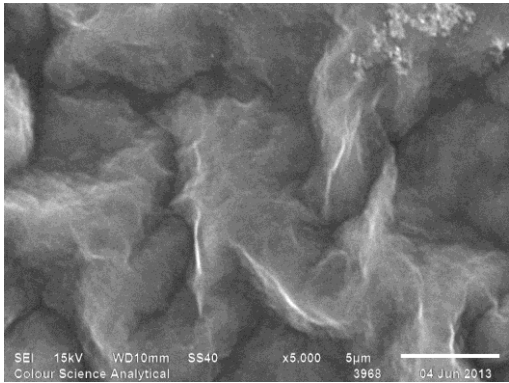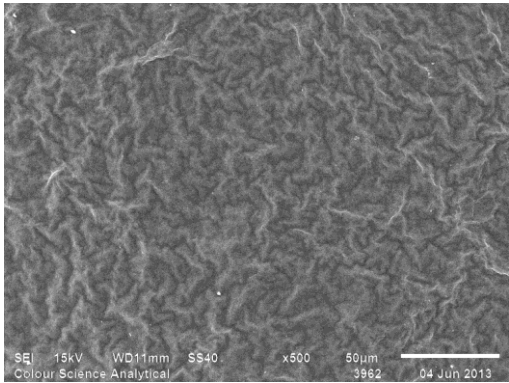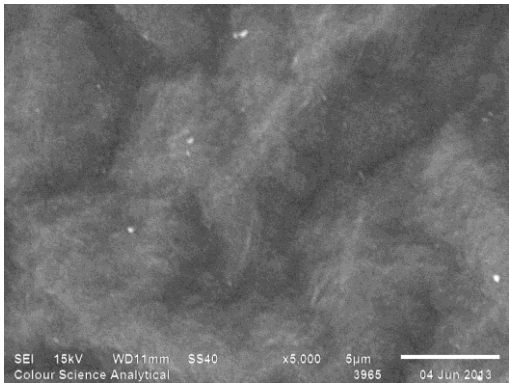
4.4 Thermal degradation

Thermal stability of the G.O. is of paramount importance for reliable a membrane pervaporation performance at elevated temperatures. Naturally, it is desirable to have a membrane material that is stable over a wide temperature range since typically pervaporation operations are carried out below 100°C. Thermal stability of the material was studied using TA instruments DSC (Q20) and TA instruments TGA (Q50).
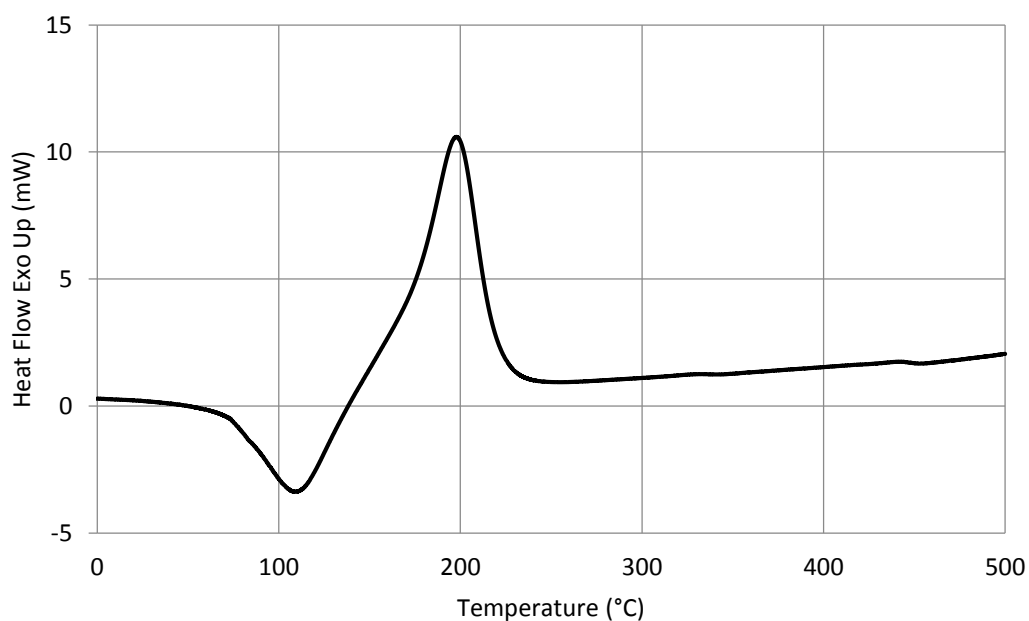
Figure 27-DSC scan in a 0-500°C temperature range at a 5°C per minute heating rate
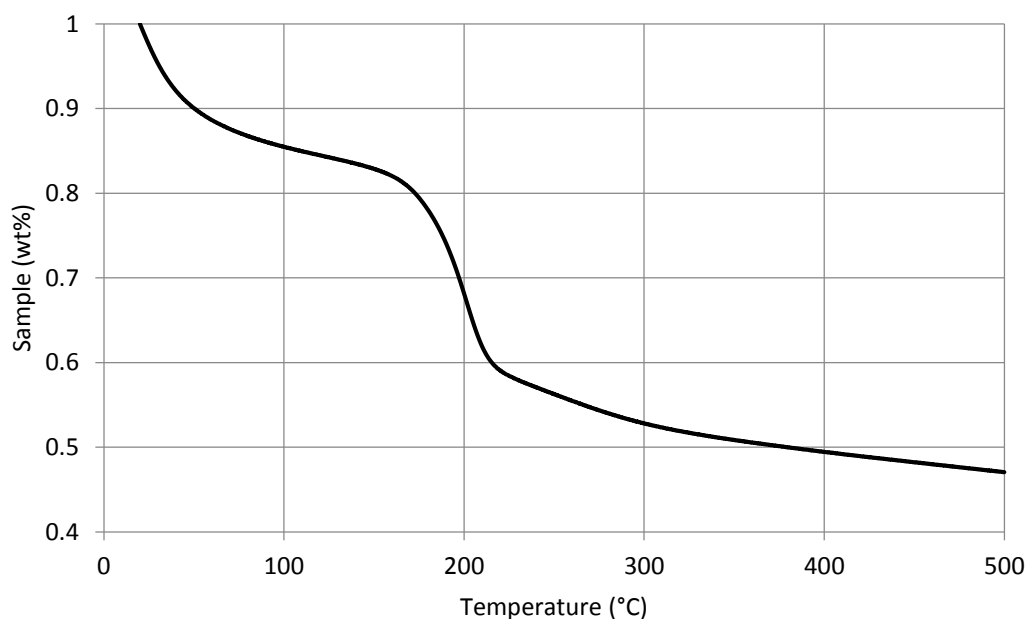
Figure 28-TGA scan in a 0-500°C temperature range at a 5°C per minute heating rate

There was approximately 17% mass loss in a 50 – 160°C temperature range with an endothermic energy peak at 109°C. This mass loss was assigned to the loss of adsorbed water and a small loss of $C - OH$ groups. This temperature region is also known to be favourable for a $C = O$ group formation in a multi-layered G.O.[102, 103]

An exothermic event in the 160-250°C temperature range resulted in a ≈27% mass with the event peaking at ≈197°C. This was allocated to a pyrolysis of labile groups resulting in a CO and CO_2 release. The temperature region is known to be favourable for the formation of $C = O, C - O$ and a loss of the epoxide, $C - OH$, and $COOH$ groups.[103] The remainder of the TGA profile had a much shallower gradient trending downwards. This was associated with a gradual loss of the following functional groups, $C - O, COOH, C - OH,$ and $C = O$ tightly packed in a G.O. lattice. DCS and TGA profiles were consistent with previous research reported in the literature. [102, 104-106] [103]

4.5 XRD analysis

G.O. is known to graphitise in the presence of pure ethanol at elevated temperatures.[107] A sufficient loss of functional groups would lead to a reduction of the interlayer spacing and available space for water permeation. It is also known that there is no water transport through a reduced G.O. material.[1] Thus, a reduction of the G.O. membrane would be detrimental to the pervaporation performance.

To study the effects of the water/alcohol mixtures on G.O. internal structure an interlayer spacing was measured using XRD of i) Graphite ii) PVDF (a support) film, iii) new G.O. membrane (2.1 μm) and iv) G.O. membrane (2.1 μm) used in a 7 day pervaporation operation, Figure 29. The corresponding material d-spacing was calculated using Bragg Law, Equation 71.

$$\lambda_l = 2d sin(\Theta) \qquad\qquad \text{Equation 71}$$

Graphite powder exhibited a strong, sharp peak at 25.5° (0.35 nm d-spacing), corresponding to a 002 plane family. A supporting PVDF polymer XRD pattern showed very broad peaks at 17.97°, 18.37°, 20.0°, and 26.88°. This indicates varying sizes in crystalline regions. The pattern was a match to a previous XRD study of a PVDF material.[108] A scan of a G.O. membrane includes patterns of graphene oxide and underlying PVDF support. Due to oxidation the interlayer spacing of the G.O. was larger than the graphite. An unused membrane had a d-spacing of 0.811 nm (10.9°) more than double that of the graphite powder. A membrane used in the 7-day pervaporation experiment exhibited an interlayer spacing of 0.842 nm (10.5°). Thus, indicating no apparent interlayer spacing change after 7-days exposure to an alcohol water mixture. No peak growth in a graphite region (25.5°) was observed thus excluding any potential loss in pervaporation flux due to internal graphitisation of the material which was previously suggested in a study on G.O. thermal reduction in methanol (MeOH) and EtOH.[107]

The study was extended to thinner membranes (1000 nm), Figure 30. The membrane was used in pervaporation of water/Ethanol solution for several days at 50 – 60 ° The XRD pattern of the membrane was a match of a pattern of the PVDF with an extra peak at 10°, which corresponds to the graphene oxide d-spacing of 0.84 nm. No significant graphitisation of the material was observed.
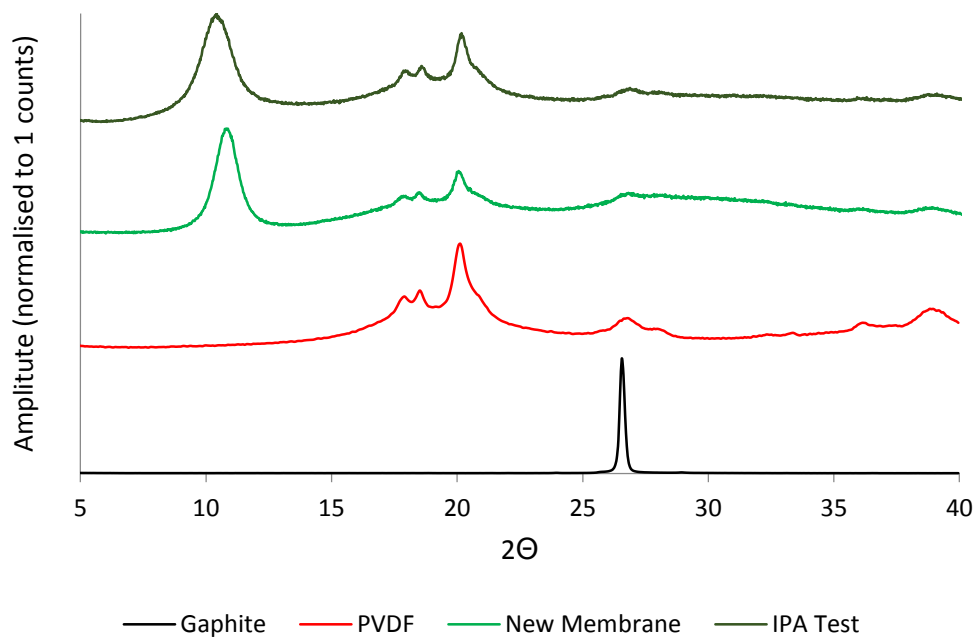
Figure 29-XRD patterns of i) Graphite, ii) PVDF, iii) New Membrane, and iv) G.O. membrane tested in a 7 day pervaporation process.
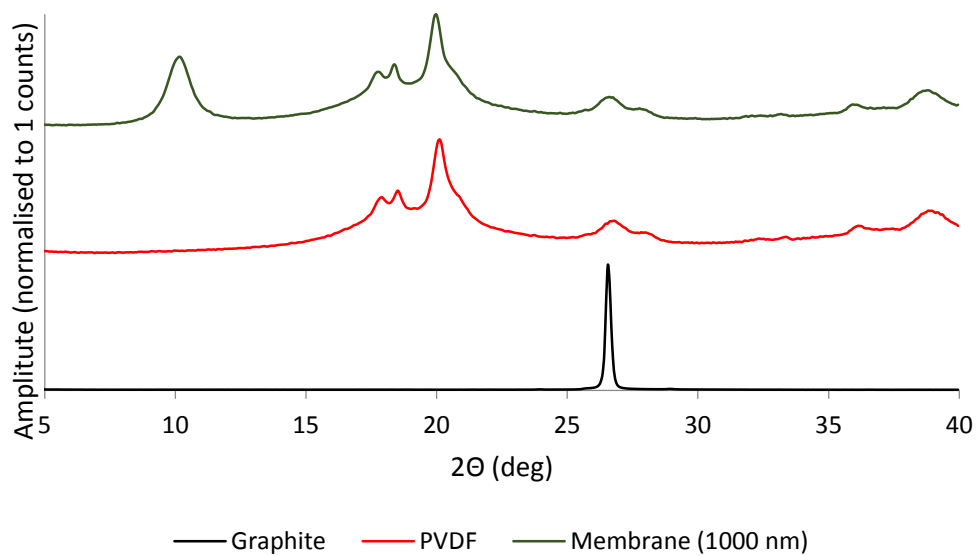
Figure 30-XRD patterns of i) Graphite, ii) PVDF, and iii) G.O. Membrane (1 μm)

4.6 FT-IR analysis

Numerous authors have studied graphene oxide using IR spectroscopy.[60, 68, 109, 110] Historically, there has been some debate over the peak assignments. The reason of disagreement is the presence of a very broad peak in a $2800 - 3800$ cm^{-1} range due to adsorbed water, which in turn can conceal or partially block other peaks.[60]

In this study, G.O., functional groups were investigated using Bruker Alpha ATR-IR spectrometer, Figure 31. The peak at $2800 - 3800$ cm^{-1} was assigned to a hydroxyl group stretching and intercalated water molecules.[110] The nature of such a broad peak can be explained by hydroxyl groups attached to the carbon basal plane in different forms, such as tertiary and secondary alcohols, enols, phenols and carboxylic groups.[110] There is a small, shoulder like, peak at 1713 cm^{-1}. This was assigned to the carbonyl groups present in ketones and carboxylic acids located at the edge of the basal plane.[68] The peak at 1625 cm^{-1} originates from un-oxidised aromatic regions in the structure. The peak at 1218 cm^{-1} was assigned to the $C - O - C$. The fingerprint region was composed of $C - C$ and $C - O$ bonds. [111]
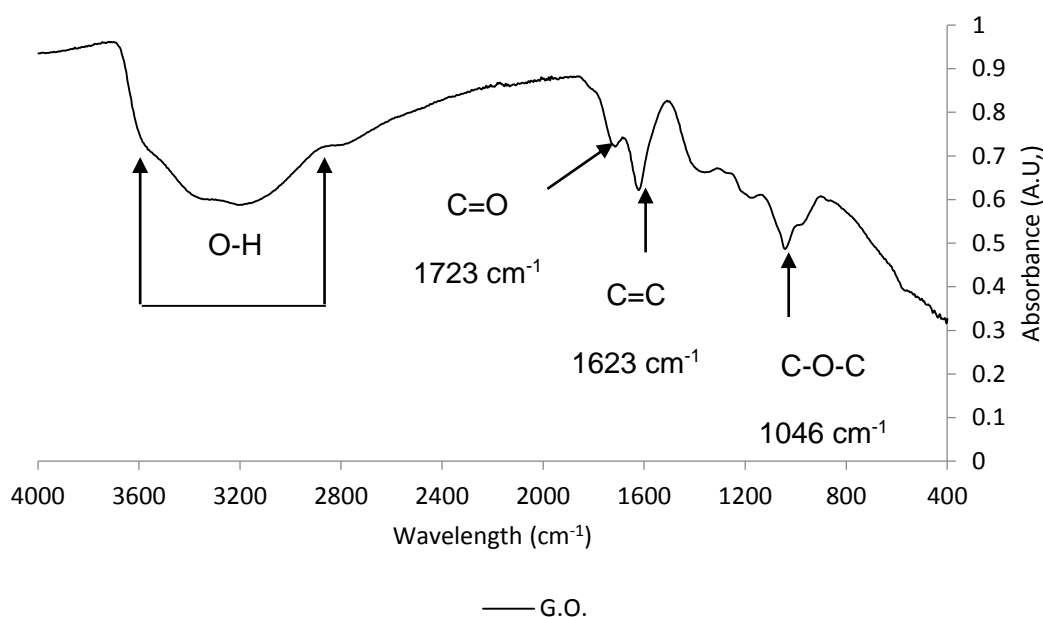
Figure 31- FT-IR of G.O.

FT-IR was used to investigate the surface changes of the membrane used in an IPA/Water pervaporation operation for 7 consecutive days. Membrane functional group changes were assessed against i) G.O. film, ii) new membrane, and ii) PVDF polymeric support shown in Figure 32. The landscape of the PVDF and G.O. film spectra was a match to the previous literature data.[110, 112] The spectrum of the new G.O. membrane was almost a complete match to an unsupported G.O. film. Minute peak differences were

observed in the fingerprint region (400 – 900 cm^{-1}), which are most likely resulting from an underlying PVDF polymeric support. There were no other major differences between the G.O. film and new G.O. membrane IR spectra. A set of three distinct peaks (2950 cm^{-1}, 2919 cm^{-1} and 2845 cm^{-1}) was observed in the used membrane FT-IR scan. Peaks in this region result from C-H stretches (2950-3000 cm^{-1}). The exact same location of the peaks is present in the IPA spectrum, suggesting that the IPA is present on or in the membrane. It is not entirely clear whether IPA has permanently bonded to the G.O. surface or just small amounts of the compound intercalated between the G.O. sheets.
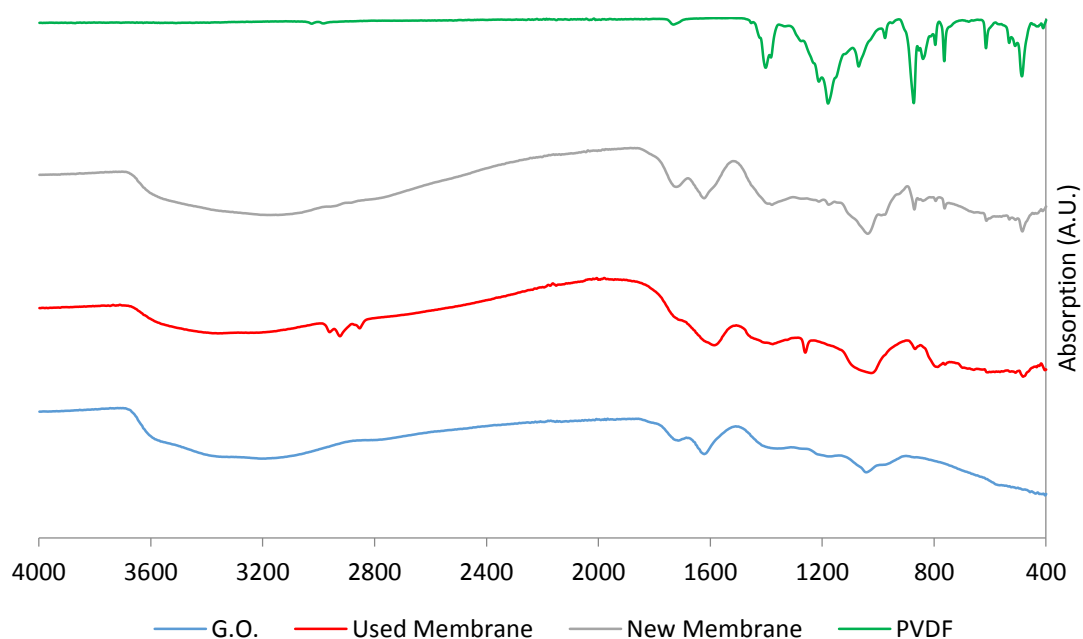
Figure 32-FT-IR of i) G.O, ii) Used Membrane, iii) New Membrane, and iv) PVDF

To rule out the possibility of the additional peaks being an artefact of the intercalated solvent into the G.O. matrix a fresh membrane was soaked in the IPA solution for 24 hours and dried in a vacuum oven for 9 days at 40°C. FT-IR spectrum of the i) soaked membrane, ii) fresh membrane, and iii) used membrane is shown in Figure 33. There were significant changes in the fingerprint region among all of the spectra. No IPA peaks were observed in the soaked membrane FT-IR scan. This supports the argument that the IPA has permanently attached to the G.O. surface during pervaporation operation.
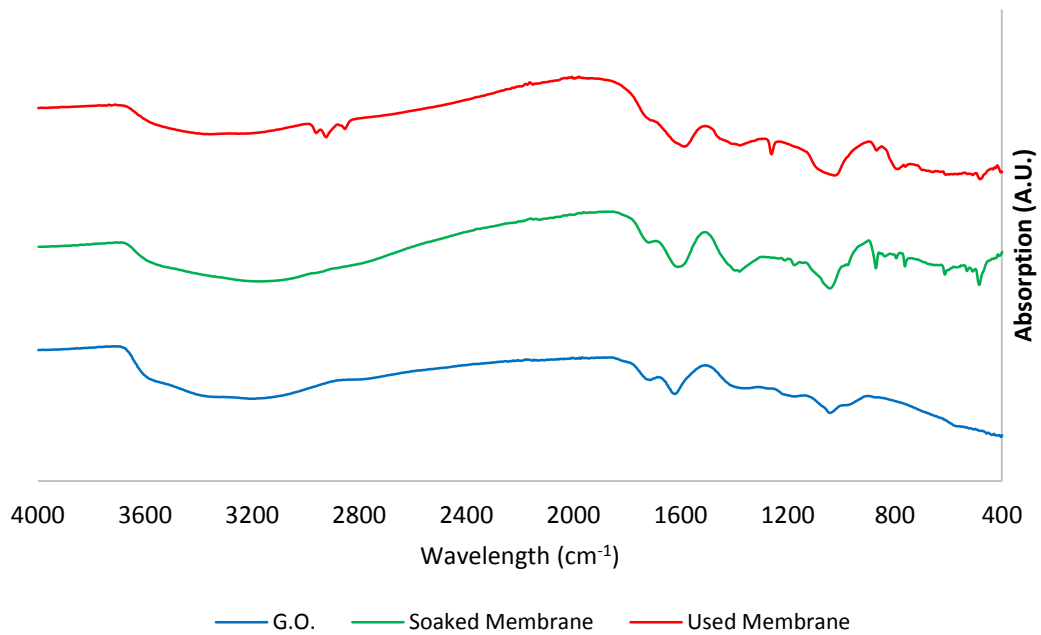
Figure 33-FT-IR spectra of i) G.O., ii) Soaked Membrane, and iii) Used Membrane

Membrane surface hydrophilicity affects water partitioning into the membrane matrix, permanent bonding of the IPA to the surface of the G.O. can change the hydrophilicity and in turn negatively affect water partitioning. A water droplet contact angle measurement is an easy and fast way to assess the surface hydrophilicity.[97] If a water droplet has a contact angle smaller than 90° the surface is said to be hydrophilic (high wettability), the opposite is true if the surface contact angle is less than 90°. Images of a water droplet on a fresh G.O. membrane and the membrane used in the 7 days dewatering process are shown in Figure 34 a) and b) respectively. Oxygen groups on the graphene surface have been known to introduce a hydrophilic property to the material. The contact angle of water on the fresh G.O. surface was 65.88° and 65.63°, confirming the hydrophilic nature of the surface. The contact angle of a water
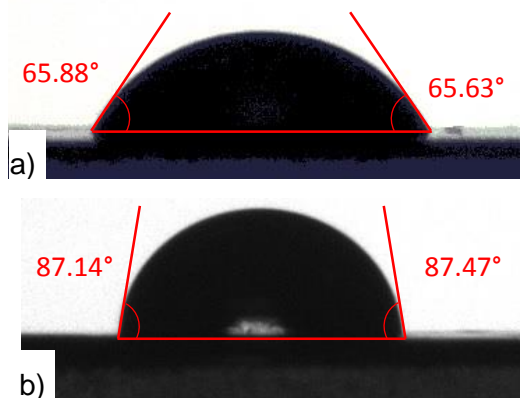
Figure 34 – Water contact angle on the a) fresh G.O. membrane, and b) used G.O. membrane

droplet on the used membrane surface has significantly increased to 87.14° and 87.47°. This suggests a large surface chemistry change has taken place during the pervaporation operation, which has significantly reduced G.O. membrane hydrophilicity. In light of G.O. material surface chemistry instability at elevated temperatures the

increase in the contact angle is most likely the results of the IPA reaction at the membrane surface and previously reported material thermal degradation. The reduction in the surface wettability would explain the drop in the rate of permeation over time. As the membrane becomes less hydrophilic water finds it harder to wet the surface and intercalate between the G.O. sheets.

4.7 Solution-diffusion model validation

It is accepted that the solution-diffusion model describes pervaporation process, Equation 72. In this model the transport of the permeating species is a product of the permeability coefficient and partial pressure difference across the membrane. To get a detailed view of the membrane material performance, typically pervaporation flux change with respect to the change in process parameters is studied.

$$J = \frac{D_{wm}K_s^G}{y_{GO}} x\, \gamma 10^{A - \frac{B}{C+T}}$$

Equation 72

From Equation 72, it is apparent that the change in the rate of pervaporation can be altered in three ways: i) varying temperature of the operation, ii) changing membrane thickness and iii) varying the mole fraction of water in the process solution. In typical membrane permeation performance studies pervaporation flux change with respect to the change in temperature and mole fraction is reported. [15, 71, 73, 100] In this work the influence of all three variables on the rate of permeation are studied.

4.7.1 Temperature effects

The feed temperature is a crucial variable in a pervaporation process as it influences both separation quality and flux. To gain an insight into G.O. membrane performance with respect to the temperature change, three common binary solvent systems were tested: i) 30wt% Water/IPA, ii) 30wt% Water/EtOH, and iii) 30wt% Water/THF.

Water/IPA solution was tested using a 2.1 µm thick membrane in a temperature range of 50 – 70 "C. The pervaporation flux through a G.O. membrane was first plotted against the water vapour partial pressure, Figure 35. The permeate flux increased linearly with the driving force whilst maintaining the purity of water on the permeate side at high levels; between 97.9 and 99.5 wt%. In all experiments the observed permeate quality was considered to be very pure and is of comparable purity with other research or commercial membranes.[76, 113] The variations in water purity did not follow any trend and were most likely caused by a variation in the membrane quality.
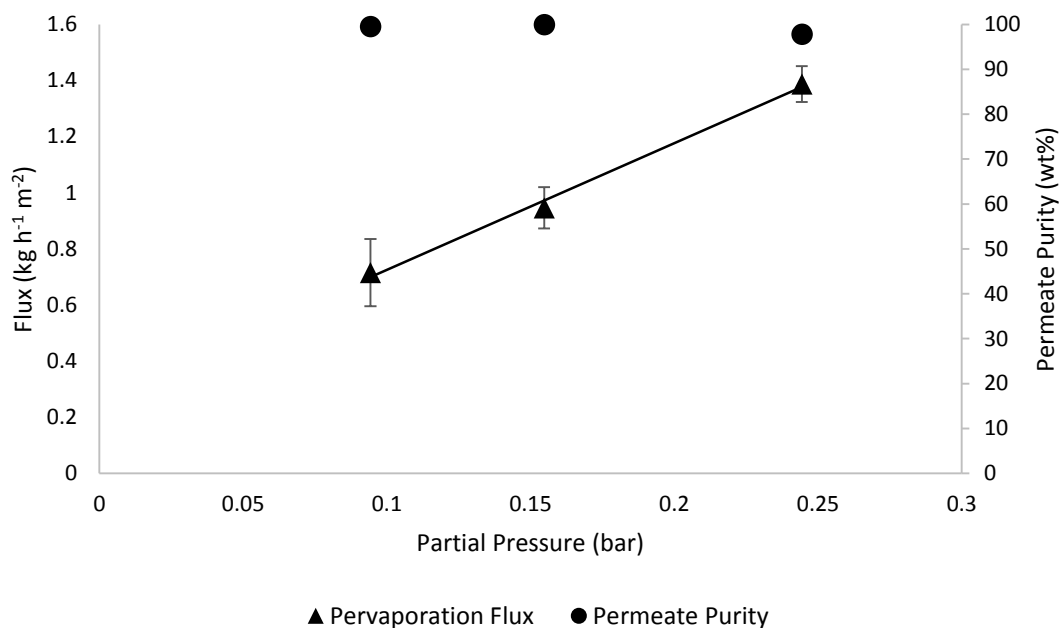
Figure 35-Pervaporation flux of water/IPA (30 / 70wt%) solution at 50, 60, and 70°C, 2.1μm membrane

A binary pair of Water/EtOH was studied in a 50 – 80°C temperature range. As anticipated the permeation flux rose linearly with increase in partial pressure and was in agreement with the solution-diffusion model, Figure 36. The permeation flux was significantly lower when compared to the Water/IPA system. The permeate purity (95.0-95.7 wt%) was also slightly lower than the Water/IPA binary pair. This was attributed to the smaller molecular kinetic diameter of the ethanol molecule leading to an easier intercalation into the G.O. structure and faster permeation rates of the organic species.

A Water/THF solution was investigated in a 50 – 70°C temperature range using a thinner, 1 μm membrane. The permeation flux trend was in agreement with the solution-diffusion model and increased linearly with increase in partial pressure. As expected, the rate of permeation was significantly higher due to the thinner membrane. The permeate purity remained high in the entire temperature envelope at 97.6 – 99.1 wt% water. A perfect compound separation was anticipated and the presence of the THF in the permeate was surprising. The permeation was attributed to the imperfections in the membrane surface.
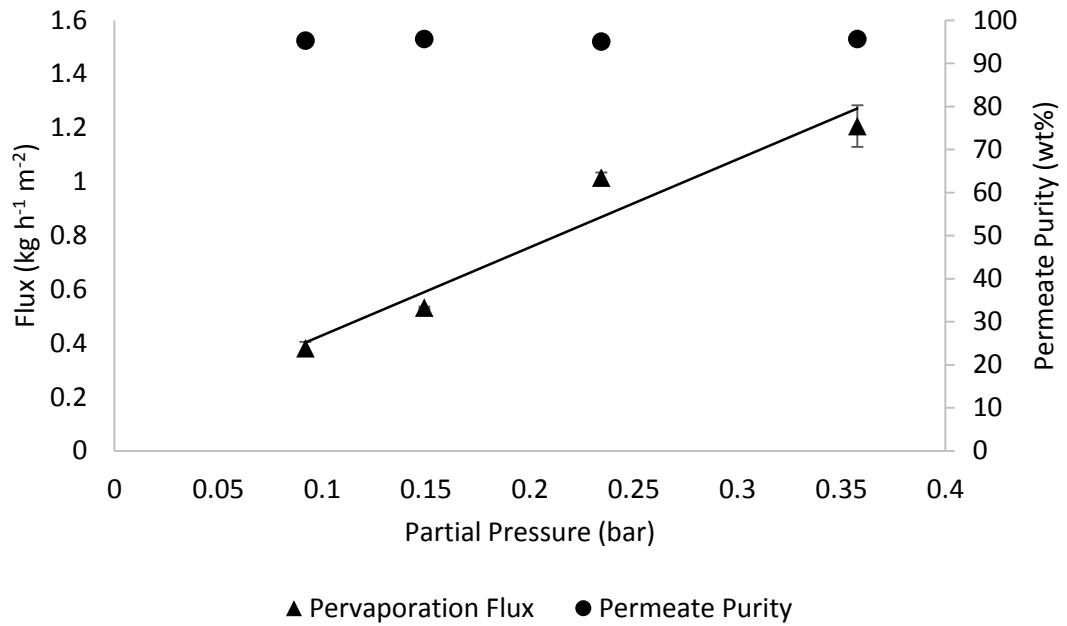
Figure 36-Pervaporation of water/ethanol (30 / 70wt%) solution at 50, 60, 70, 80°C, 2.1 μm membrane
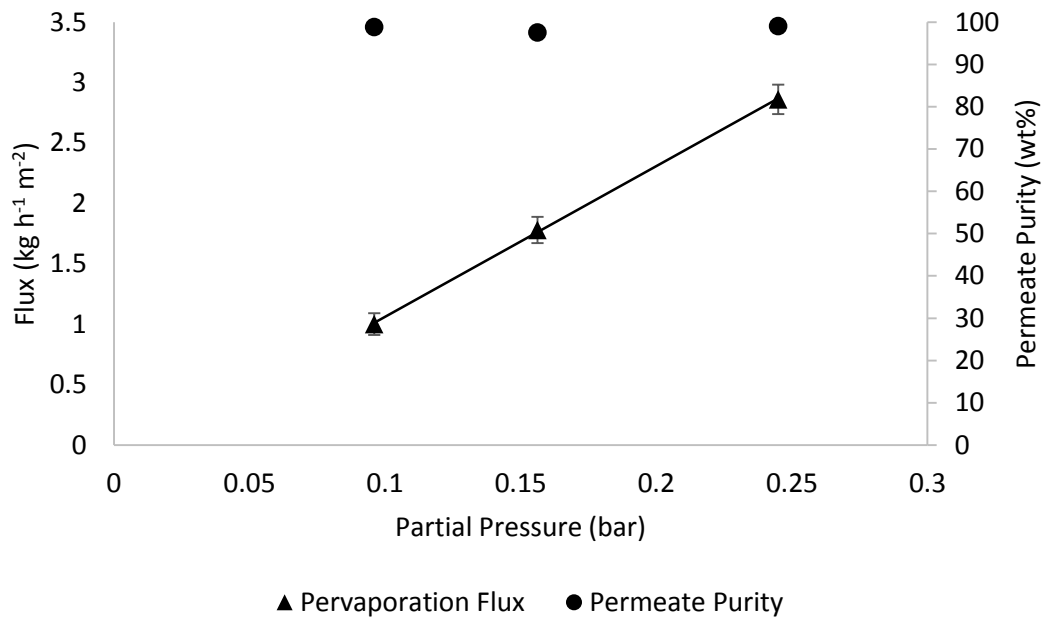
Figure 37-Pervaporation of water/THF (30 / 70wt%) solution at 50, 60, 70°C, 1.0 μm membrane

4.7.2   Membrane thickness

To test the pervaporation flux change with respect to the membrane thickness the pervaporation flux in Equation 72 was divided by the partial pressure of water over the solution to yield equation Equation 73.

$$\frac{J}{P_{w_L}} = D_{w_m} K_s^G \frac{1}{y_m}$$

Equation 73

To test the impact of GO layer thickness, membranes of three different thicknesses were evaluated Figure 38. The pervaporation flux linearly increased with a decrease in the selective membrane layer which was anticipated and is in agreement with well-established membrane research.[2] The pervaporation flux was extremely high and a pressure and thickness normalised permeation coefficient resulted in a value of 12.4 kg µm h^{-1}m^{-2}bar^{-1} ± 24%;. It was estimated that a 1.2 µm membrane at one bar pressure and 30 wt% water in IPA would result in a 10 kg h^{-1}m^{-2} water flux.

The purity of the permeate remained high in the entire region studied and was in a range of 97 – 99 wt%; There was, again, no observable trend for the permeate purity in the studied thickness range.
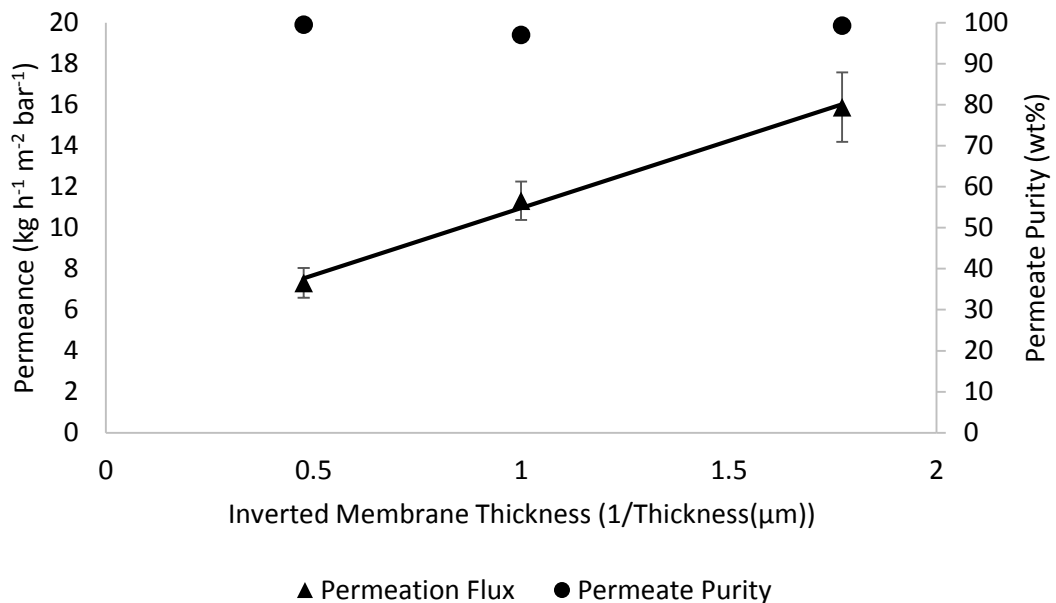
Figure 38-Pervaporation of water/IPA (30 / 70wt%) vs inverted membrane thickness (0.56, 1 and 2.1µm), 50 and 60°C

4.7.3 Water concentration effects

In light of the membrane degradation (showed in the earlier work), demonstrated by pervaporation of 20wt% water in IPA, a lower pervaporation temperature was selected to study long term water concentration influence on the membrane. In this instance 1-100 wt% water in IPA at 50°C was selected as a model solution. The entire study was split into several segments i) 1 wt% experiment, ii) 4-5 wt% experiment, iii) 8-12.5 wt%, iv) 5-30 wt%, and v) 100 wt%. Graphically, this was plotted as a pervaporation flux versus partial water vapour pressure, Figure 39. Interestingly, the pervaporation flux change exhibited a curved trend line. If the solution-diffusion model is applicable to the graphene oxide material the pervaporation flux had to be linear with respect to the change in water vapour partial pressure, Equation 66 Equation 72. The curved change in the rate of permeation suggests a change in the permeation constant value in the solution-diffusion model.
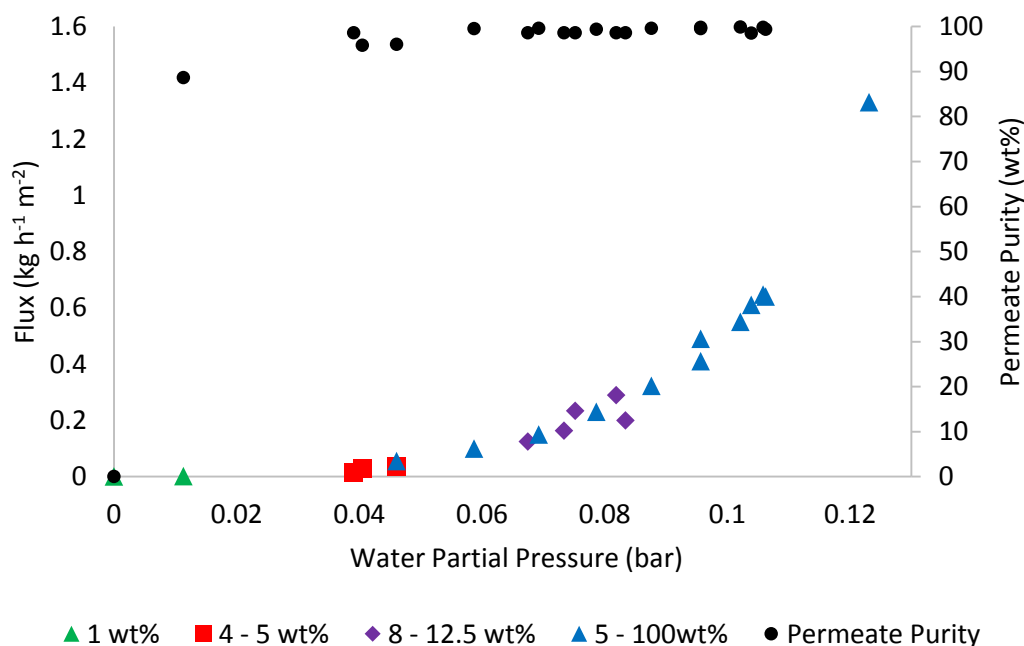
Figure 39-Pervaporation flux with respect to the water concentration, water/IPA (1 – 100wt%), 50°C, 2.1µm membrane

Research at the University of Manchester showed that relative humidity affects the rate of vapour permeation.[1] At 100% relative humidity the rate of permeation matched that of an open apparatus. This was followed by a rapid exponential reduction in the rate of permeation as the relative humidity was decreased.[1] Talyzin et al. has carried out an in depth study of graphene oxide film and powder interlayer spacing change in water/alcohol solutions.[63] The interlayer spacing has dramatically increased from 0.95 nm at 10 vol% water in EtOH to 1.2 nm at 100 vol% water. In their supporting information,

researchers suggested that the level of hydration of graphene oxide is closely related to the water concentration in the solution.[63] If the number of intercalated water layers is directly related to the water concentration this should effect the permeation constant. Thus, it was reasoned that the change in the permeation constant has to be associated with the graphene oxide material interlayer spacing variation with respect to the water content in the process solution

If water concentration has an influence on the permeability coefficient it can be factored in by introducing an extra term in the model, Equation 74.

$$J = k_{m.p}x(P_{W.L} - P_{W.P})$$
<div align="right">Equation 74</div>

Where the additional term, x, is a mole fraction of water in the process solution. The experimental data used in the Figure 39 was reused to graphically represent Equation 74, shown in Equation 47.

Mole fraction corrected solution-diffusion model flux gained a linear trend line with respect to the product of the mole fraction and partial water vapour pressure in the bulk liquid. A linear declining gradient indicates that the permeation constant remains the same in a range of water concentrations and this model is a better representation of the water permeation through the G.O. membranes.

y = 10.715x
R² = 0.9946

● Pervaporation Flux   ▲ Permeate Purity
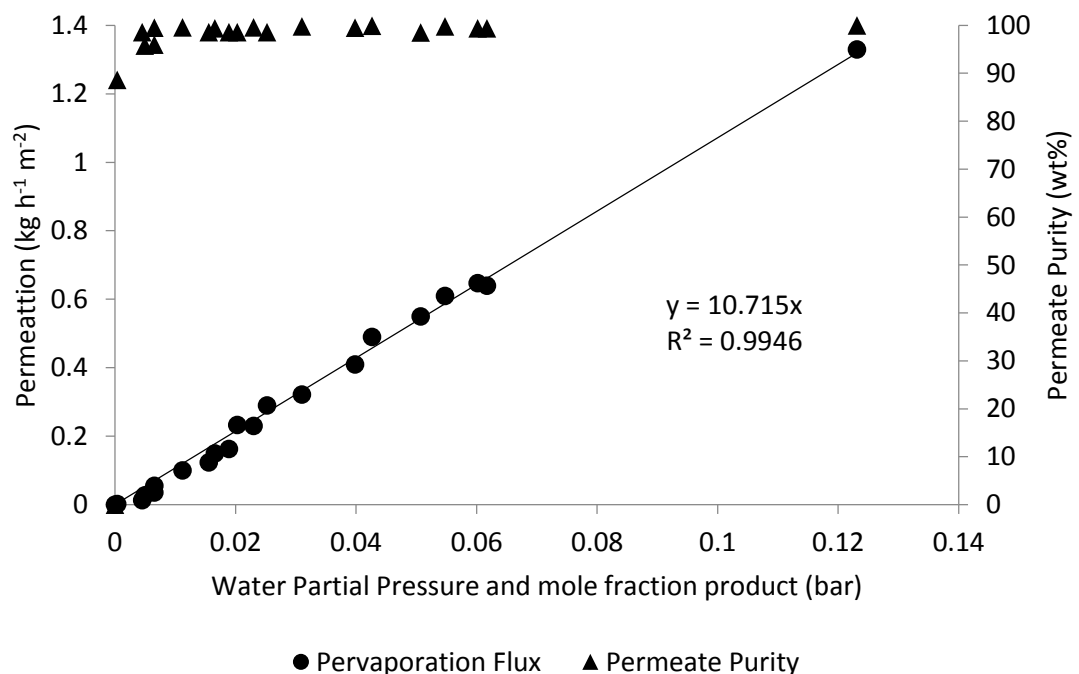
Figure 40-Pervaporation flux vs mole fraction corrected driving force, water/IPA (1 – 100wt%), 50°C, 2.1µm membrane

4.8 Summary

The work in this chapter is concluded by comparing various state-of-the-art polymer, G.O. and commercial membranes, Figure 41. While G.O. membranes in this work showed significantly smaller selectivity coefficient they were very competitive in terms of the membrane thickness and temperature normalised pervaporation flux compared to the bulk of prior G.O. membranes. G.O. membranes in this work also outperformed polymeric and HybSi membranes in terms of pressure and membrane thickness normalised pervaporation flux and provided comparable magnitude separation performance. However, having in mind that polymeric and ceramic membranes had a significantly larger amounts of investment in their R&D, it is not unreasonable to postulate that G.O. membranes could offer significantly better permeation rates and affinity towards water if further material development would take place.
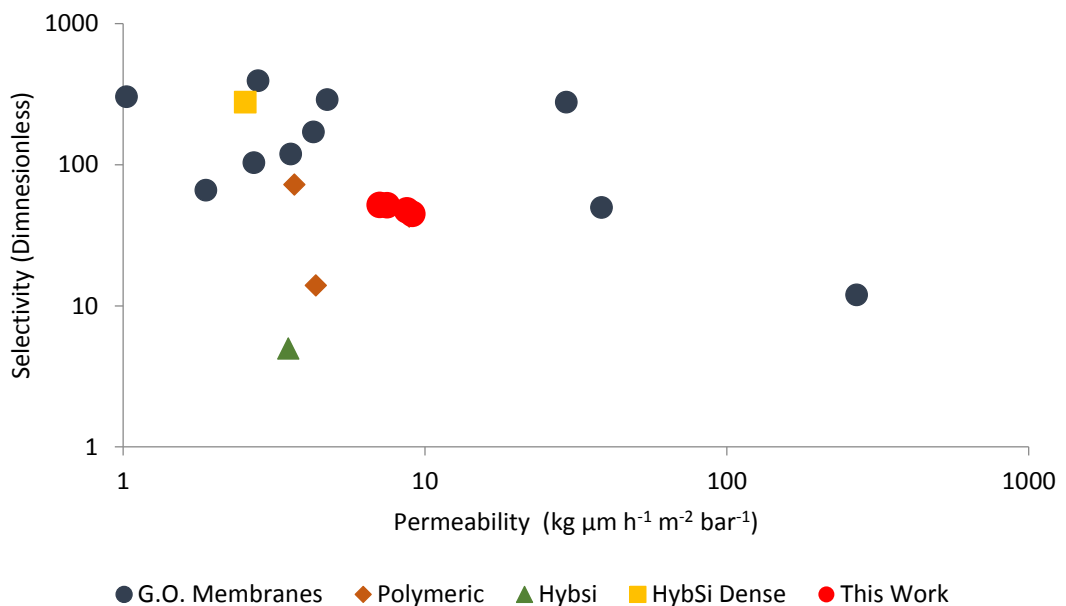
Figure 41-Membrane Comparison

5 Industrial Case Studies

5.1 Organic/Organic Separation

Compound separation using large-scale column chromatography is a well-established and versatile process.[114] The separation can be used to remove impurities from naturally occurring compound mixtures. Final products are clear, odourless high purity compounds used in the pharmaceutical and personal care industry.

This case study focuses on a waste solvent treatment from a chromatographic process where two high added value personal care products are manufactured. The process was composed of three stages: i) apolar wash, ii) polar and apolar mixture wash, and iii) polar and a polar wash. In the first stage a high added value product is produced at a moderate yield on a large scale. The second stage of the process extracts the remaining non-polar compounds and a large portion of polar products. The third step is focused on the polar compounds.

Recently, there has been an interest in increasing profitability of an existing chromatographic separation by improving the following aspects:

1. Process yield
2. Product quality
3. Minimising waste

A potential route to minimising waste would be a solvent recovery. G.O. membranes are very selective water barriers. In this case study there is a need to separate MeOH which has very similar kinetic molecular diameter and has been shown in prior art to selectively permeate through G.O. membranes.[115]

MeOH/n-Hexane mixtures are not fully miscible and undisturbed phase separates. Thus, the solvent mixture was stirred in the pervaporation cell and the stock solution vessel in order to ascertain a homogeneous concentration mixture.

The permeation flux of MeOH and permeate purity are shown in Figure 42. As anticipated, the permeation flux has increased with an increase in the MeOH concentration in the process solution. Despite a clear inclining trend, a linear relationship between the wt% MeOH in the process liquid and permeation flux could not be established. The variance in the collected data was attributed to the biphasic nature of the solution and component sensitivity to the temperature changes. The permeate purity has remained high in the entire study region with only minute amounts (0.8-7 wt%) of n-Hexane passing the membrane barrier.
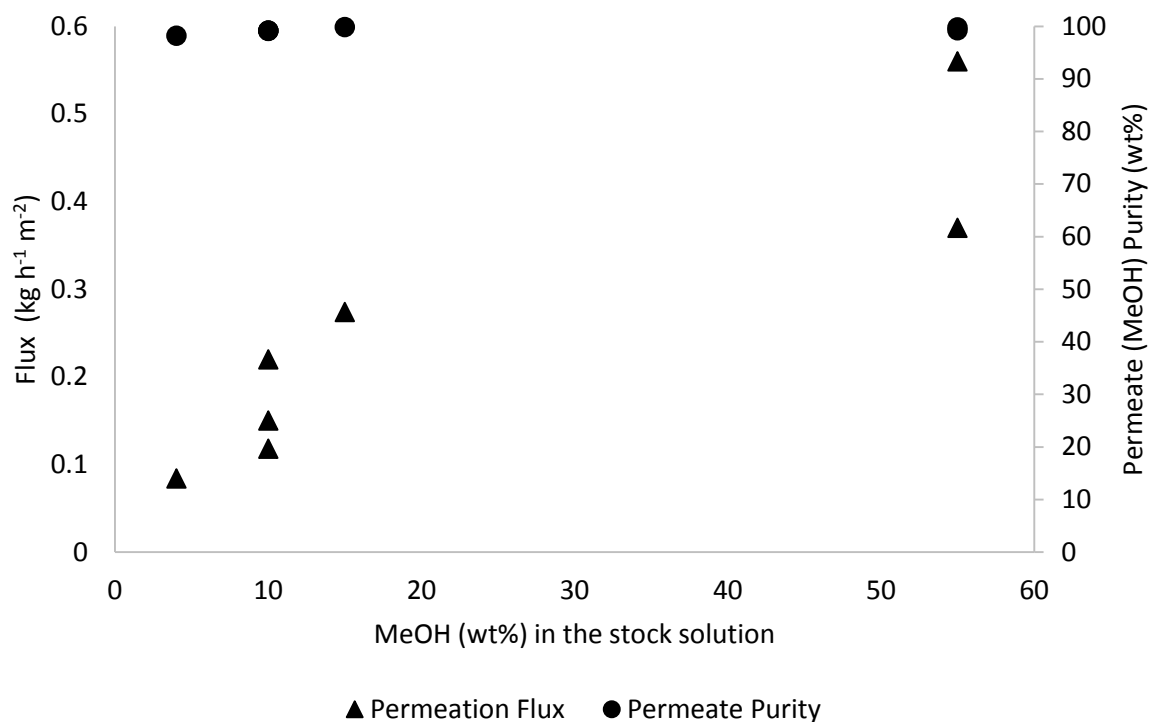
Figure 42-Pervaporation flux of MeOH/n-Hexane (5 – 55wt%), 60°C, 2.1µm membrane

Permeation flux at 10 wt% MeOH and 60-80°C was studied, Table 23. The rate of MeOH pervaporation varied approximately ±17% at 60 and 70°C. The variation in the rate of permeation was again attributed to the temperature fluctuations and the biphasic nature of the solution. The permeate purity remained high in the entire temperature range studied. A decline in the quality of the permeate was observed as the temperature was increased. The highest purity (99.2 ±0.05 wt%) was found at the lowest temperature (Entry 1) and the lowest permeate purity (93 wt%) was found at the highest temperature (Entry 3).

Table 23-MeOH pervaporation flux and permeate purity and different temperatures

Entry	MeOH (wt%)	Temperature (°C)	Permeation flux (kg h^{-1} m^{-2})	Permeate purity (wt%)
1	10	60	0.22 (±0.12)	99.2 (±0.05)
2	10	70	0.25 (±0.17)	95.7 (±2.4)
3	10	80	0.15 (N/A)	93 (N/A)

G.O. coated on a hydrophilic PVDF layer has demonstrated a capability to selectively remove MeOH from n-Hexane and produce high permeate purity. This creates an opportunity to treat the waste solvent stream after the second chromatographic separation step and increase the process profitability.

5.2 Esterification

Esterification of carboxylic acids with alcohols is a common example of an equilibrium limited reaction where water is produced as one of the products, Scheme 2. The final yield of such a system is determined by the relative speeds of the forward and reverse reactions. To shift the equilibrium towards the product formation two strategies can be employed: i) increase the speed of the forward reaction by adding excess of a cheaper reagent, or ii) reduce the speed of the reverse reaction by continuously removing one of the reaction products. For low boiling point compounds typically both of the strategies are used concurrently. An excess of alcohol is added to favour the forward reaction, and remove water (a reaction product) from the process solution by distillation, thus reducing the speed of the reverse reaction. However, this leads to an excessive amount of alcohol used and an energy intensive waste stream treatment.[116] Alternatively, a non-reacting immiscible species can be added to the reaction mixture to act as a carrier compound such as toluene or cyclohexane. This would induce a natural, energy free phase-splitting in the distillate product and in turn would remove water very efficiently. However, in the production of a fatty acid esters, which are common products in personal care focused chemical industry, these compounds cannot be used due to their toxicity.[116]
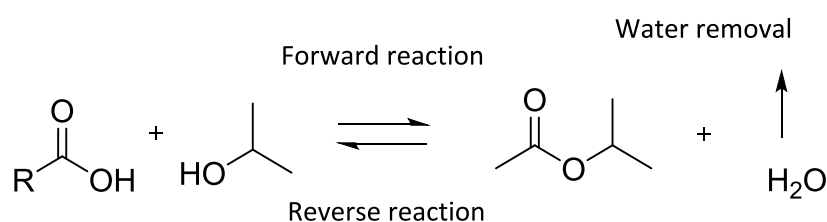
Scheme 2-Generic esterification process

Multiple pervaporation assisted esterification studies have successfully demonstrated *in-situ* water removal and an increase in the final product yield. Korkmaz *et.al.* have used commercially available hydrophilic PERVAP 1201 and Nafion 117 membranes to remove water from acetic acid and isobutanol esterification reactions. Both membranes, PERVAP 1201 and Nafion 117, have shown higher final product yields, 78% and 90%, respectively, at the end of the reaction compared to a simple batch operation which had an equilibrium conversion set at 57%.[117]

Despite the numerous successful pervaporation studies, the use of the membrane technology where reaction and product removal is combined is limited due to several drawbacks. A major polymeric membrane shortcoming is their resistance to organic solvents at elevated temperatures.[29] Inorganic pervaporation membranes cannot tolerate acidic conditions, for example zeolite membranes immediately denature even at mild acidic conditions.[45] To circumvent the material degradation by esterification mixture inorganic membranes can be used in a vapour permeation mode.[116]

To the best of our knowledge, G.O. membranes have not been used before for a selective water removal from an esterification reaction mixture. It was anticipated that the G.O. membrane will be able to tolerate acidic conditions without a loss in performance. The only pervaporation system limitation was imposed by a hydrophilic PVDF polymeric support, which has limited the range process temperature.

It is important to note that due to the experimental setup, shown in a simplistic view in Figure 43, the rate of conversion is not comparable with a simple batch operation. The stock solution was recirculated between the stock solution vessel where it was maintained at a room temperature, and a pervaporation cell, where the reaction was taking place.
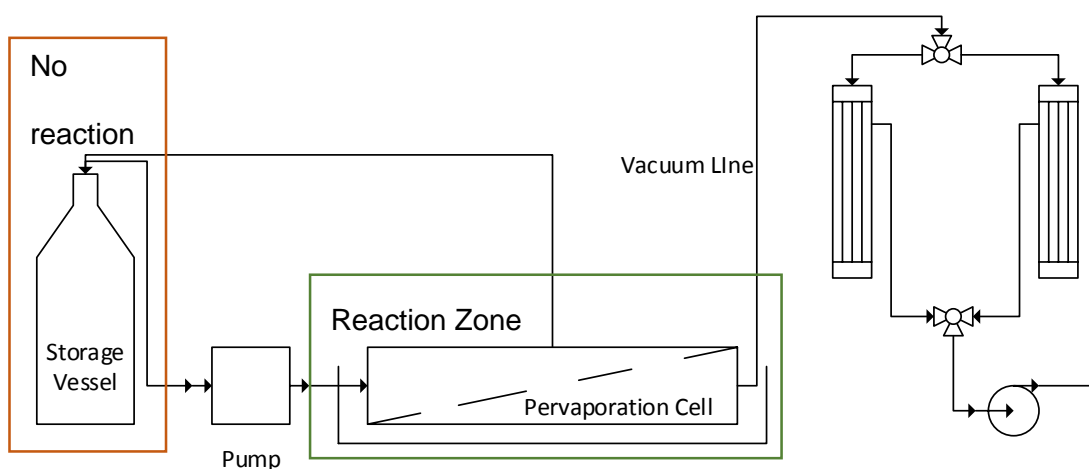
Figure 43-Pervaporation assisted esterification reaction setup

The esterification reaction was conducted using a pervaporation setup with and without a G.O. membrane. In the study without the selective water removal the G.O. membrane was replaced by an impermeable PTFE disk.

The effects of a G.O. membrane on an esterification conversion are shown in Figure 44. An esterification reaction at 100°C without a selective water removal has reached 58% conversion after 16 hours. The selective water removal from the reaction mixture has increased the conversion to 77% within the same time frame. The experiment was then

repeated without replacing the membrane in the pervaporation cell. Interestingly, the conversion after 16 hours was only 69%. In both cases, the first run and the repeat, water removal from the reaction mixture has increased the conversion. A cumulative permeation flux and the permeate purity time plot are shown in Figure 45. The permeate purity remained high at 99wt% water value throughout the first 21 hours of experimentation. This shows that the G.O. membrane was capable of separating water from the esterification reaction with high selectivity. The value dropped to 85 wt% water in the permeate in the last two samples. This is most likely a result of a perished rubber seal between the membrane and the permeation cell, which resulted in a minute leak and could be avoided by selecting a seal which is more compatible with the reaction products.

The permeate flux could not be maintained at a stable value, Figure 45. Initially, a high 0.65 kg h^{-1} m^{-2} water flux was measured. This was followed by a large decrease to 0.18 kg h^{-1} m^{-2} permeation rate, which has linearly declined for the remainder of the experimental time to 0.043 kg h^{-1} m^{-2}.

Pervaporation flux change with respect to the theoretical water wt% in the process solution is shown in Figure 46. There was no obvious correlation between pervaporation flux and water concentration in the process solution. The highest permeation rate was observed at 1.6wt% water in the reaction mixture which was the lowest water wt% in the entire study. An increase in the water concentration in the process solution did not increase the permeation rate, leading to a conclusion that the permeation flux was strongly affected by other factors such as membrane degradation at elevated temperatures.
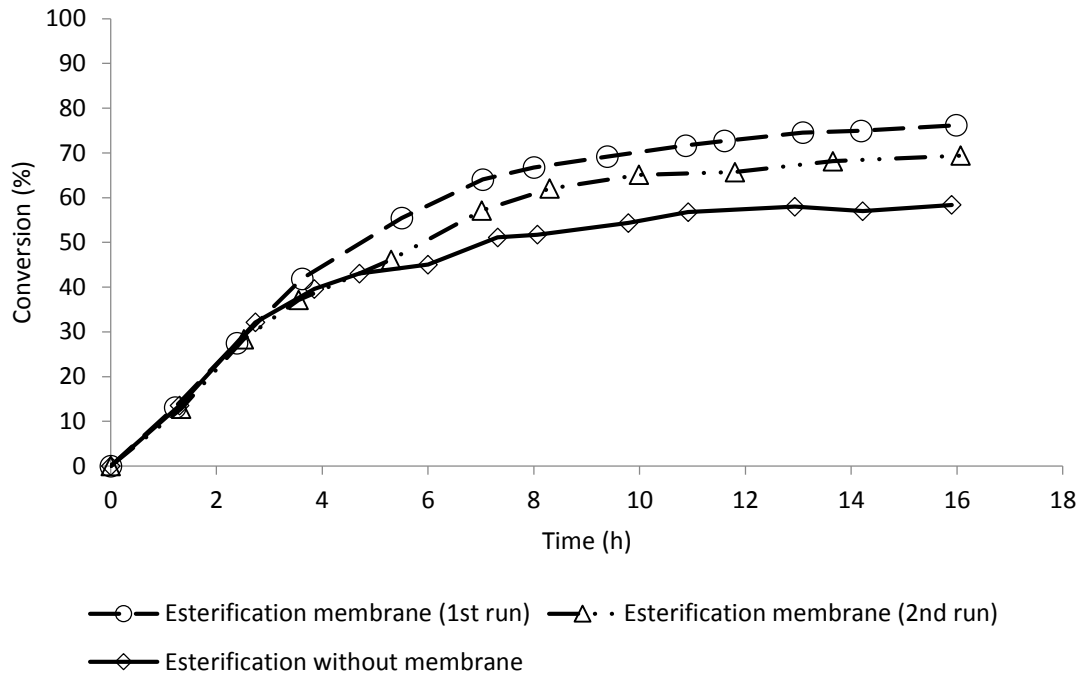
Figure 44-Effects of selective water removal on esterification reaction conversion, 100°C, 2.1µm membrane
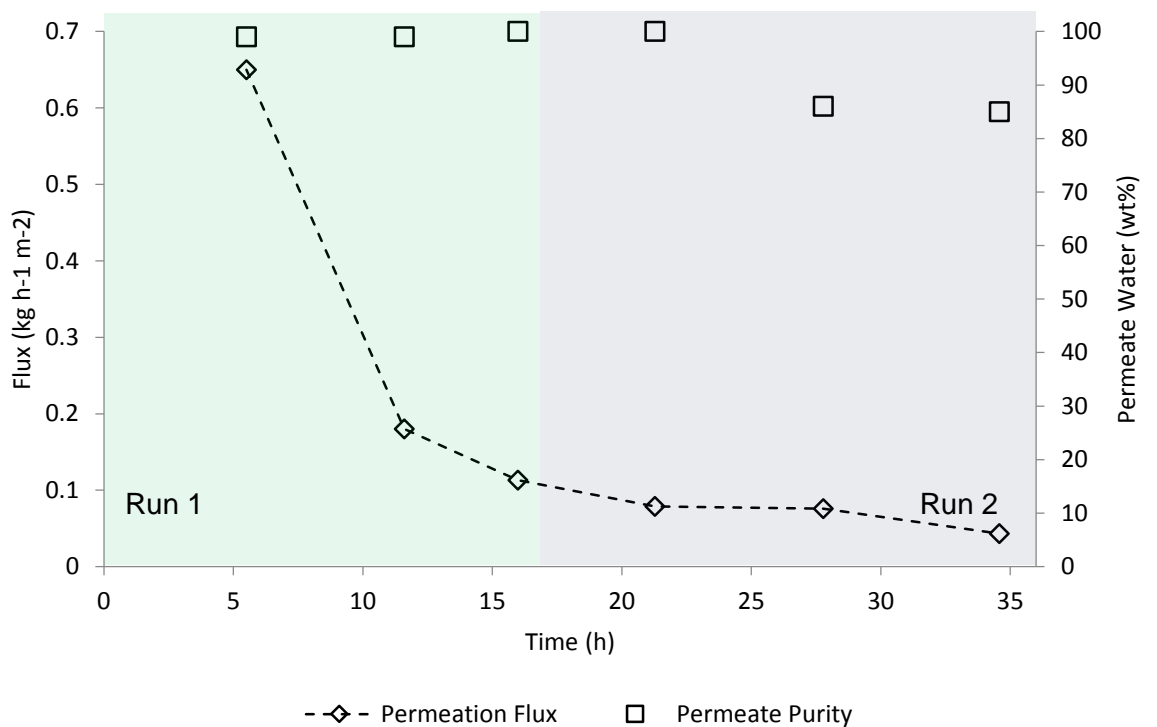
Figure 45-Pervaporation flux and permeate purity vs time, 100°C, 2.1µm membrane
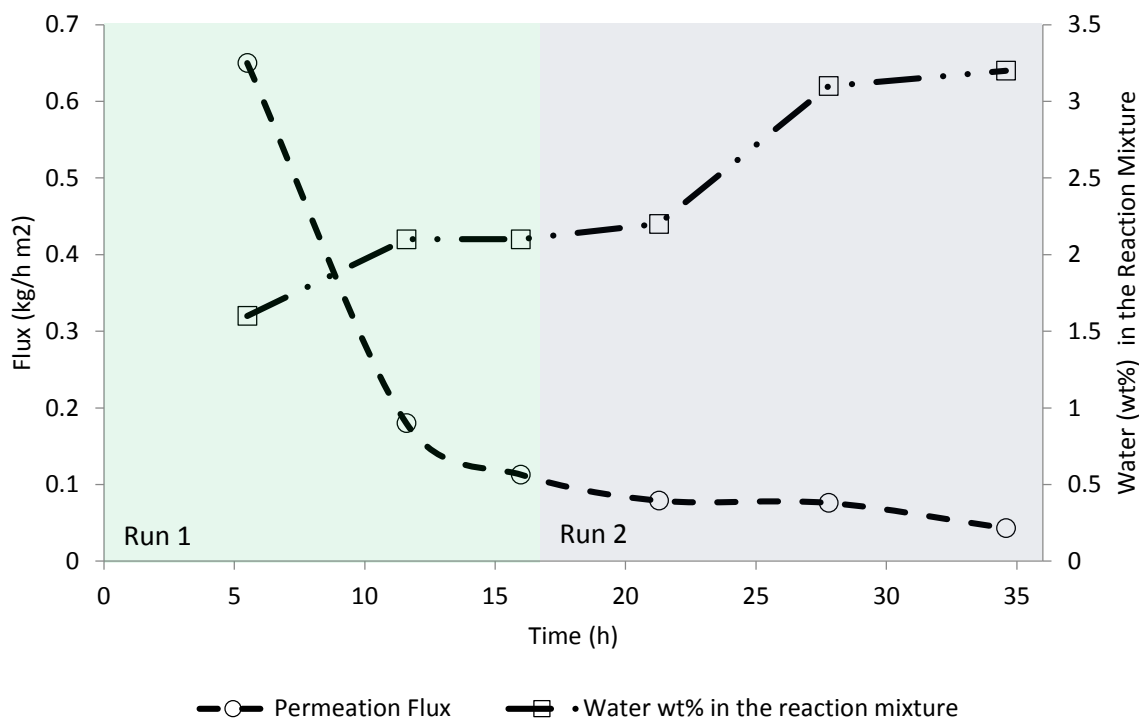
Figure 46-Pervaporation flux change vs water wt% in the reaction mixture, 100°C, 2.1µm membrane

The G.O. membrane used in the esterification reaction was characterised using SEM and EDX analysis tools, Table 24 and Figure 47 respectively. A visual image of used membrane did not appear significantly different than an image of a fresh G.O. membrane. This suggests that the drop in the permeation flux is not related to any physical changes of the membrane surface. An elemental analysis indicated that the membrane selective surface was composed of carbon and oxygen (79.63 wt% carbon / 17.64 wt% oxygen) almost in the same ratio as a fresh membrane (79 wt% carbon / 20 wt% Oxygen and 1 wt% impurities). This suggests that the bulk of the material was able to tolerate the esterification reaction components at 100°C for over 35 hours.

Table 24-Visual G.O. membrane characterisation

Experiment	Conditions and comments	SEM image
Fatty carboxylic acid and IPA esterification at 100°C	Used membrane, 2 µm zoom.	
N/A	Fresh membrane, 1 µm zoom.	
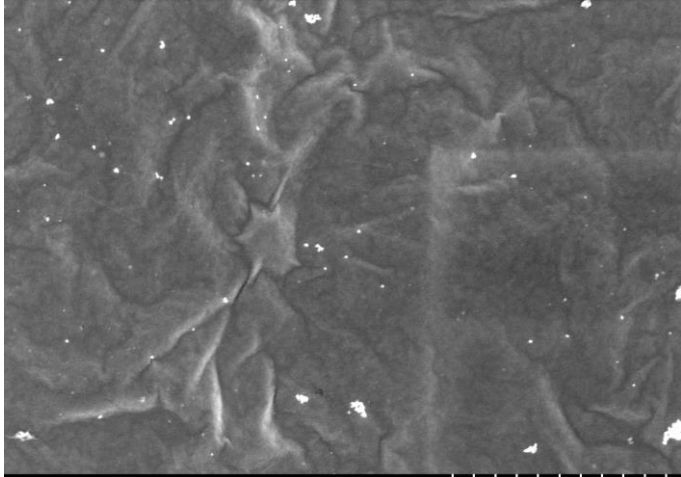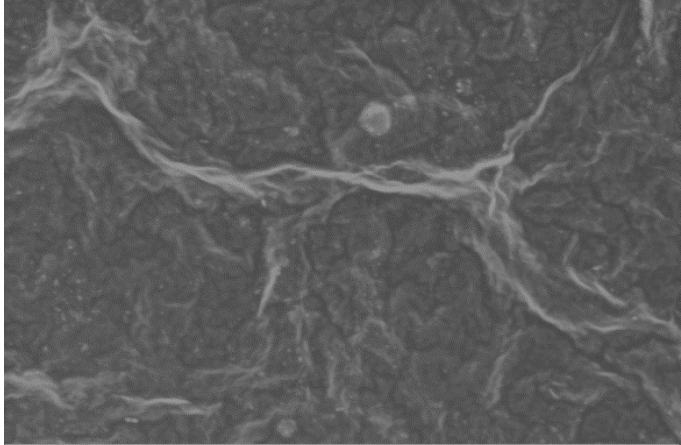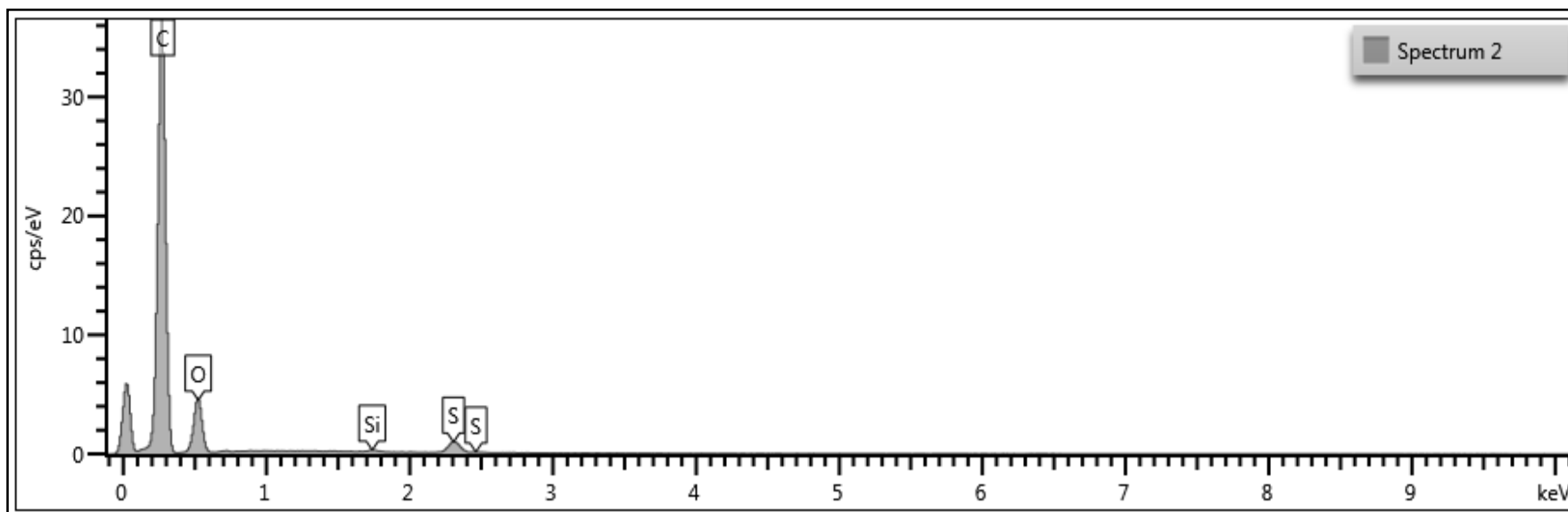
Elemental composition table

Element	Wt%	Wt% Sigma
C	79.63	0.17
O	17.64	0.16
Si	0.27	0.03
S	2.47	0.06
Total:	100.00	
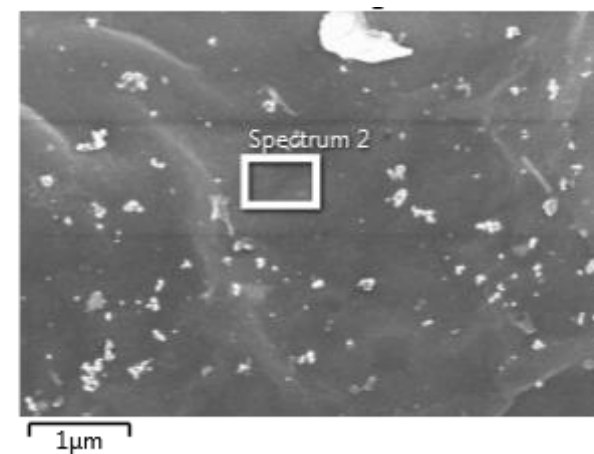
Figure 47-Energy dispersive X-ray spectroscopy characterisation of the G.O. membrane exposed to an esterification reaction

The change in the G.O. membrane surface chemistry was investigated using FT-IR, Figure 48. A large double headed peak appeared at 2919 and 2854 cm^{-1}, which was attributed to an alkane (-CH$_3$ and -CH$_2$-) symmetric and antisymmetric stretching. The peak may originate from either surface bonded carboxylic acid or IPA. Interestingly, similar surface chemistry change was observed in the water/IPA dewatering chapter "Organic Solvent Dehydration". The fingerprint region had a significantly different landscape than an unused membrane or G.O. used in the IPA dewatering study. The emergence of new peaks in the fingerprint region is likely to be a result of the thermal decomposition of the G.O. at elevated temperatures[103] and permanently bonded esterification reaction compounds. To date it is not known whether it is possible to avoid the surface chemical change and retain the permeate flux and the membrane selectivity.
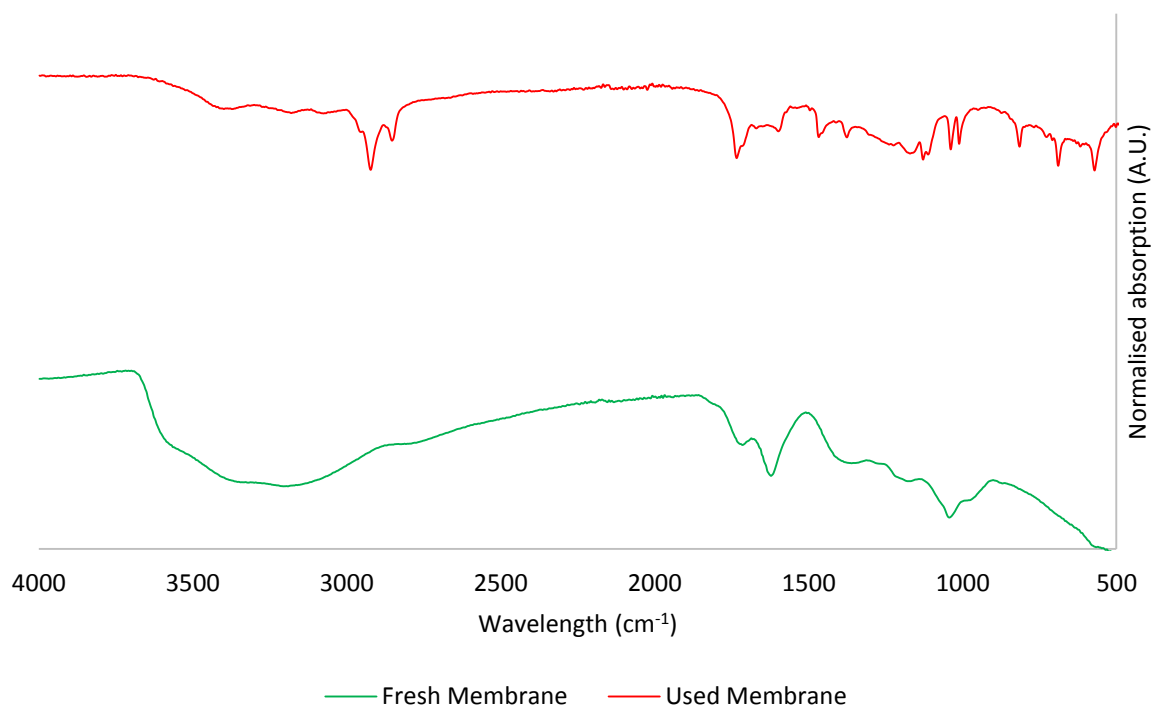
Figure 48-FT-IR spectrum of used (esterification reaction, 100°C, 2.1µm membrane) and fresh G.O. membrane
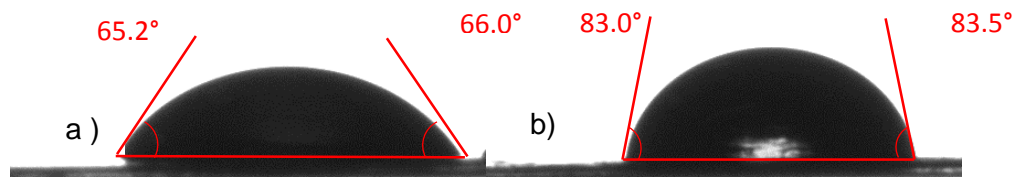
Figure 49 - Water contact angle on the a) fresh G.O. membrane, and b) used G.O. membrane in an esterification reaction

To complement the FT-IR study, water contact angle measurements were made, Figure 49. A water drop contact angles has significantly increased from approximately 66° (fresh G.O. membrane) to 83° (used G.O. membrane). The increased contact angle shows a decrease in the material hydrophilicity which is known to negatively impact the water permeation flux and membrane selectivity.[118] The issue could be addressed by modifying the material surface chemistry and attaching more stable functional groups.

5.3 Peptides

A membrane separation process is an attractive water removal technique, not only for challenging azeotropic mixtures, but also for highly aqueous protein solutions. Large scale dewatering is typically conducted *via* distillation. However, large molecular species such as peptides or proteins can degrade at high temperatures. This severely limits the rate of water removal in a distillation process and makes equipment underutilised. A membrane process can remove large quantities of water under mild conditions and a relatively small floor footprint due to its compact module design.[85]

An incorporation of a G.O. sheets into a polymeric membrane matrix has previously shown a good water separation rate and a decreased membrane surface fouling[119], which is especially prominent in a peptide separation processes.[120] In this case study, 2.1 μm G.O. membranes were used in a water removal operation from highly aqueous peptide solutions.

The current peptide dewatering process uses vacuum distillation to evaporate approximately 10,000 kg water at 80°C. One operation takes 6-10 h, which translates to the following rate of water removal 1000-1666 kg/h. The variation in the rate of water removal is attributed to the following two factors: i) initial solids content, and ii) a variation in the steam temperature.

To improve industrial peptide dewatering process several key factors were identified:
  i)   Processing time reduction
  ii)   Lower processing temperature
  iii) Improved quality of the product

Initial DI (deionised) water pervaporation tests at a 70°C and 90°C resulted in a 5.43 and 9.8 kg h^{-1} m^{-2} flux respectively. Pervaporation flux at 80°C was estimated using prior data to be approximately 8 kg h^{-1} m^2. This approximation allows for a facile required membrane surface area calculation to remove 10000 kg in 6-10 h, Table 25.

Table 25-Estimates of membrane areas required to replace current evaporator process

Operation Time (h)	Area (m^2) at 70°C	Area (m^2) at 80°C
6	307	208
10	184	125

5.3.1 Peptide 1 Hydrolysate

Pervaporation of an aqueous Peptide 1 hydrolysate solution was conducted at 80°C and 2-8wt% solids in water content over a course of several days, resulting in a total experiment time of ≈34 h. The purpose of this study was to investigate the pervaporation

flux and G.O. membrane stability at elevated temperatures and different solids content at prolonged operation times. The change of water flux was plotted against time of operation and is shown in Figure 50. The dotted straight line at the top of the Figure 50 shows the maximum water flux at 80°C.

The initial rate of water transport was 4.29 kg h^{-1} m^{-2}, which is significantly lower than DI water rate of permeation (≈8.0 kg h^{-1} m^{-2}). The exact reason for such a drop in pervaporation flux is currently unknown, however a likely explanation is a peptide-G.O. adsorption. Previous research shows that some protein mixtures can almost immediately foul membrane surface and impact on water transport through the selective membrane layer.[121] In this series of studies the pre-equilibrium stage was at least 1 h, which would be a sufficient amount of time for a rapid membrane fouling to occur. As the pervaporation operation progressed the drop in the rate of permeation continued for the first 5 h exhibiting an exponential trend. The pervaporation flux gained a steady value (≈2.6 kg h^{-1} m^{-2}) during 5 – 10 h of operation. From there onwards a linear drop in the rate of permeation was observed resulting in a practically non-existent water flux after a 34 h of operation. Interestingly, no significant changes in the pervaporation flux were observed with a change in the solids wt%. It was anticipated to observe an increase in the rate of fouling with respect to an increase in the amount of solids in the process solution.

The predicted flux line was modelled as two separate equations i) exponential (initial), and ii) linear drop. A small abnormality in the predicted flux between 11-12 h is present. This is a transition zone between the exponential drop to linear flux drop stages.
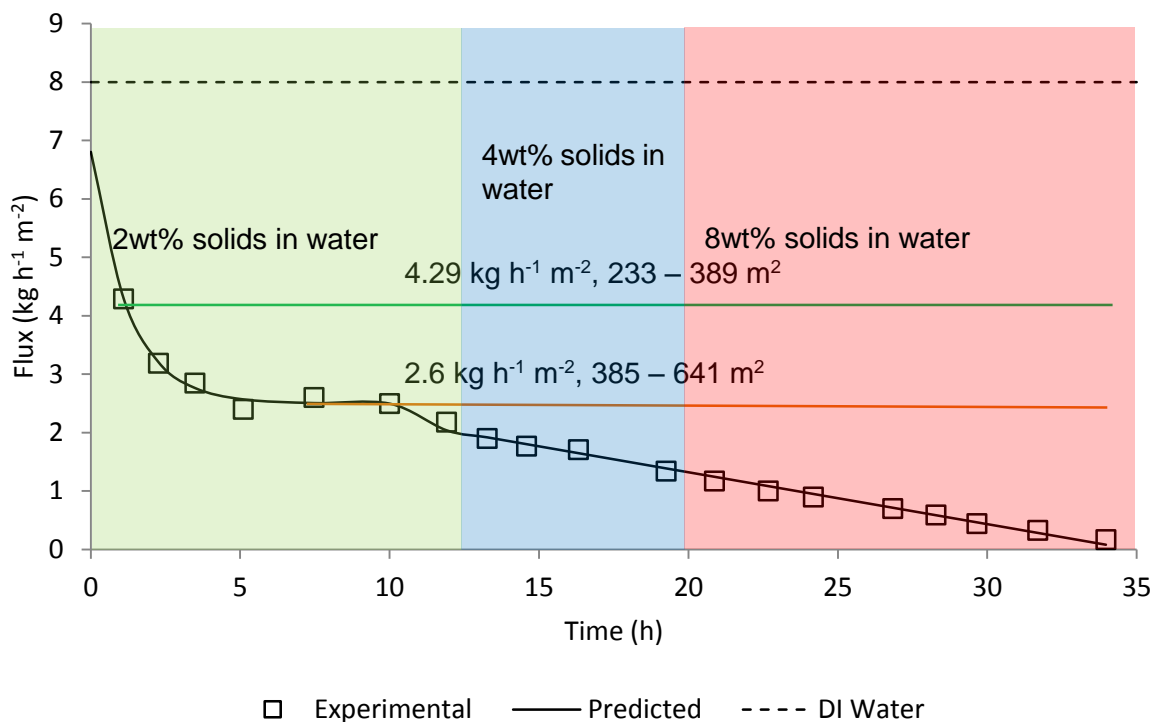
Figure 50-Pervaporation of aqueous Peptide 1 Hydrolysate (2 – 8wt% solids) at 80°C, 2.1 μm membrane

For an extremely dilute system containing only 2wt% solids it was anticipated to achieve DI water rate of permeation. It is important to note that the model fitted flux at 0 h does not match pure water pervaporation rate. This may be a result of i) inaccurate interpolation of DI water data, or ii) immediate interaction between peptides and G.O. surface. It is also important to note that the initial pervaporation data is lost due to pre-equilibration stage, which was ≥ 1 h.

Two new sets of required surface areas were estimated at initial flux and a semi steady-state flux as 233 – 389 m^2 and 385 – 641 m^2 respectively.

5.3.2   Peptide 2 Hydrolysate

The Peptide 2 peptide solution dewatering was conducted at 80°C over a period of 26 h. The rate of water permeation was plotted against time of operation and is shown in Figure 51. The dotted straight line (8 kg h^{-1} m^{-2}) shows the maximum rate of permeation at 80°C interpolated from previous DI water permeation data. The initial rate of permeation was found to be 5.2 kg h^{-1} m^{-2}. At a similar time of operation Peptide 1 peptide had almost 1 kg h^{-1} m^{-2} lower flux than Peptide 2 peptide solution. It is not known whether this is a result of different pH or structure/molecular weight of the peptides present in the solution. The semi steady-state rate of permeation at 3.6 kg h^{-1} m^{-2} was reached after 2 hours of

operation. A linear flux decline was observed after 10h of operation and was similar to the Peptide 1 peptide dewatering process.

The entire pervaporation process was modelled using a two-part equation i) exponential drop, and ii) linear drop. The shape of the curve was similar to the one of the Peptide 1 peptide dewatering process. However, the gradients were different indicating different rates of the membrane "deactivation".
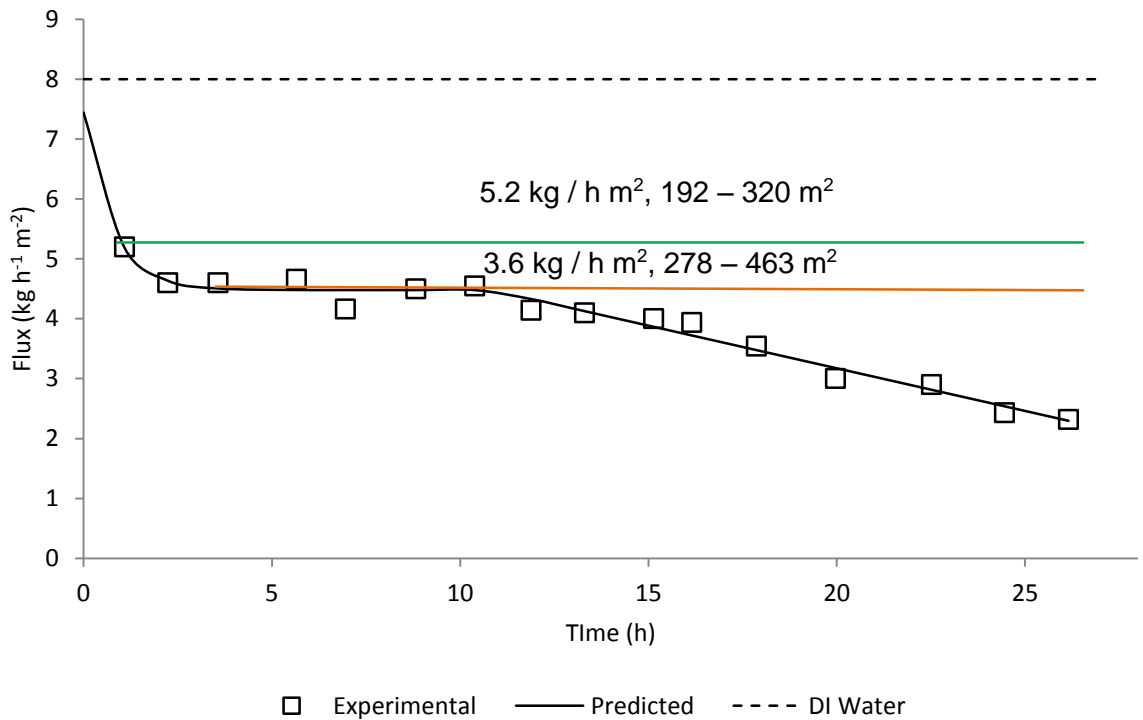
Figure 51-Pervaporation of aqueous Peptide 2 Hydrolysate (5wt% solids) at 80°C, 2.1 μm membrane

5.3.3 Peptide 3 Hydrolysate

Pervaporation experiments were conducted using typical pervaporation procedures as described previously. The pervaporation flux against time of operation was plotted and is shown in Figure 52. The difference in the initial pervaporation flux and the maximum rate of water permeation (DI Water) was considerably larger for aqueous Peptide 3 than any other tested peptide. This may be an indication of significantly stronger and faster membrane fouling. In order to test this hypothesis further studies are required. After initial exponential permeation flux drop (6 h) a constant flux was attained for ≈ 13 h. The period of steady state permeation was significantly longer when compared to the Peptide 1 hydrolysate (≈5 h), and Peptide 2 hydrolysate (≈7 h). It is important to note that pervaporation of the aqueous Peptide 3 solution was conducted at 70°C, whilst Peptide

1 and Peptide 2 hydrolysates were dewatered at 80°C. It is known that the process temperature affects the membrane fouling rate.[121]
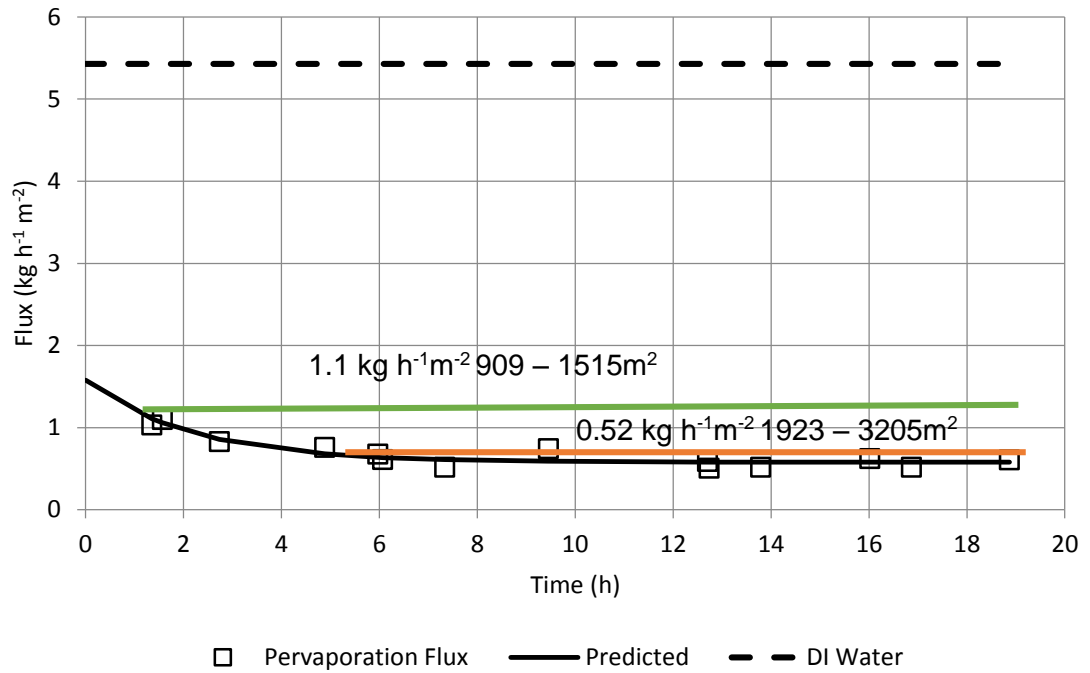
Figure 52-Pervaporation of aqueous Peptide 3 (2wt% solids) solution at 70°C, 2.1 µm membrane

Membranes from the i) Peptide 1, ii) Peptide 2 and iii) Peptide 3 dewatering experiments were analysed using SEM and EDX. To draw an objective comparison between used and fresh membrane surface morphologies an unused membrane image is shown in Table 26. The unused membrane SEM image had a typical surface structure of a G.O. membrane and was a match to the previous research data.[109]

Table 26-Unused G.O. membrane SEM images

Experiment	Conditions and comments	SEM image
N/A	Fresh membrane, 10 µm zoom.	
N/A	Fresh membrane, 1 µm zoom.	
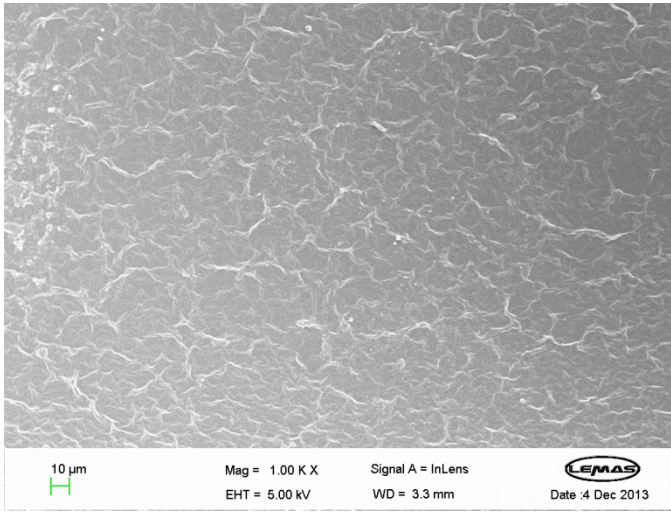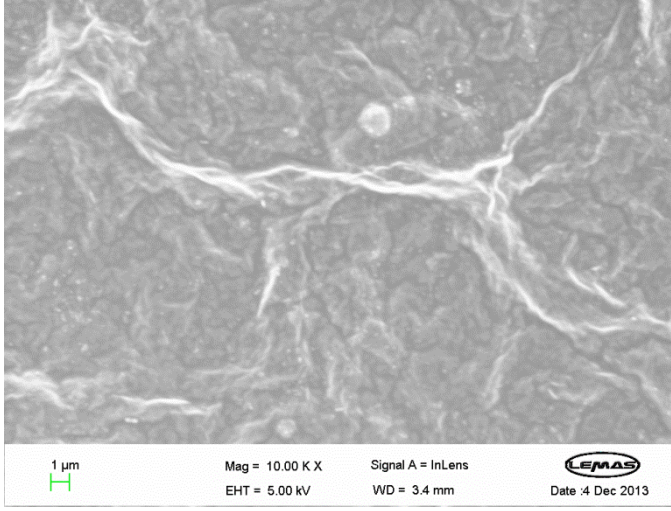
SEM images of the membranes used in the peptide dewatering processes and are shown in Figure 53. All three membranes exhibited different surface morphologies compared to an unused membrane shown in Table 26. The characteristic coarse structure G.O. surface has completely disappeared. Surfaces of the membranes used in dewatering Peptide 1 and Peptide 3 peptides were relatively smooth at a 100 μm scale. The membrane used in the Peptide 2 dewatering process did not share the same surface morphology at a 100 μm scale.

Upon a closer investigation,2 μm zoom, membrane exposed to the Peptide 1 peptide still had a relatively smooth surface and was clearly fouled with the peptide. Membranes exposed to Peptide 3 and Peptide 2 peptides at 2 μm scale had similar surface appearance. The highlighted regions were attributed to a peptide presence at the periphery of the G.O. sheets, which could result from a physisorption or chemisorption process between the G.O. sheet and a peptide functional groups. Interestingly, in the image of the membrane exposed to the Peptide 2 peptide a subsurface of the G.O. membrane can be seen. This would imply that the peptide has bonded to several layers of the G.O. membrane. Physically hindered access between the membrane sheets would inhibit water intercalation into the membrane matrix and negatively impact on the rate of water permeation.

EDX spectroscopy was performed on all of the membranes. The analysis showed a presence of various elements on the surface of the membranes confirming the presence of the peptides. Initially, it was thought that the graphene oxide was chemically altered at elevated temperatures, which has been observed to occur in an alkaline and highly acidic media,[115, 122] and could lead to a drop in a pervaporation flux. In case of the chemical reduction a high increase in the carbon/oxygen ratio was anticipated from an initial 4/1 to 12/1.[115] All of the membranes have retained high oxygen content ranging from C/O 3.42, Figure 56, to 4.58, Figure 54. A high amount, 7.67 wt%, of chloride was found on the surface of a membrane exposed to the Peptide 3 peptide. A minute amounts of chloride (0.22) was also found on the membrane surface used in the Peptide 2 peptide dewatering process. Previous research has highlighted that chloride can permanently bond to the surface *via* S_N2 reaction mechanism.[115] Due to peak overlap it was not possible to tabulate accurate amounts of nitrogen present on the membrane surface. Only a small area scan, Figure 56, showed a significant amount of nitrogen, 9.11 wt%, present on the surface; a key element in all of the peptides.

Figure 53-SEM images of membranes used in i) Peptide 1 hydrolysate, ii) Peptide 3, and iii) Peptide 2 peptide dewatering processes
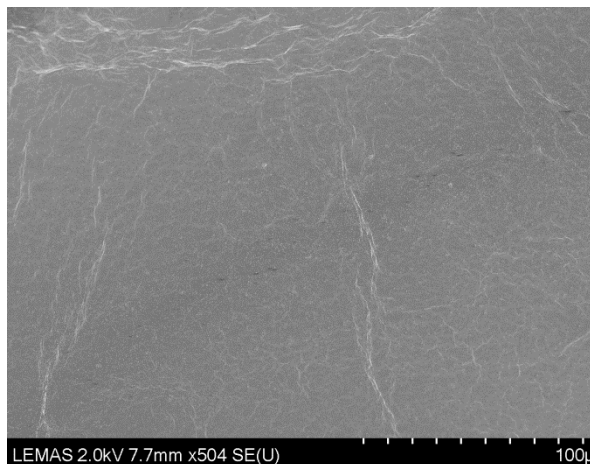
Peptide 1 (700 Da), pH = 4	Peptide 3 (1200 Da), pH =5.5	Peptide 2 (2000 Da), pH = 9.9
100 µm zoom	100 µm zoom	100 µm zoom
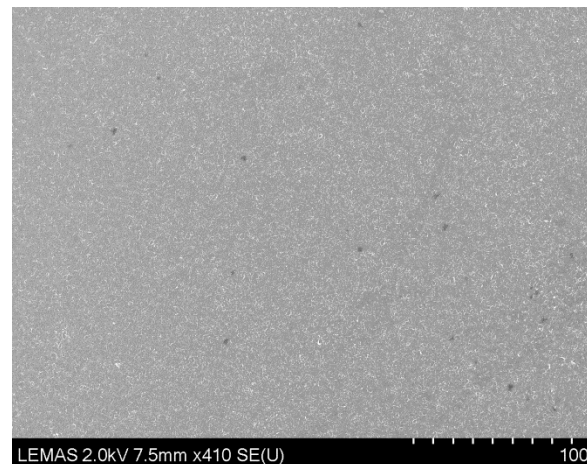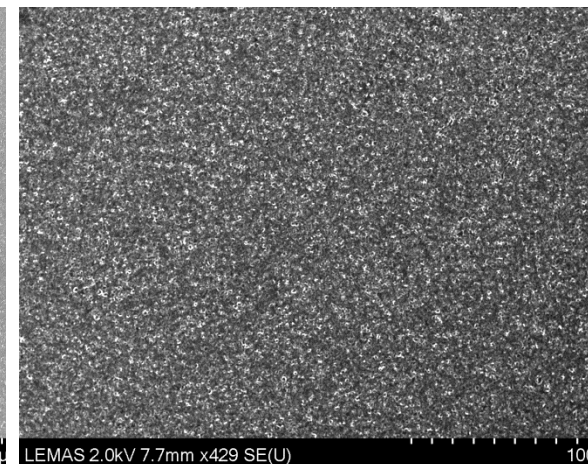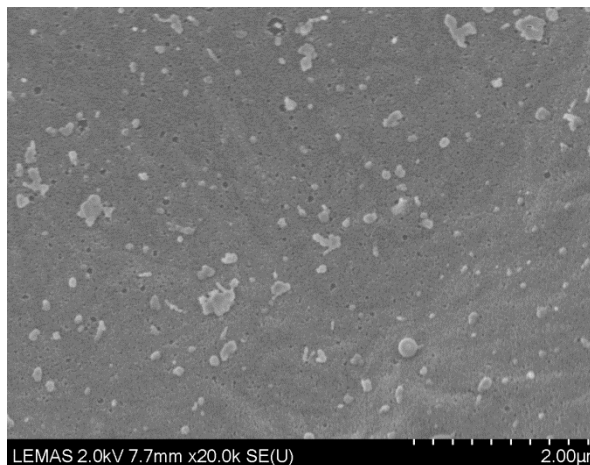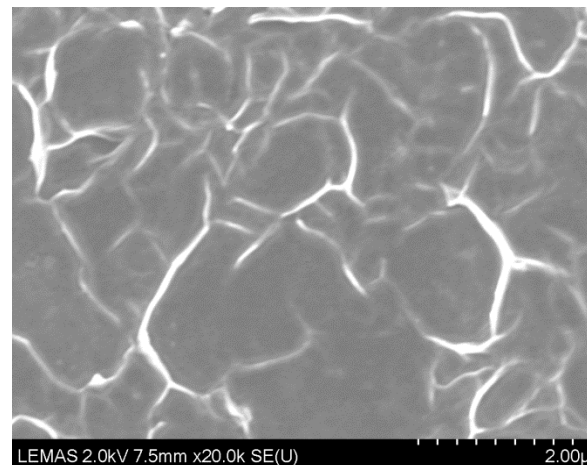
2 µm zoom	2 µm zoom	2 µm zoom
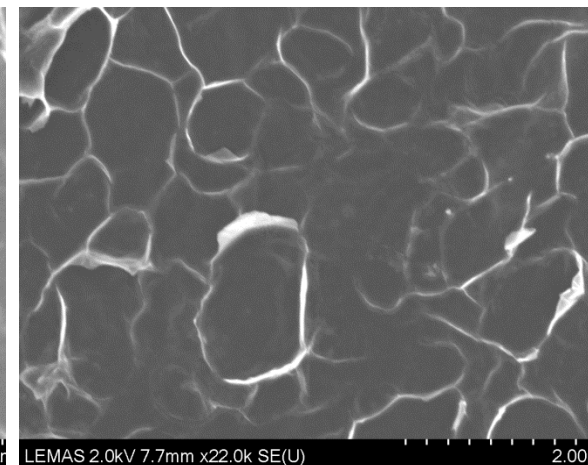
Figure 54-EDX spectrum of a membrane used in a Peptide 1 peptide dewatering process
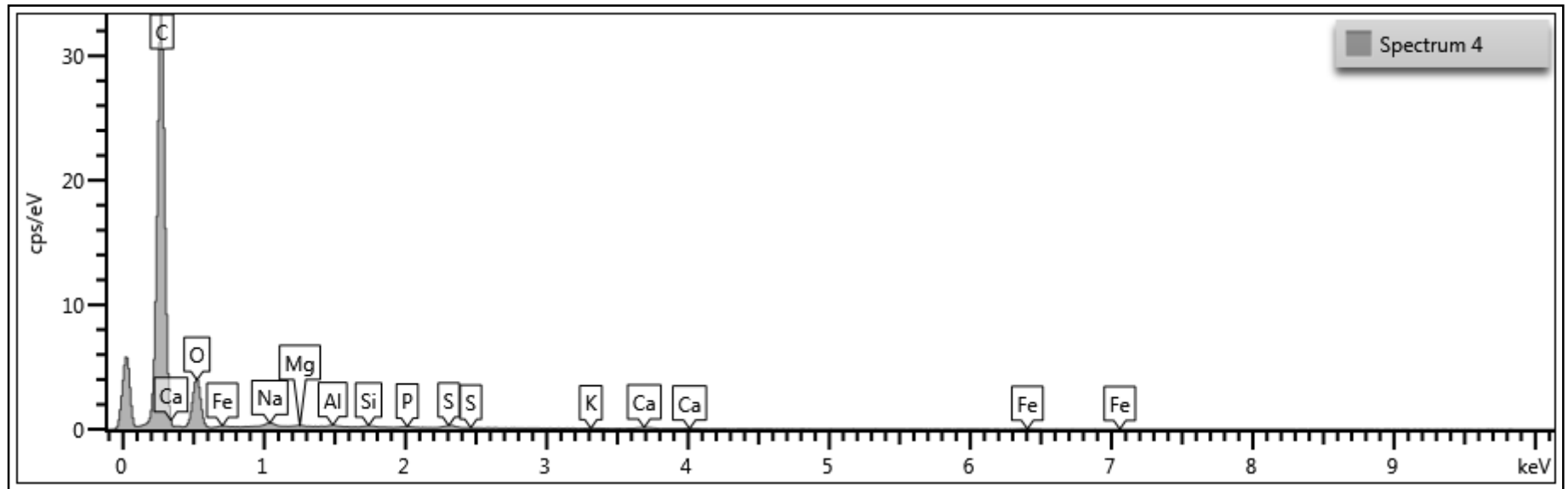
Spectrum 4

Element	Wt%	Element	Wt%
C	78.62	S	0.57
O	17.15	K	0.15
Na	0.45	Ca	0.73
Mg	0.12	Fe	1.63
Al	0.18	Total:	100.00
Si	0.24		
P	0.17		

Electron Image 4
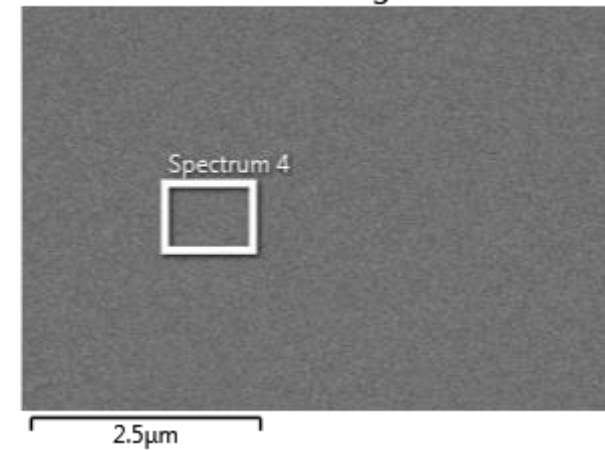
Figure 55-EDX spectrum of a membrane used in a Peptide 3 peptide dewatering process
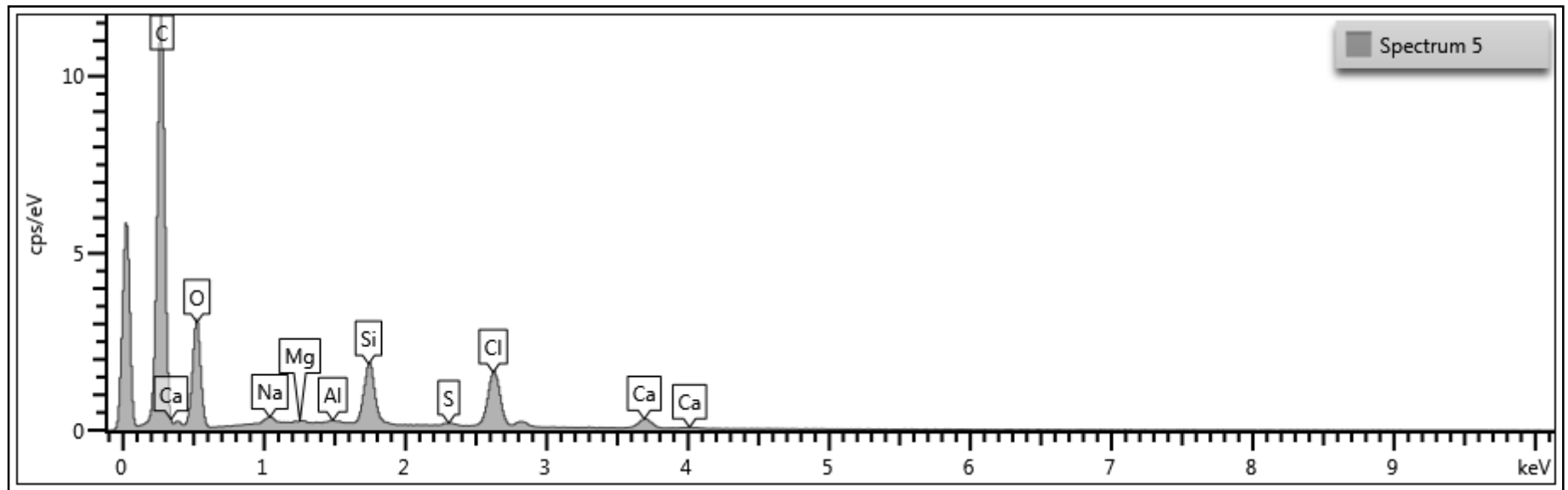
Spectrum 5

Element	Wt%	Element	Wt%
C	67.19	Cl	7.67
O	17.26	Ca	2.53
Na	0.36	Total:	100.00
Mg	0.12		
Al	0.15		
Si	4.42		
S	0.29		

Electron Image 5

1µm
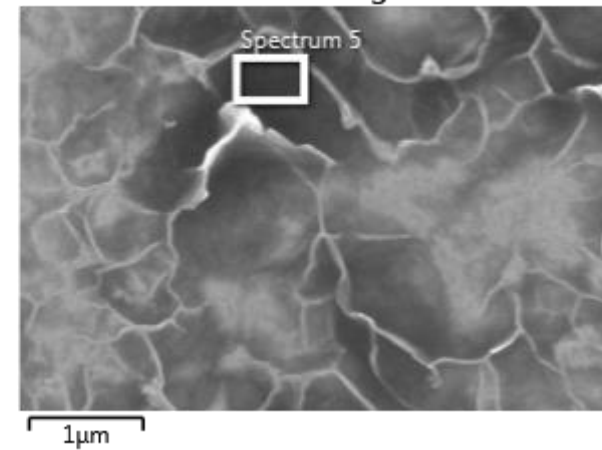
Figure 56-EDX spectrum of a membrane used in a Peptide 2 peptide dewatering process (scan1)
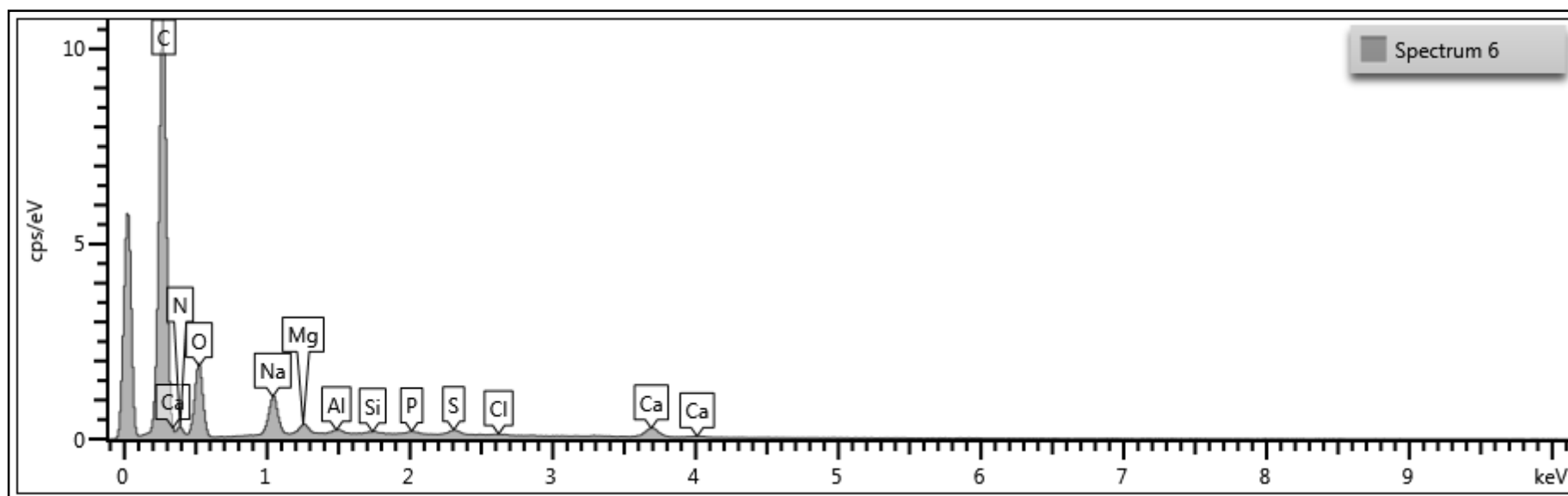
Spectrum 6

Element	Wt%	Element	Wt%
C	62.29	S	0.75
N	9.11	Cl	0.22
O	18.22	Ca	3.72
Na	3.81	Total:	100.00
Mg	0.90		
Al	0.39		
Si	0.22		
P	0.37		

Electron Image 6
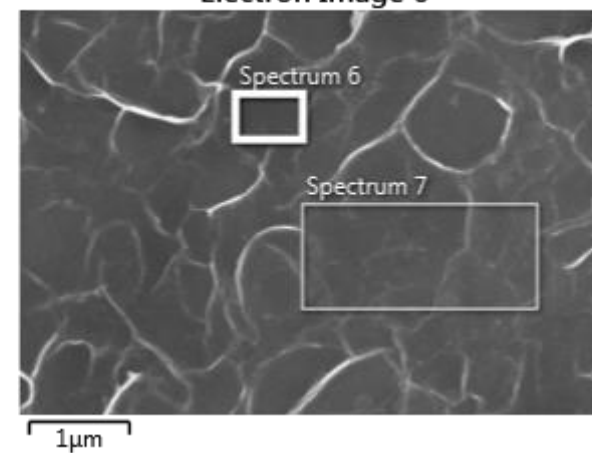
To complement SEM visual analysis and EDX, surface hydrophilicity was tested by measuring water droplet contact angle. Images of the water contact angles are shown in Figure 57. Membranes exposed to the peptide dewatering process exhibited larger contact angles leading to a reduced membrane surface hydrophilicity. It is not known whether the change in the contact angle was a result of adhered peptides to the surface or there has been G.O. membrane degradation.
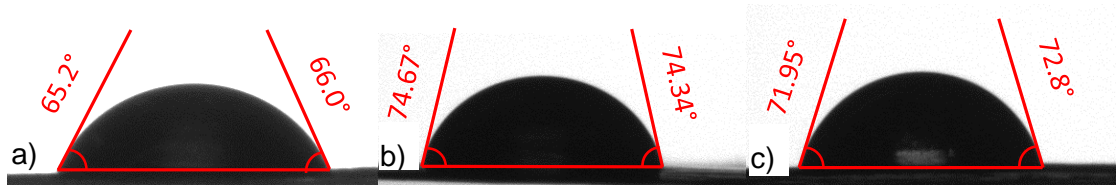
Figure 57 – Water contact angles of a) Unused membrane, b) Peptide 3 peptide exposed membrane, and c) Peptide 2 peptide exposed membrane

All three peptides demonstrated very similar rate of permeation trend lines. The process was separated into three segments: i) high initial flux and exponential decay, ii) constant rate of permeation, and iii) linear drop in the rate of pervaporation. SEM and EDX analysis confirmed peptide presence on the surface of the membrane, however, it is not clear whether there was any preferential fouling by any certain fraction of the peptides in the solution. Furthermore, the surface water contact angle has changed and the membranes became less hydrophilic after exposure to an alkaline and acidic aqueous peptide solutions. Currently, it is not clear if it is possible to regenerate the membrane surface or has it been permanently altered.

Peptides and proteins are known to accumulate on a surface of a membrane and produce a fouling layer over time. It is difficult to determine whether there is a specific set of compounds responsible for the loss of the rate of water permeation. An in depth review has been previously published covering various aspects contributing to the surface fouling and analysis methods used to investigate cake layer.[120] In this instance, more experimentation is required to determine the exact nature of the membrane deactivation.

6 Process Modelling and Economics

The purpose of this chapter is to evaluate the economic benefits of a pervaporation process using G.O. membranes. Dewatering of an aqueous IPA solution was selected as a case study. Membrane process, modelled by an in-house developed code and Aspen Plus, is compared to an azeotropic distillation, modelled by Aspen Plus, in terms of their energy consumption. Furthermore, G.O. membrane capability to dehydrate aqueous IPA solution to a various degrees of water content are discussed. The design specifications of the selected case study are summarised in Table 27.

Table 27-Selected case study design specifications

Components	Flow (kg h^{-1})	Temperature (°C)	Pressure (bar)	Product Purity (wt%)	Recovery (%)
IPA	700	25	1.01	95	99
Water	300	25	1.01	>99	$\cong$87.8

IPA is a bulk chemical used in many different industries with the total annual production of 550,000 tons in 1992 in Europe.[123] It is mainly encountered as a solvent in paint and plastic manufacturing.[123] The compound can also be used as a reactant in the production of mono-isopropyl amine and isopropyl acetate.[124] Frequently, the IPA waste stream contains water and it is desired to recycle the organic solvent. [123] A water rich IPA waste stream forms a minimum boiling point (80.4°C) azeotropic mixture (87.7 wt%, IPA, 1.01 bar), Figure 58. As mentioned before, this mixture cannot be separated by a conventional distillation and an azeotropic distillation has to be used. The process is typically very energy intensive and expensive to run.[8]Pervaporation is seen as an energy saving alternative and is frequently implemented on a large scale.[123]
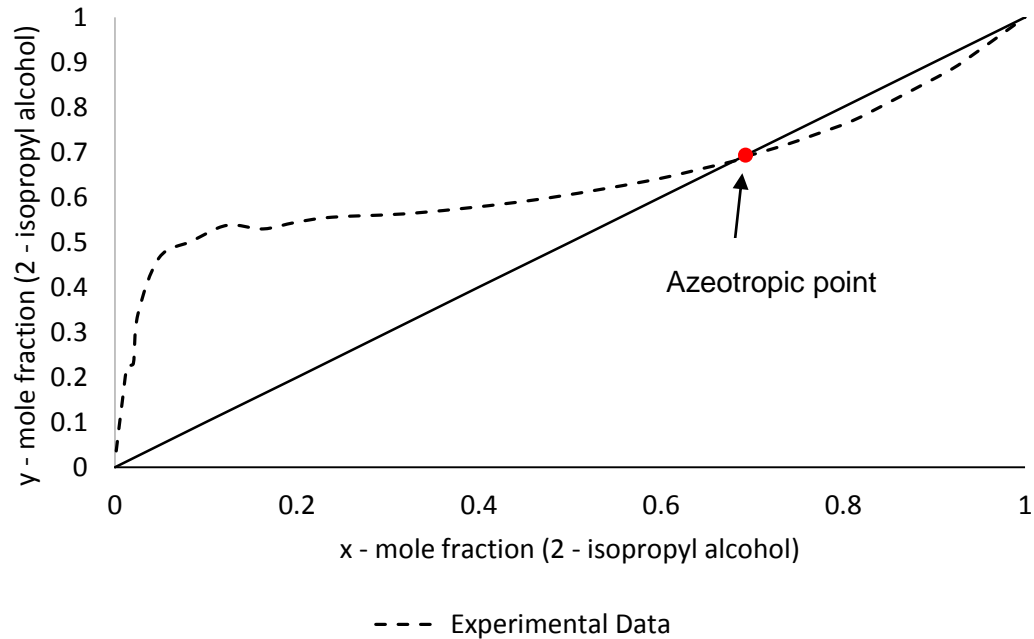
Figure 58 - x-y diagram of IPA and water[125]

6.1 Process

Homogeneous distillation (extractive distillation) separates the two components that otherwise would produce an azeotrope by introducing a third component into the mixture. The third component alters relative volatility of the system from unity without introducing another azeotrope or introducing a liquid phase splitting. The design of an azeotropic distillation mainly involves: i) selection of entrainers, and ii) the choice of the column configuration.[126]

Several solvents can be used in IPA/Water extractive distillation process. The two most common are ethylene glycol and DMSO.[127] Previous studies showed that DMSO has the largest separation power and doesn't produce any further azeotropes in the system, thus this solvent was selected for this study.[128]

A conventional extractive distillation process is composed of two columns, Figure 59. The entrainer and the aqueous alcohol mixture are fed into the Column1, where components are separated and IPA leaves as a top product. The bottom product of the Column1 is fed into the Column2 where the entrainer and water are separated. Typically, an optimised separation has minimal loss of the entrainer in the distillate products and it is possible to recycle the compound. Two other common strategies used in a separation of azeotropic

139

mixtures are: pressure swing distillation or heterogeneous azeotropic distillation. Some mixtures shift their azeotropic point when the pressure is changed, this can be used to separate the mixtures into its constituents. Heterogeneous azeotropic distillation introduces a third component which is not miscible with the mixture. This results in a natural phase split and removal of relatively high purity products.[123, 127, 129, 130]
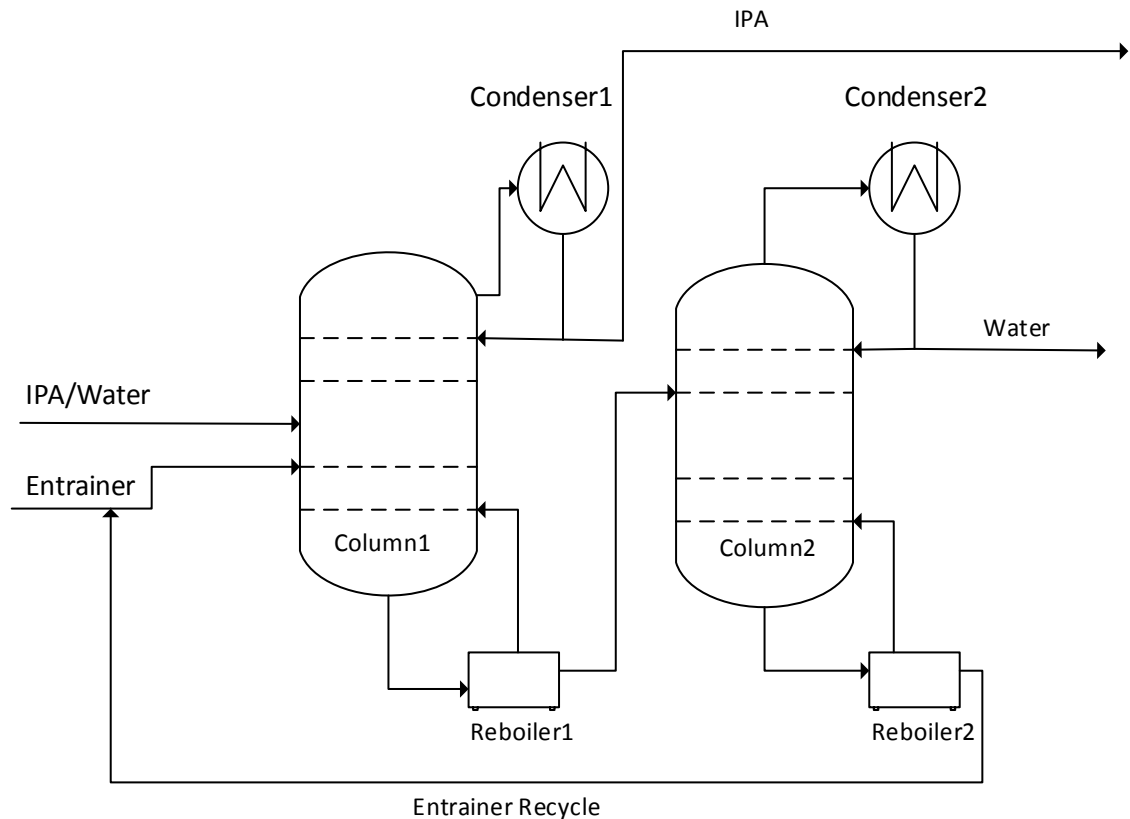
Figure 59-Conventional extractive distillation

6.2   Simulation method

Aspen Plus has 4 simulation methodologies for solving separation problems. The choice of the correct model is dictated by the complexity of the process. One of the common models is "SEP2", which is a general-purpose unit operation. It does not include the number of trays or a reflux ratio, therefore it is used just as a general screening tool. Another general distillation model is DSTWU. It uses Gilliland's (required reflux ratio for a specified number of stages), Winn's (minimum number of stages) and Underwood's (minimum reflux ratio) methods to calculate the number of stages and reflux ratios. Named shortcuts assume: i) constant molar overflow, and ii) constant relative volatility. However, due to the complexity of the extractive distillation, shortcut methods cannot be used to simulate the process.[131]

In this work a more rigorous model, RadFrac, is used, which can simulate a number of trays, random packing and structured packing in the column. This model is applicable to: i) conventional distillation, ii) absorption, and ii) extractive or azeotropic distillation. In this work it was assumed that equilibrium is reached at each stage, thus columns were set in equilibrium mode. Alternatively, Murphree or vaporisation efficiencies can be specified to solve this distillation problem.

The RadFrac model solves a number of simultaneous equations: phase equilibrium (Equation 75), component mass balance (Equation 76), total mass balance (Equation 77), and enthalpy balance (Equation 78). The mass flow balance is shown graphically in Figure 60. Initially the model either guesses temperature, pressure, liquid and vapour compositions and their corresponding flow rates or uses user provided values.

$$y_{i,n} - k_{i,n} X_{i,n} = 0 \qquad \text{Equation 75}$$

$$-l_{i,n-1} + l_{i,n} + v_{i,n} - v_{i,n+1} - f_{i,n} = 0 \qquad \text{Equation 76}$$

$$-L_{n-1} + L_n + V_n - V_{n+1} - F_n = 0 \qquad \text{Equation 77}$$

$$-H_{n-1}^L L_{n-1} + H_n^L L_n + H_n^V V_n - H_{n+1}^V V_{n+1} - F_n H_n^F - Q_n = 0 \qquad \text{Equation 78}$$
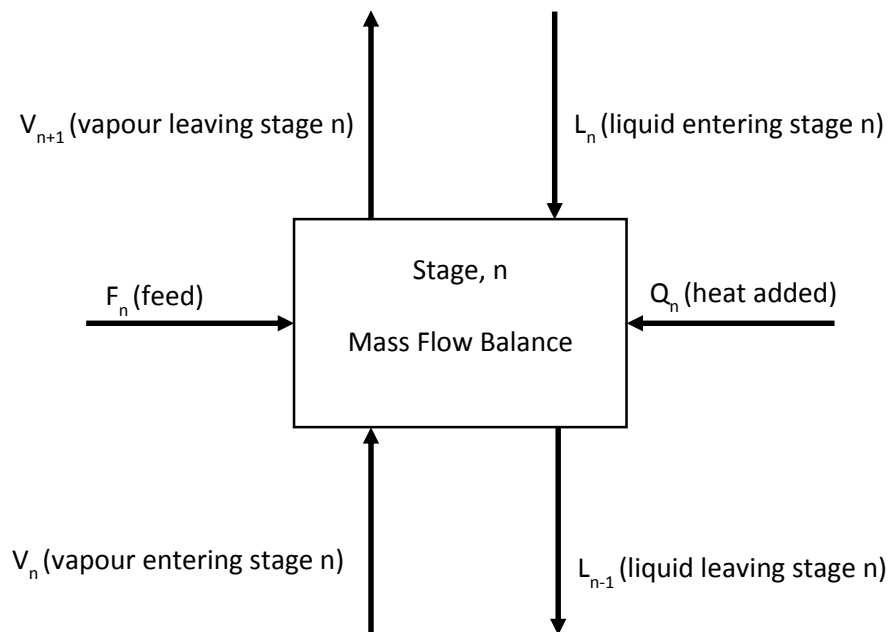
Figure 60 – Mass flow balance on a single stage

A Non-ideal algorithm was used to converge RadFrac column with a standard initialization technique, which is tailored to model a non-ideal mixture. The vapour phase was modelled as an ideal gas while a non-ideal liquid phase activity coefficient was calculated using the NRTL model. The NRTL model and parameters are shown in Equation 79, Equation 80 and Table 28.

Table 28-NRTL Parameters from Aspen Plus Properties Database

Parameter	Binary Pair		
Component i	WATER	WATER	IPA
Component j	IPA	DMSO	DMSO
AIJ	6.8284	-1.2449	0
AJI	-1.3115	1.7524	0
BIJ	-1483.4573	586.801	115.2787
BJI	426.3978	-1130.2155	-25.0123
CIJ	0.3	0.3	0.3

$$\ln(\gamma_i) = \frac{\sum_j x_j \tau_{ji} G_{ji}}{\sum_k x_k G_{ki}} + \sum_j \frac{x_j G_{ij}}{\sum_k x_k G_{kj}} \left(\tau_{ij} - \frac{\sum_m x_m \tau_m G_{mj}}{\sum_k x_k G_{kj}} \right)$$

Equation 79

Where

$$G_{ij} = \exp(-\alpha_{ij}\tau_{ij}), \tau_{ij} = \alpha_{ij} + \frac{b_{ij}}{T}, \alpha_{ij} = c_{ij}, \tau_{ii} = 0, G_{ii} = 1$$

Equation 80

A homogeneous extractive distillation of Water/IPA solution using DMSO as an entrainer was optimised for the re-boiler duty by varying the following parameters: i) DMSO flow rate, ii) total number of stages iii) feed stage of IPA/Water, and iv) feed stage of DMSO. Optimal conditions were found using typical optimisation strategy [127]:

1. Guess initial DMSO feed flow rate
2. Guess a total number of plates
3. Guess fresh feed and DMSO feed stages in the column (DMSO below the IPA/Water feed)
4. Set the distillate flow rate (based on the process specifications)
5. Change DMSO flow rate and re-boiler duty until design specifications are met
6. Lower feed stages to a minimum
7. Change DMSO and IPA/Water feed stages
8. Repeat step 5

The extractive distillation process has two columns, which makes it computationally intensive to optimise all variables at the same time. Thus an extractive column was optimised first, because it was more important to reach the desired dewatered alcohol purity than the quality of the water waste stream.

6.3   Energy Consumption Modelling-Distillation

An optimised azeotropic distillation process is shown in Figure 61. The first column was composed of 20 theoretical stages (including condenser and re-boiler). Preheated Water/IPA solution was fed into the extractive column above stage 16 and the entrainer was fed above stage 3. The column section between the Water/IPA feed and the entrainer feed is called an extraction zone. The purpose of this section is to strip out water by lowering the relative volatility of the water using DMSO. The water then leaves the column as a bottom product. The top part of the column (above DMSO feed) contains mainly IPA and a minute amount of water. This component mixture does not form an azeotrope, thus the light component (IPA) is separated from the high boiling point DMSO and leaves as a top product.

The optimised entrainer recovery column was composed of 10 theoretical stages (including re-boiler and condenser). The distillate product was almost pure (99.99wt%) water and a small amount of DMSO (0.01 wt%); the bottom product of the column high purity DMSO, which was suitable for a recycle
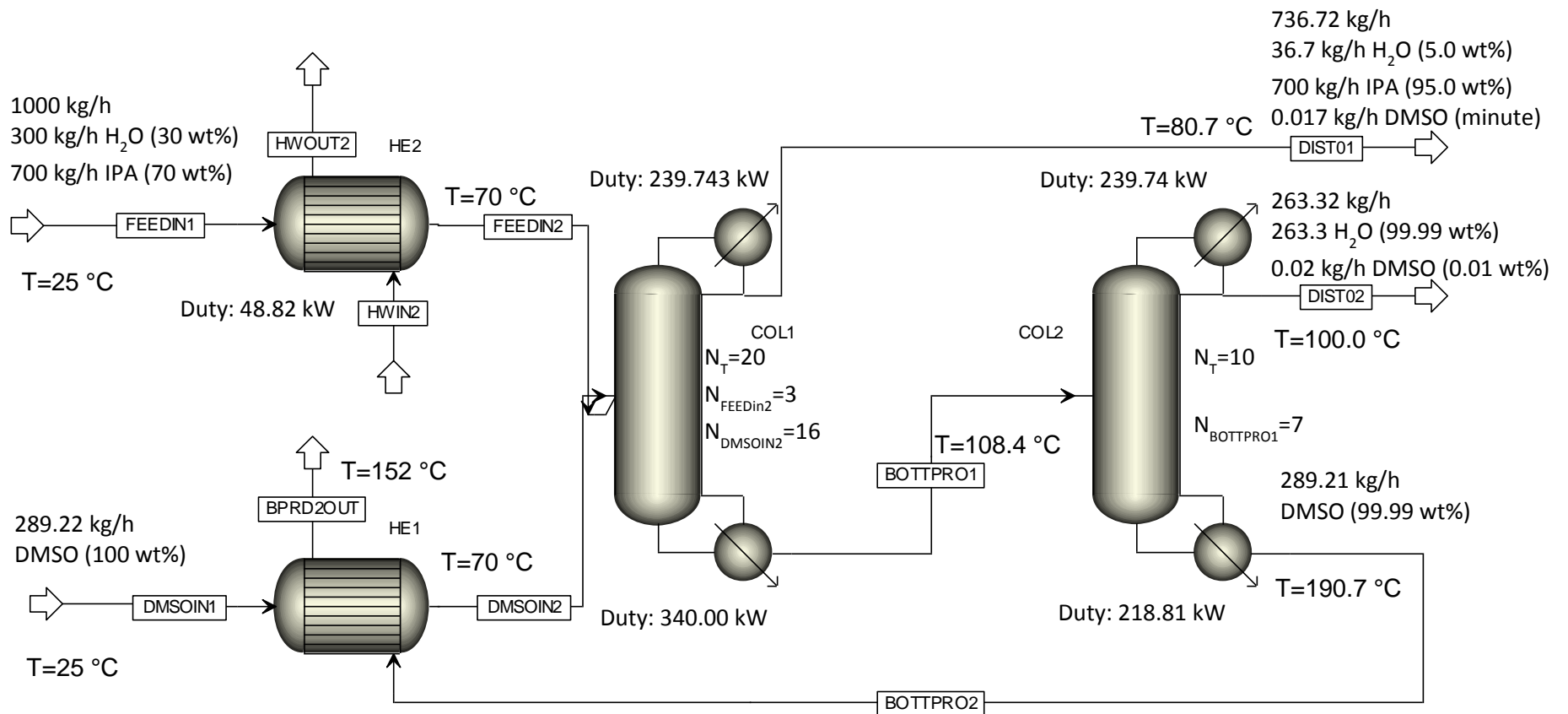
Figure 61-Extractive distillation of the IPA

Liquid composition profiles of the extractive column are shown in Figure 62. The goal of the DMSO (change relative volatility in the extractive column) was achieved and the majority of the water was retained in the extraction section. The distillate product was composed of 95wt% IPA and 5wt% water with minute amounts of DMSO; this was deemed to be acceptable. The stripping section, between the plates 16 and 20, had a rapidly diminishing amount of IPA. As the lightest component IPA evaporated and was returned to the extractive part of the column. The bottom product was composed of 52.34wt% DMSO and 47.65wt% water. The amount of IPA leaving as a bottom product was negligible, thus the overall recovery of the compound was greater than 99.99 wt%.
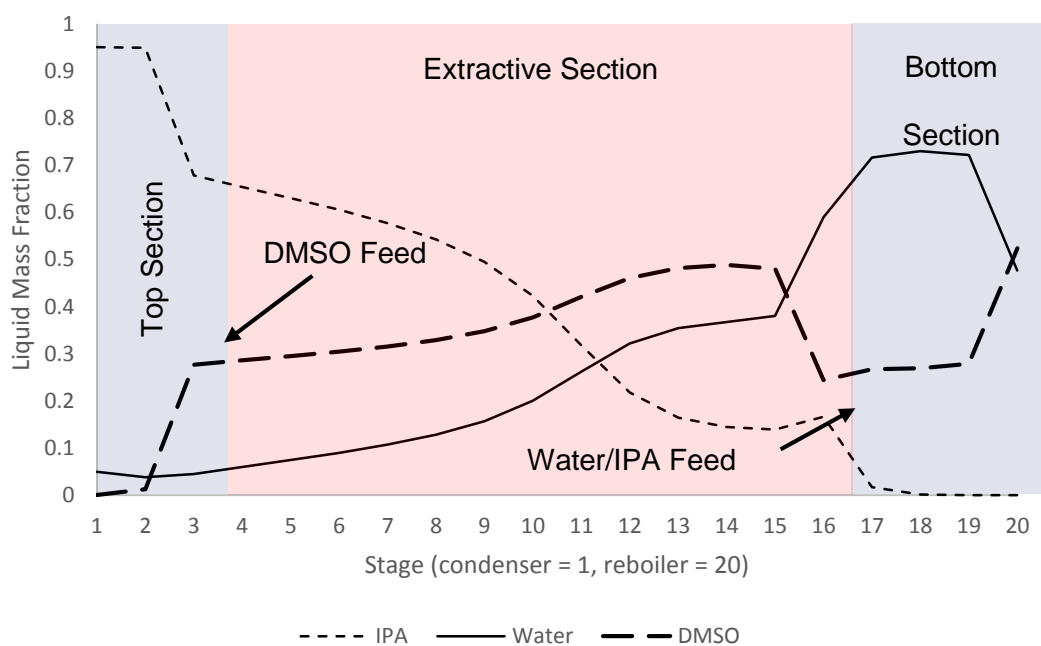
Figure 62 - Composition profiles in the extractive column

The purpose of the second column was to recover the entrainer (DMSO) and produce high purity water as the distillate. The composition profile of the recovery column is shown in Figure 63. Very high purity water, 99.99wt%, was obtained as a distillate and only 0.006 wt% DMSO was lost through the top product of the recovery column. The bottom product of the recovery column resulted in a high 99.99wt% DMSO purity. The recovered entrainer can then be reused as a feed stream to the extractive column (not shown in Figure 61).
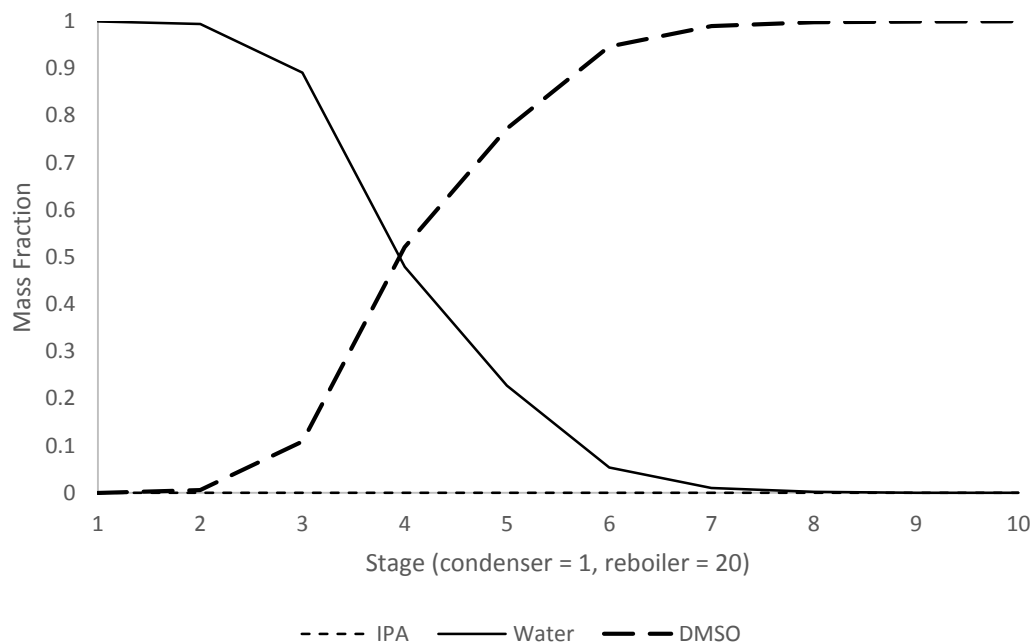
Figure 63 - Composition profiles in the entrainer recovery column

Extractive distillation is known to be an energy intensive process.[132] The breakdown of the energy consumed in the separation is shown in Table 29. The majority of the energy (55.96%) is consumed by the first column where IPA was separated. The second largest energy consumer (36.01%) was a DMSO recovery column. A small portion of the total energy (8.03%) was consumed by the pre-heating of fresh Water/IPA stream. It was possible to eliminate the pre-heating energy penalty of the DMSO stream by re-using the heat of the bottom product coming from the second column. In order to make an objective energy budget comparison between distillation and other separation processes, energy required per kilogram of product produced was calculated, Table 29.

Table 29-Energy consumption of azeotropic distillation process

Unit operation	Energy Consumed	The percentage of the total energy consumed
HE1	48.82 kW	8.03%
COL1	340.00 kW	55.96%
COL2	218.81 kW	36.01%
Total	607.63 kW	100%
Energy	2969.28 kJ/kg	N/A

7 Pervaporation separation of Water/IPA mixtures

7.1 Process

Membrane process modelling can be split into three distinct parts which serve different purposes: i) membrane scale-parameter estimation, ii) unit scale-mass and heat transfer in the module assessment, and iii) large scale-process economics study of the whole operation.[8, 133, 134]

Membrane scale modelling has a rich history and many different theories have been proposed over time. An in-depth review of multiple available models has been published recently.[135] The difficulty in applying these models arise from the lack of their applicability for different solute, solvent and membrane material systems. Recently, seven different membrane separation models have been compared with each other in terms of their fit to the experimental data. It was shown that solution-diffusion based models gave a better fit to a permeation data collected from a flexible-chain glassy membranes whereas the pore-flow model gave a better fit to the data obtained from a glassy membranes with a rigid structure. [136] A simulation of a membrane separation process requires the selection of an appropriate permeation model and some experimental effort to support the model selection.

At a modular scale it is assumed that the correct model for the permeation has been selected. The simulation focus shifts towards the fluid dynamics and mass transfer properties in the membrane module.[136] On this scale, the concentration polarisation and temperature gradients become important, and If not appropriately addressed, the performance of the process can be significantly impeded.

To address the issue of the concentration polarisation several experimental strategies have been developed.[85] One of the methods makes use of the concentration polarisation expression, Equation 81. The model relies on a correlation between the liquid boundary layer thickness and process fluid velocity, Equation 82.

$$\ln\left(1 - \frac{1}{E}\right) = \ln\left(1 - \frac{1}{E_0}\right) - \frac{J_v y_l}{D_w} \qquad \text{Equation 81}$$

$$\frac{D_w}{y_l} = K u^n \qquad \text{Equation 82}$$

The model parameters are determined by a linear regression of Equation 81, which gives an intrinsic enrichment factor, E_0, as a function of the fluid velocity.[85] Thereafter, the ratio

of the E/E_0 is calculated, which gives the magnitude of the concentration polarisation in the membrane equipment.

Heat transfer effects are typically accounted by considering dimensionless group correlations and heat balance equations.[94] These concepts link fluid velocity and temperature to the permeation flux profile in the membrane module.

Liquid mass transfer coefficient is typically determined by varying liquid flowrate on the process side followed by a parameter fitting to a pervaporation equation. This method is commonly used among membrane researchers.[94] Another option, is to apply dimensionless mass transfer coefficient correlations however, this works only when mass transfer correlations for a given membrane configuration are available.[137] Alternatively, mass transfer coefficients can be studied by varying the membrane thickness while the process liquid flowrate is kept constant. This methodology allows separating the liquid and membrane mass transfer coefficients. It has to be noted that in order for this method to work membrane has to present a significant part of the overall resistance.[83]

If membrane material is close to commercialisation at this scale the type of the membrane module should be selected. There are several different options to choose from: spiral wound, plate and frame, and tubular. The design of the membrane module is mainly determined by several factors such as: i) cost of the process, ii) fouling control, ii) pressure drop, iii) the desired operation pressure, and iv) material compatibility.[11]

Large-scale modelling is focused on the capital and operating costs of the pervaporation alone or in a combination with other chemical engineering processes. Lipnizki has produced a review article covering a large number of pervaporation case studies.[134] Typically, the results of large scale pervaporation modelling show significantly reduced operating costs and smaller capital investment.[8, 134]

7.2 Simulation methodology and process energy requirement

There is no "ready to use" pervaporation model in the Aspen Plus simulation package. To circumvent this issue and calculate pervaporation energy consumption a model separation was set-up, Figure 64. The model was split into three parts: i) pre-heating of the process fluid, ii) separation of the components, and iii) evaporation of the water rich stream (permeate). A heat exchanger (HE1) was used to pre-heat the process stream from 25°C to the pervaporation temperature (70°C) which was then fed into the separator (SEP). Separation in this unit is based on user defined split values for each component, coupled to

a rigorous flash calculation to determine the energy required for the separation. It is usually used as a simplified representation of a distillation process when separation is achieved or the column is known but the details of the process are not important. In this block, the top product was set to match the design specifications and leave the process in the liquid phase, while the bottom product (water rich stream) was flashed into vapour, imitating the phase change in a pervaporation process.

Overall energy requirements were calculated using Equation 83.

$$E_{pre-heat} + E_{phase\ change} + E_{vacuum\ pump} = E_{total}$$ Equation 83

Where $E_{pre-heat}$ is energy of the pre-heater (kW), $E_{phase\ change}$, the energy associated with the phase change of the permeate (kW), $E_{vacuum\ pump}$ is energy calculation required to run vacuum pump. The pre-heater and the phase change energy requirements were estimated by Aspen Plus. The vacuum pump electric power was calculated using Equation 84.[138]

Equation 84

$$E_{vacuum\ pump} = n_{permeate} R T_{perm} \frac{1}{\eta_{vac}} \frac{\gamma_{gas}}{\gamma_{gas} - 1} \left(\left(\frac{P_{atmopheric}}{P_{permeate}} \right)^{\frac{\gamma_{gas}-1}{\gamma_{gas}}} - 1 \right)$$

Where $E_{vacuum\ pump}$ is electric energy required to run the vacuum pump (W), $n_{permeate}$ is a molar flow of permeate (mol s^{-1}), R is the ideal gas constant (J mol^{-1} K^{-1}), T is permeate temperature (K), η is the vacuum pump efficiency, γ_{gas} is an adiabatic expansion coefficient, $P_{atmospheric}$ is atmospheric pressure (bar), and $P_{permeate}$ is the permeate side pressure, which was set at 30 mbar. The vacuum pump efficiency was calculated using Equation 85.[139]

$$\eta = 0.1058 \ln \left(\frac{P_{permeate}}{P_{process}} \right) + 0.8746$$ Equation 85

Where $P_{process}$ is water vapour pressure on the process side (bar). The electric power was then converted to thermal energy using the following conversion 1 kW electric = 2 kW thermal.

Energy savings provided by the membrane separation were calculated using Equation 86

$$100 - \frac{Energy(Pervaporation)}{Energy(Distillation)} * 100$$ Equation 86

736.7 kg/h (Liquid)
36.7 kg/h H_2O (5 wt%)
700 kg/h IPA (95 wt%)

IPA

T = 70 °C

SEP

Hot Water
Outlet

1000 kg/h
300 kg/h H_2O (30 wt%)
700 kg/h IPA (70 wt%)

HOUT

HE1

FEED1

FEED2

T = 25 °C   Duty: 25.5 kW   T = 70 °C   Duty: 178.35 kW

HIN

WATER

Hot Water
Inlet

263.3 kg/h (Vapour)
263.3 kg/h H_2O (100.00 wt%)

T = 70 °C
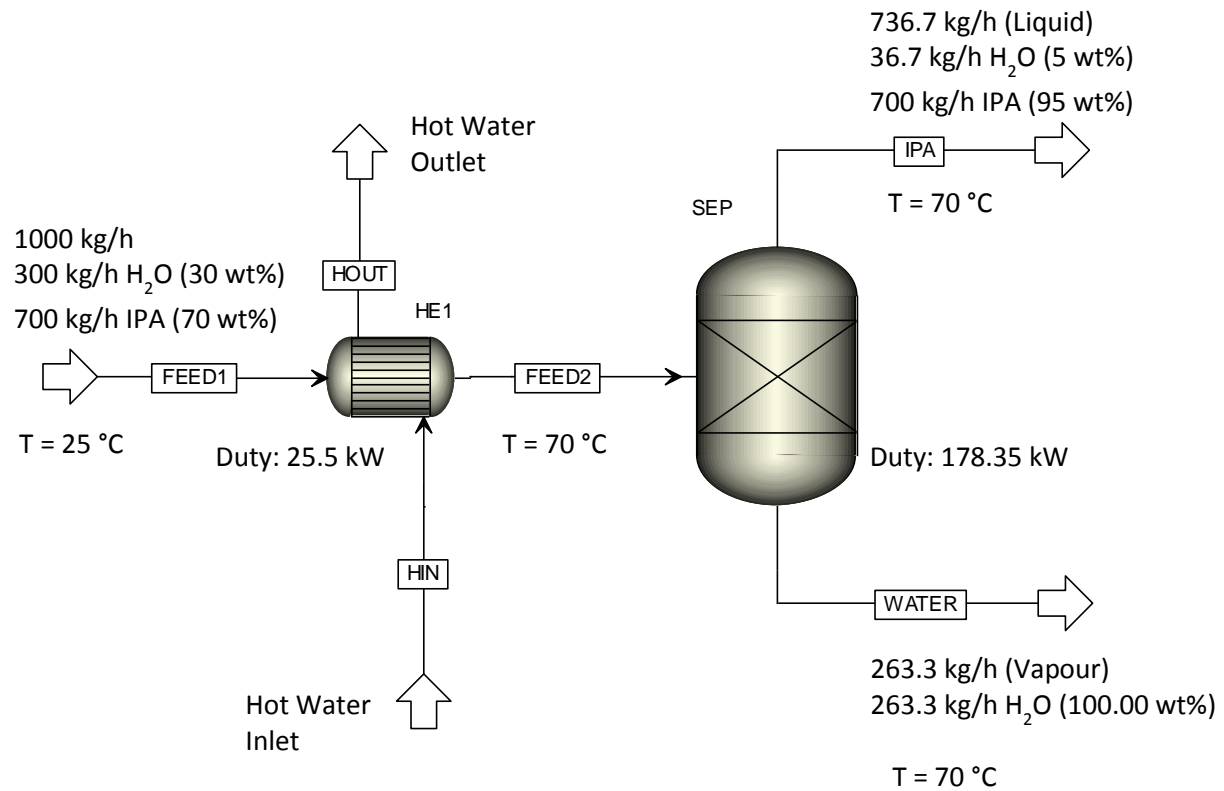
Total Duty: 175.49 kW
Energy of Permeation = 862.41 kJ/kg

Figure 64 – Pervaporation energy requirement simulation

150

The overall energy requirements of the pervaporation process are shown in Table 30. The energy required for the evaporation of the permeate stream has dwarfed the pre-heater energy requirements. Interestingly, the heat required (thermal equivalent) to maintain vacuum (30 mbar) on the permeate side was almost as high as the energy required for the evaporation. This makes maintaining vacuum an important consideration when designing pervaporation process and a trade-off between the vacuum pump operating cost and the reduced permeation flux should be carefully assessed. A similar energy penalty in a pervaporation research was found previously while studying acetic acid dewatering process. [8]

Table 30-Energy consumption of a membrane separation process

Unit operation	Energy Consumed (thermal)	The percentage of the total energy consumed
HE1	25.5 kW	6.87%
SEP	178.35 kW	48.05%
Vacuum pump	167.31 kW	45.08%
Total	371.16 kW	100%
Energy	1813.73 kJ/kg	N/A

7.3 Economic assessment

7.4 Pervaporation and distillation energy consumption

A combined pervaporation and distillation energy budget data is shown in Table 31. In this study pervaporation process was able to provide a 39% reduction in the energy consumption, which is a significant portion of the variable operating cost. The energy requirements could further be reduced for both processes by adding heat integration solutions. Naturally, this is only a facile comparison between the two processes and a more in depth process capital and operating cost analysis is required, which is out of the scope of this study. However, this finding was in agreement with a previous extensive review of the pervaporation use in industrial applications where the membrane process was shown to bring economic benefits in terms of capital and operating costs.[134]

Table 31-Pervaporation and distillation energy requirements

Unit operation (Pervaporation)	Energy Consumed (thermal)	Unit operation (Distillation)	Energy Consumed (thermal)
HE1	25.5 kW	HE1	48.82 kW
SEP	178.35 kW	COL1	340.00 kW
Vacuum pump	167.31 kW	COL2	218.81 kW
Total	371.16 kW	Total	607.63 kW
Energy	1813.73 kJ kg^{-1}	Energy	2969.28 kJ kg^{-1}

7.5   Membrane surface area requirements and cost

While reduction in the energy consumption can deliver significant operating savings, the change in the process from distillation to pervaporation can only be justified if the required surface area of the membrane module is not excessive. Experimental data from the "Organic Solvent Dehydration" chapter was used to develop a pervaporation cell simulation software. The programme was designed to estimate the final water concentration in the process stream based on the following process parameters: i) time of the operation, ii) membrane surface area, iii) process fluid flow rate, iv) process temperature, and v) initial water concentration. A schematic diagram of the software is shown in Figure 65. The rate of permeation was calculated using a solution-diffusion model with the extra term relating G.O. material sensitivity to the water concentration in the process fluid, Equation 87. Water in IPA partial pressure calculations were not performed as a part of this simulation, instead exported data from Aspen Plus Properties was used.

Pervaporation simulation makes the following assumptions: i) pervaporation operates isothermally ii) an ideal separation between water and IPA is ascertained, iii) liquid side mass transfer limitation is negligible, iv) there is no pressure drop in the module, and v) there is no membrane surface degradation. It is important to note that previous literature shows a small amount of propanol (3.6×10^{-4} kg h^{-1} m^{-2}) can permeate through a G.O. membrane (5 µm) at a room temperature compared to significantly larger water rates of permeation (0.146 kg h^{-1} m^{-2}, 4 µm) .[16, 140] In this work this was assumed to be negligible.

Surface area of the module was estimated by diving the entire unit into multiple submodules. In each module local mole balance was calculated. The mass of the N+1 step was a sum of the mole flow of N step and the rate of permeation, Equation 88. The calculated retentate

was then fed into the consecutive module until the number of user input steps was reached, Equation 89. A schematic view of the theoretical model is shown in Figure 66 and Figure 67.

$$J = k_{M.P} x (P_{W.L} - P_{W.P})$$

Equation 87

$$n_{f,N+1} = n_{f,N} + \frac{Q_{liquid} * A}{M}$$

Equation 88

$$n_{f,N-1} = n_{f,N}, N = 1, 2, 3, \dots \dots N$$

Equation 89

Input Parameters:

Process fluid flow rate

Water concentration

Temperature

Estimate

pervaporation flux

based on the process

Data logging

Log the process data

in excel sheet

No

If iteration = process steps

Yes
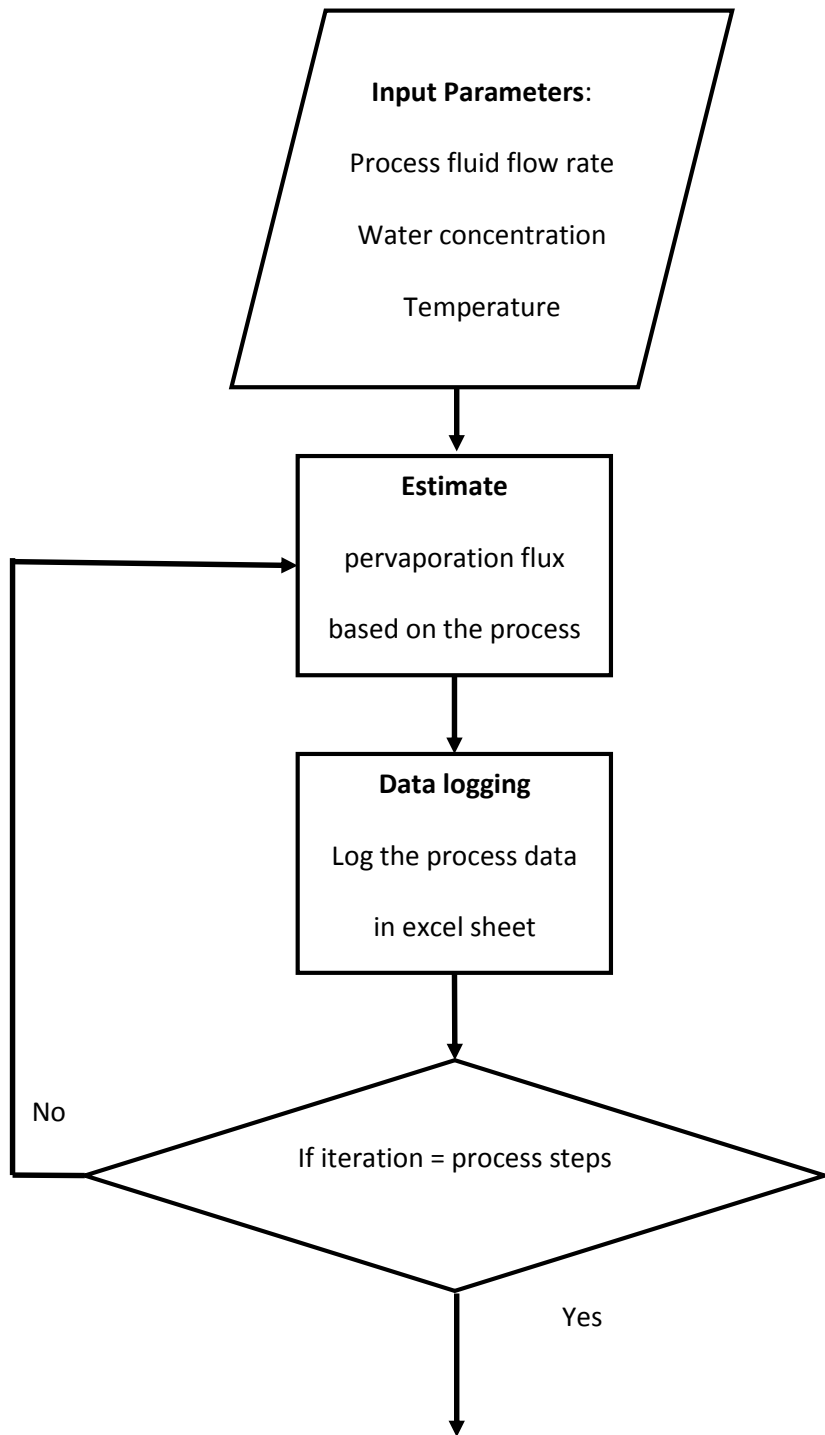
Figure 65 – Pervaporation module surface area estimation program

Stage constants:

- Temperature
- Pressure
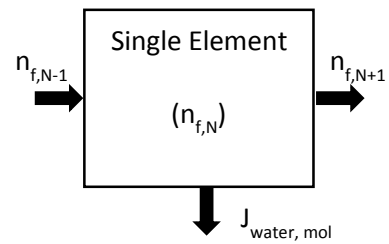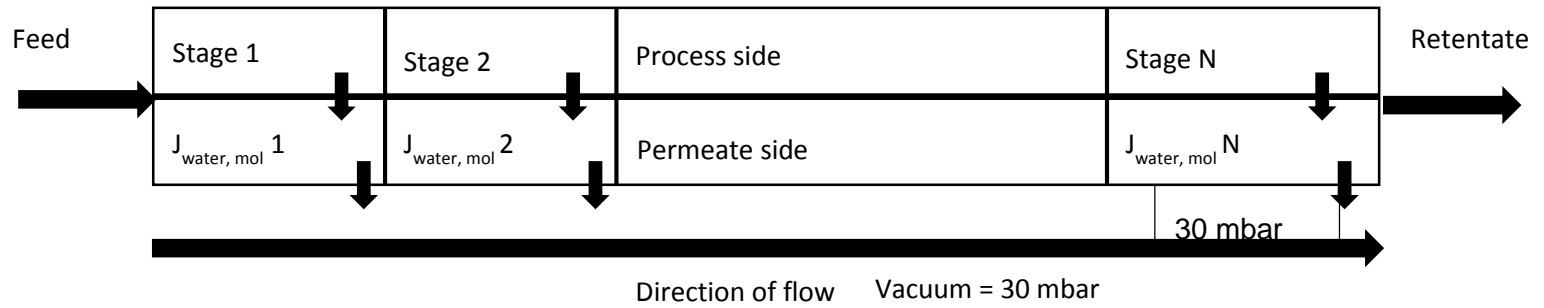
Figure 66 –Simulated pervaporation cell model[141]

Figure 67-Single block of a simulated pervaporation cell[141]

The capital cost of a membrane module primarily depends on the total surface area required. Several researchers have previously shown that a stand-alone membrane process may require an excessively high surface area which creates large capital expenditure and hinders the membrane process competitiveness.

An in-house built code was used to estimate the required membrane surface to dehydrate 1000 kg/h of 30wt% water in IPA to a various degrees of dryness. A pervaporation process using 2.1 μm G.O. membrane at 70°C was selected as this set of conditions had robust set of data. The required surface area change with respect to the final IPA concentration in the process solution is shown in Figure 68. There was a linear increase in the total membrane required surface area up to 97wt%. In order to achieve smaller amounts of water in the process solution the required surface area grows exponentially. This was the result of a decrease in the driving force across the membrane due to small water mole fraction on the retentate side. The effect is especially prominent when G.O. membranes are used, because of its mole fraction square relationship to the rate of permeation. However, this is not an unusual pervaporation membrane behaviour and has been demonstrated in a previous research.[132] Despite the exponential growth of the required surface, the feasibility of the process will be ultimately determined by the capital cost of the membrane module.

In this case study the design specification of 5 wt% water in IPA could be achieved with 380 m^2 membrane module. This is considered to be a small membrane operation. To the extent of our knowledge the largest pervaporation operation to date has 3000 m^2 membrane area.[8]
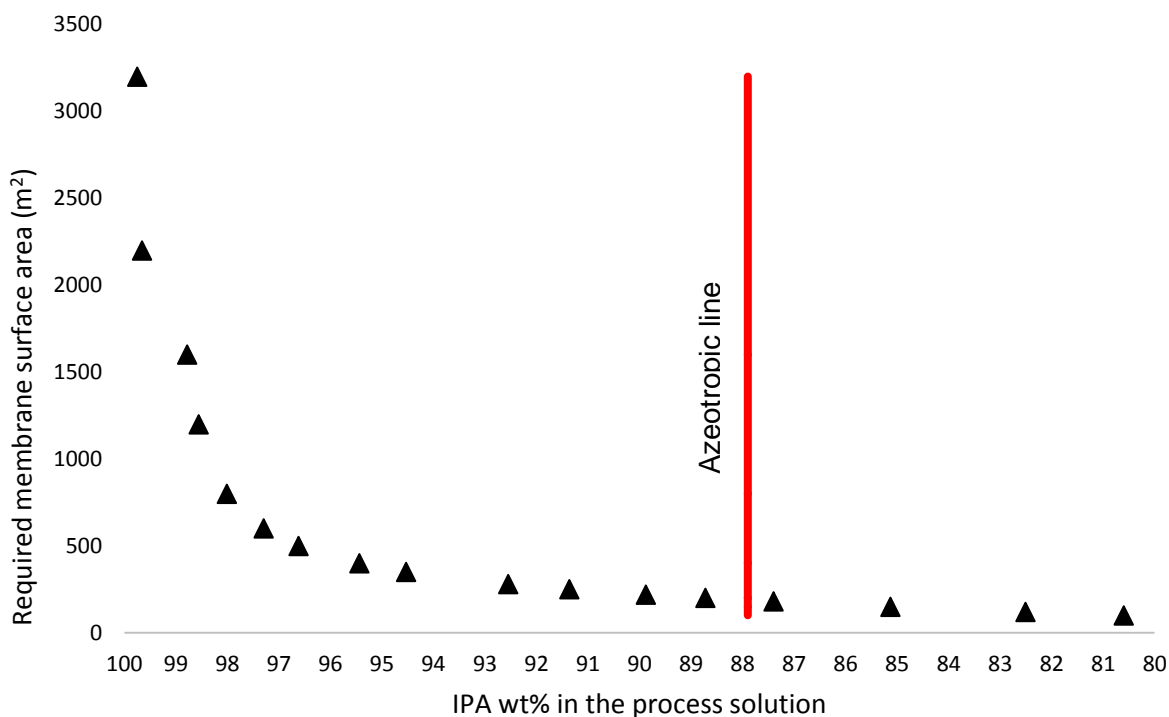
Figure 68-Required membrane surface area vs different degrees of dryness for 1000 kg/h 30wt% water in IPA using 2.1 µm G.O. membrane at 70°C

It is difficult to accurately estimate pervaporation process capital costs when the membrane material has not been commercialised. Firstly, we evaluate a lab-scale pricing, which is deemed to be the maximum cost of the membrane. This is followed by a brief discussion of the selective G.O. layer costs at a large scale.

To estimate a 2.1 µm thick G.O. membrane costs per square meter the following factors have been considered: the cost of the G.O. and the cost of the polymeric support. The cost of the G.O. was dictated by the price of the lab scale G.O. solution provider "Graphene-Supermarket". At the time of purchase a 0.87 g of a G.O. dispersed in water was priced at $200 (£129.03). The PVDF supports were acquired in a pack of 100 from a commercial microfiltration membrane supplier Millipore. The price of a single film was calculated as £0.98/film. Total price per membrane with a 9.1 cm^2 active surface area (used in this research) was £1.72. The price was then extrapolated to estimate the cost per square meter, Table 32. The price per square meter of the G.O. membranes was extraordinarily high and was on the same scale as inorganic their ceramic counterparts. [142]

Table 32-Lab scale costs of the G.O. membrane production

	Laboratory Scale		Extrapolated Price	
Unit	Price (£)	Scale	Price (£ m^{-2})	Scale
PVDF	0.98	17.35 cm^2	564.84	1 m^2
G.O.	0.74	9.1 cm^2 (5 mg)	813.19	1 m^2 (5.49 g)
Total	1.72	9.1 cm^2 (active surface area)	1378.03	1 m^2 (active surface area)

If the production is scaled up it is expected that the price of the membrane will significantly drop. The main price reduction is anticipated to stem from the cheap raw materials used in the G.O. synthesis [143] Typical prices of the raw materials used in the synthesis of the G.O. are listed in Table 33. Using these figures, the estimated cost per square meter of the selective G.O. layer is £0.02, which indicates a low raw material cost impact on the production of a selective film. A further price reduction per square meter would be possible if thinner membranes are made.

Table 33-Raw material prices used in the G.O. synthesis

Chemical	Price £/1000kg	Synthesis of 1g G.O.	Price £
Sulphuric Acid	153.72	60.5 g	0.0093
Potassium Permanganate	1281.02	4.29 g	0.0055
Sodium Nitrate	204.96	0.715 g	0.0001
Graphite	192.15	1.43 g	0.0003
Hydrogen Peroxide	256.2	8.1 g	0.0021
		Total	0.0173

Typically, polymeric pervaporation membranes cost £730 per m^2 of installed unit. The price goes up significantly when inorganic membranes are used to £2190 per m^2 of installed unit.[123] The price is also very sensitive to the selected pervaporation module design. If highly viscous fluids are used the price of polymeric membrane can go up to £1291-3229 per m^2.[85]

8 Conclusions and Future Research

8.1 Conclusions

G.O. as a water selective membrane has first emerged in 2012.[1] The researchers used the membrane in a vapour permeation mode to separate water from diatomic gasses and organic solvents.[16, 144] The membrane has shown excellent separation selectivity and rates of permeation. In a completely hydrated state the material allowed water to go through as fast as an open apparatus, thus presenting no mass transfer resistance for the permeating molecular species.

Many research groups have investigated G.O. membrane performance in pervaporation and vapour permeation modes.[1, 16, 73, 75, 100, 140] Despite the exciting results the scope of the conditions investigated is still fairly limited and there is a need for a more detailed research. This study is focused on the G.O. membrane pervaporation performance using model and industrial solvent mixtures.

The pervaporation was investigated using in-house built permeation cell. The design of the vessel and detailed drawings of the apparatus are shown in the "Methods and Materials" chapter. The pervaporation equipment was validated by a series of experiments were a trade-off between the liquid and membrane mass transfer coefficients with respect to the rate of agitation was determined. All of the remaining experiments were conducted in a high agitation region.

G.O. membrane stability was tested using water (20 wt%)/IPA (80 wt%) mixture at 80°C in a 7-day study. It was found that the rate of permeation continuously declined over the period of the study with the final rate of permeation value 38% lower than the initial value. This drop in the rate of permeation has not been previously reported and is the most important shortcoming of this material. The membrane selective layer chemical and physical properties were studied using SEM, EDX, XRD, FT-IR, and contact angle measurements. SEM, EDX and XRD have not revealed any significant G.O. membrane changes, which could have led to a drop in the rate of permeation. FT-IR studies revealed an increase in the alkane group presence on the membrane surface. Furthermore, the surface of the G.O. membrane has changed the water contact angle from an average value of 65.8° to 87.31°.

Three model aqueous organic solvent systems were studied: water/IPA, water/EtOH, and water/THF. The rate of permeation and membrane selectivity was comparable to the previous research discussed in "Organic Solvent Dehydration" chapter. A number of studies were conducted to investigate the rate of pervaporation and G.O. selectivity at

low water concentrations in the process solution. A deviation from a linear Solution-Diffusion model was found, which has not been reported previously. Interestingly, the rate of permeation becomes linear if an additional term of the water mole fraction is introduced. It is theorised that the non-linear relationship between rate of permeation and partial water vapour pressure originates from a well-documented G.O. material solvation by liquids such as water, EtOH and MeOH.[63] Overall, the G.O. membranes showed excellent results in the water separation from organic liquids and had a similar performance to the state-of-the-art and commercial pervaporation membranes, "Industrial Case Studies".

G.O. membrane potential in industrial applications was tested in the following case studies: i) MeOH/n-Hexane separation, ii) dewatering of aqueous peptides, and iii) water removal from an esterification of fatty carboxylic acid with IPA reaction mixture.

MeOH solvent separation was successful and the resulting permeate purity varied between 93-99.2 wt%. This offers an opportunity to selectively separate polar and non-polar solvent after second chromatographic separation step and improve the process by reducing the solvent waste.

Esterification of fatty carboxylic acid and IPA was used to test in-*situ* water removal from a reaction media. Initial experimentation showed a 19% increase in the yield compared to a reaction without a selective water removal. A repeat of the study without replacing the G.O. membrane resulted in a smaller 11% yield increase in the same time-frame. The membrane was examined using SEM and EDX analytical techniques, which have not shown any significant membrane changes compared to an unused G.O. membrane. Membrane surface chemistry change was investigated using FT-IR. A set of peaks emerged in the alkane C-H stretch region (2850-3000 cm^{-1}). Contact angle measurements showed a reduction in the surface hydrophilicity and an average contact angle increase from 65.6° to 83.3°.

A high water permeation flux was demonstrated in peptide dewatering studies. Despite good initial results G.O. membranes were prone to the peptide fouling and permeation flux reduction. The presence of the surface foulants was confirmed by SEM and EDX. Water contact angle measurements showed a reduction in the surface hydrophilicity. Currently, it is not clear whether the membrane surface fouling is reversible or irreversible. To elucidate whether permeation flux recovery is possible further research is required.

Pervaporation data from organic solvent dewatering studies was used to create a program which estimates the required surface area for a given water/IPA separation.

In addition, Aspen Plus was used to simulate pervaporation and extractive distillation of water/IPA mixture and estimate the required energy for the separation. To make an objective comparison between the process energy requirements to produce 1 kg of 95 wt% IPA was calculated. The extractive distillation process required 2.97 MJ kg^{-1} of IPA produced while pervaporation process required 1.81 MJ kg^{-1}. Pervaporation process resulted in a 39% energy reduction, which would directly translate into operating cost savings. Interestingly, vacuum pump energy consumption was a significant part of the overall energy needs and contributed 45.08% to the overall IPA dewatering energy budget. The energy requirements of the vacuum pump would be significantly smaller if a lower vacuum is applied on the permeate side. However, this would result in a larger membrane surface area requirement. It was estimated that 1000 kg h^{-1} 30wt% water in IPA mixture could be dehydrated to 95wt% IPA using 380 m^2 membrane module at 70°C.

Furthermore, it was found that due to G.O. material solvation by water the membrane surface area requirements start growing exponentially once there was less than 3wt% water in the process solution. This point marks a milestone beyond which alternative membrane materials would hold an upper hand in terms of rate of permeation. While G.O. membranes are less competitive at low water concentrations in the process solution and have exponential growth of the required membrane area this can be potentially offset by a cheap manufacturing costs. The raw materials used in the synthesis of the G.O. are cheap bulk chemicals, which lead to incredibly low selective surface manufacturing costs (0.02 £ m^{-1}).

8.2   Future Research

The most important future research avenue is the reduction in the permeate flux at elevated temperatures. A multi-layered G.O. membrane is known to have a minimal functional group change up to 100°C. [103] XRD, SEM, and EDX studies have indicated little to no change in the bulk of the material and physical appearance of the membrane. Thus, the loss in activity has to be associated with the surface functional groups. The issue has to be addressed before any further developments. A number of research publications and several review papers have been published on the G.O. functional group alteration.[57, 80, 145] This should serve as a prime source of information for a stable G.O. membrane surface chemistry research.

G.O. material production

There have been individual attempts to demonstrate how various factors such as: i) exfoliation, ii) parent graphite, and iii) oxidation methods, affects the final structure of the G.O. material. [144, 146, 147] Furthermore, it has been demonstrated that the graphite

oxidation reaction can affect the solvation of the final product in powder and membrane form.[63] Despite numerous individual research papers there is no published study which relates previously discussed processing steps to the membrane selectivity of the rate of permeation. Due to the size distribution of the parent graphite and non- homogeneously distributed functional groups it is suggested to employ design of experiments to establish the relationships between the membrane performance and its production route. This is a large potential research area which can offer development of a more permeable and selective G.O. based membrane.

G.O. selective layer is mechanically too fragile to be applied as a standalone membrane. The issue is circumvented by preparing anisotropic membranes where the G.O. layer is coated on a highly porous support. In this study G.O. was coated on a 70% porous hydrophilic PVDF membrane. Many other supports have been used.[1, 16, 75, 100] Most of them have been polymer based, which has given the flexible nature to the final product. Initial research papers have also indicated a pervaporation rate and selectivity difference among the G.O. membranes coated on different supports.[16] The reasons behind the varying performance have not been elucidated. Thus, there is still room for a more comprehensive study, which would bridge the gap between the nature of the support and the selective layer performance. Perhaps the most impressive water rates of permeation through G.O. membranes were demonstrated by a G.O. layer on a ceramic support.[75] The G.O. membrane production on ceramic supports has not been actively pursued and given the excellent results acquired in the prior publication this could be a highly rewarding field of research.

Moving forward the membrane process should be scaled-up and tested. While research in this body of work can serve as an excellent representation of a lab scale membrane performance it does not capture the challenges of a large scale pervaporation process. The most important issues to be addressed on a large scale G.O. membrane manufacturing will be the coating technique. Several options are available: i) spin-coating, ii) spray-coating, and iii) filtration-coating. It is not know which of these methods can deliver the most uniform selective layer and minimal amount of defects. In this study the thinnest membrane made had a 564 nm thick selective layer, which is larger than a typical commercial membrane thickness.[85] To the best of our knowledge the thinnest G.O. membrane had 97 nm thick selective layer which was coated on a thin film nanocomposite support.[100] A significant amount of effort should be focused on making the G.O. membranes thinner as this would significantly increase the rate of permeation.

9 Appendix

9.1 Appendix A Experimental Data

Table 34-Water/IPA (20wt%/80wt%) 7 day dewatering study, 80°C, 2.1 μm membrane

Entry	Total (kg h^{-1}m^{-2})	Water (kg h^{-1}m^{-2})	IPA (kg h^{-1}m^{-2})	Permeate (wt%)	Time	Date
1	1.3	1.25	0.05	96.32	2h09min	29.06.2015
2	1.37	1.33	0.04	97.24	1h30min	29.06.2015
3	1.3	1.27	0.03	97.56	2h18min	29.06.2015
4	0.84	0.82	0.02	97.96	1h22min	30.06.2015
5	1.18	1.16	0.02	98.39	1h41min	30.06.2015
6	1.087	1.07	0.02	98.35	2h10min	30.06.2015
7	0.96	0.94	0.02	98.30	1h57min	01.07.2015
8	1.17	1.15	0.02	98.60	1h30min	01.07.2015
9	0.85	0.84	0.01	98.70	2h14min	01.07.2015
10	1.11	1.09	0.02	98.60	1h17min	01.07.2015
11	0.82	0.81	0.01	98.80	2h02min	02.07.2015
12	1.018	1.01	0.01	98.96	1h40min	02.07.2015
13	0.94	0.93	0.01	98.90	1h44min	02.07.2015
14	0.79	0.78	0.01	98.70	1h00min	02.07.2015
15	0.8	0.79	0.01	98.85	2h02min	03.07.2015
16	0.94	0.93	0.01	98.90	1h50min	03.07.2015
17	0.95	0.94	0.01	98.50	1h11min	03.07.2015
18	0.7	0.69	0.01	99.00	1h20min	06.07.2015
19	0.77	0.76	0.01	99.00	2h05min	06.07.2015
20	0.78	0.77	0.01	98.80	1h53min	06.07.2015
21	0.8	0.79	0.01	98.85	2h16min	07.07.2015
22	0.9	0.89	0.01	99.02	2h10min	07.07.2015
23	0.86	0.82	0.04	95.17	1h12min	07.07.2015

Table 35-Water/IPA (30wt% / 70wt%) varying temperature (50-70°C) study, 2.1 µm membrane

Entry	Temperature (°C)	Total (kg h^{-1}m^{-2})	Water (kg h^{-1}m^{-2})	IPA (kg h^{-1}m^{-2})	Permeate (wt%)	Date
1		1.39	1.36	0.03	97.60	26022014
2		1.48	1.44	0.03	97.70	26022014
3	70	1.40	1.37	0.03	97.60	26022014
4		1.42	1.39	0.03	98.20	26022014
5		1.33	1.29	0.04	97.20	26022014
6		1.49	1.47	0.02	98.80	26022014
7		0.91	0.91	0.00	99.99	15022014
8		0.85	0.85	0.00	99.99	15022014
9	60	1.04	1.03	0.00	99.99	15022014
10		1.00	1.00	0.00	99.99	15022014
11		0.94	0.94	0.00	99.99	15022014
12		0.58	0.58	0.00	99.99	17022014
13		0.76	0.76	0.00	99.99	17022014
14		0.60	0.59	0.00	99.99	17022014
15		0.76	0.76	0.00	99.99	17022014
16		0.80	0.79	0.01	99.30	18022014
17		0.90	0.90	0.00	99.99	18022014
18	50	0.86	0.86	0.00	99.99	18022015
19		0.51	0.51	0.00	99.99	18022015
20		0.67	0.67	0.01	99.00	18022015
21		0.61	0.59	0.01	98.00	18022015
22		0.69	0.68	0.01	99.13	18022015
23		0.84	0.83	0.01	99.15	18022015
24		0.77	0.76	0.01	99.20	18022015

Table 36-Water / EtOH (30wt% / 70wt%) varying temperature (50-80°C) study, 2.1 µm membrane

Entry	Temperature (°C)	Total (kg h^{-1}m^{-2})	Water (kg h^{-1}m^{-2})	IPA (kg h^{-1}m^{-2})	Permeate (wt%)	Date
1		1.00	0.95	0.05	95.34	10.06.2015
2	70	1.03	0.98	0.05	95.46	10.06.2015
3		1.03	0.97	0.06	94.35	10.06.2015
4	50	0.40	0.38	0.02	95.03	15.06.2015
5		0.36	0.35	0.02	95.60	15.06.2015
6		1.21	1.16	0.05	95.64	15.06.2015
7	80	1.28	1.22	0.06	95.40	16.06.2015
8		1.13	1.08	0.05	96.01	16.06.2015
9	60	0.53	0.51	0.02	95.69	17.06.2015
10		0.54	0.51	0.02	95.65	17.06.2015

Table 37-Water / THF (30wt% / 70wt%) varying temperature (50-70°C) study, 1 µm membrane

Entry	Temperature (°C)	Total (kg h^{-1}m^{-2})	Water (kg h^{-1}m^{-2})	IPA (kg h^{-1}m^{-2})	Permeate (wt%)	Date
1	60	1.61	1.573614	0.036386	97.74	09.04.2014
2		1.86	1.80606	0.05394	97.1	09.04.2014
3		1.83	1.78608	0.04392	97.6	09.04.2014
4		1.82	1.77996	0.04004	97.8	09.04.2014
5	50	1.12	1.1088	0.0112	99	09.04.2014
6		0.98	0.96138	0.01862	98.1	09.04.2014
7		1	0.992	0.008	99.2	09.04.2014
8		0.9	0.8928	0.0072	99.2	09.04.2014
9	70	2.96	2.92744	0.03256	98.9	09.04.2014
10		2.72	2.69552	0.02448	99.1	09.04.2014
11		2.9	2.8797	0.0203	99.3	09.04.2014

Table 38-Water/IPA (30-5wt%) permeation study, 2.1µm, 50°C

Entry	Time	Cumulative Time	Total ($kg\ h^{-1}m^{-2}$)	Water ($kg\ h^{-1}m^{-2}$)	IPA ($kg\ h^{-1}m^{-2}$)	Permeate (wt%)	Measured Water (wt%)	Date
1	3h23min	5h25min	0.64	0.64	0.00	99.40	0.293	08.05.2014
2	3h05min	8h30min	0.65	0.64	0.00	99.40	0.283	08.05.2014
3	15h11min	23h41min	0.61	0.61	0.00	99.80	0.25	08.05.2014
4	8h25min	32h06min	0.55	0.54	0.01	98.50	0.228	08.05.2014
5	15h25min	47h34min	0.49	0.49	0.00	99.90	0.194	08.05.2014
6	7h58min	55h32min	0.41	0.41	0.00	99.50	0.176	08.05.2014
7	21h11min	76h43min	0.32	0.32	0.00	99.80	0.141	08.05.2014
8	22h34min	99h17min	0.23	0.23	0.00	99.60	0.11	08.05.2014
9	23h30min	122h47min	0.15	0.15	0.00	99.40	0.086	08.05.2014
10	26h37min	149h24min	0.10	0.10	0.00	99.60	0.066	08.05.2014
11	42h29min	191h53min	0.06	0.05	0.00	99.50	0.047	08.05.2014

Table 39-Water/IPA (12.5-8wt%) permeation study, 2.1µm, 50°C

Entry	Time	Cumulative Time	Total ($kg\ h^{-1}m^{-2}$)	Water ($kg\ h^{-1}m^{-2}$)	IPA ($kg\ h^{-1}m^{-2}$)	Permeate (wt%)	Measured Water (wt%)	Date
1	4h15min	5h35min	0.29	0.29	0.00	98.60	0.117583396	30.03.2015
2	15h05min	20h40min	0.23	0.23	0.00	98.60	0.099691733	30.03.2015
3	6h30min	27h10min	0.16	0.16	0.00	98.60	0.09417958	30.03.2015
4	18h03min	45h13min	0.12	0.12	0.00	98.60	0.082235557	30.03.2015

Table 40-Water/IPA (5-4wt%, and 1wt%) permeation study, 2.1µm, 50°C

Entry	Time	Cumulative Time	Total (kg h^{-1}m^{-2})	Water (kg h^{-1}m^{-2})	IPA (kg h^{-1}m^{-2})	Permeate (wt%)	Measured Water (wt%)	Date
1	21h27min	23h01min	0.04	0.03	0.00	96.00	0.047	14.04.2015
2	50h05min	73h06min	0.03	0.03	0.00	95.80	0.04	14.04.2015
3	6h30min	79h36min	0.01	0.01	0.00	98.60	0.0376	14.04.2015
4	72h54min	72h54min	0.00174	0.00154	0.00020	88.60	0.01	20.02.2015

Table 41-Water/IPA (30 / 70wt%) Liquid side mass transfer coefficient study1, 2.1µm, 50°C

Stirring (rev min^{-1})	Total (kg h^{-1}m^{-2})	Water (kg h^{-1}m^{-2})	IPA (kg h^{-1}m^{-2})	Permeate (wt%)	Date
0	0.116	0.116	0.000	99.60	18.02.2014
250	0.281	0.281	0.000	99.90	18.02.2014
500	0.754	0.750	0.004	99.50	18.02.2014
750	0.796	0.790	0.006	99.30	18.02.2014
960	0.900	0.899	0.001	99.90	18.02.2014

Table 42-Water/IPA (30 / 70wt%) Liquid side mass transfer coefficient study2, 2.1µm, 50°C

Stirring (rev min^{-1})	Total (kg h^{-1}m^{-2})	Water (kg h^{-1}m^{-2})	IPA (kg h^{-1}m^{-2})	Permeate (wt%)	Date
0	0.185	0.181	0.004	98.00	18.02.2014
250	0.445	0.439	0.006	98.60	18.02.2014
500	0.800	0.768	0.032	96.00	18.02.2014
750	0.845	0.769	0.076	91.00	18.02.2014
960	0.672	0.665	0.007	99.00	18.02.2014

Table 43-Water/IPA (30 / 70wt%) Liquid side mass transfer coefficient study3, 2.1μm, 50°C

Stirring (rev min^{-1})	Total (kg h^{-1}m^{-2})	Water (kg h^{-1}m^{-2})	IPA (kg h^{-1}m^{-2})	Permeate (wt%)	Date
0	0.177	0.177	0.000	99.90	18.02.2014
250	0.560	0.553	0.007	98.68	18.02.2014
500	0.650	0.637	0.013	97.96	18.02.2014
750	0.630	0.617	0.013	98.00	18.02.2014
960	0.687	0.681	0.006	99.13	18.02.2014

Table 44-MeOH / n-Hexane pervaporation study, 2.1µm

Entry	MeOH (wt%)	n-Hexane (wt%)	Temperature (°C)	Total (kg h^{-1}m^{-2})	MeOH (kg h^{-1}m^{-2})	n-Hexane (kg h^{-1}m^{-2})	Permeate (wt%)	Date
1	55	45		0.370	0.367	0.003	99.26	24.09.2014
2	15	85		0.274	0.274	0.000	99.83	25.09.2014
3	10	90		0.220	0.218	0.002	99.2	02.10.2014
4	55	45		0.560	0.559	0.001	99.8	02.02.2015
5	10	90	60	0.150	0.149	0.001	99.1	17.02.2015
6	4	96		0.084	0.082	0.002	98.2	18.02.2015
7	60	40		0.330	0.327	0.003	99	19.02.2015
8	10	90		0.118	0.117	0.001	99.2	11.05.2015
9	10	90		0.400	0.397	0.003	99.2	11.05.2015
10	10	90		0.144	0.135	0.009	94	20.02.2015
11	10	90		0.090	0.084	0.006	93	24.02.2015
12	10	90		0.095	0.089	0.006	94	25.02.2015
13	10	90		1.000	1.000	0.000	100	11.05.2015
14	10	90		0.700	0.698	0.002	99.78	11.05.2015
15	10	90	70	0.480	0.476	0.004	99.2	11.05.2015
16	10	90		0.310	0.302	0.008	97.45	11.05.2015
17	10	90		0.400	0.387	0.013	96.7	11.05.2015
18	45	55		0.500	0.500	0.000	99.9	13.05.2015
19	45	55		0.530	0.526	0.004	99.2	13.05.2015
20	10	90	80	0.150	0.140	0.011	93	23.02.2015

Table 45-IPA and carboxylic acid esterification study1, 100°C, 2.1µm, 03.02.2015

Entry	Sampling Time	Cumulative Time	Acid Value	Conversion
1	0h00min	0h00min	4.87	0.00
2	1h13min	1h13min	4.23	13.14
3	2h23min	2h23min	3.53	27.52
4	3h37min	3h37min	2.83	41.89
5	5h30min	5h30min	2.17	55.44
6	1h32min	7h02min	1.75	64.07
7	2h30min	8h00min	1.62	66.74
8	3h53min	9h23min	1.5	69.20
9	5h22min	10h52min	1.38	71.66
10	6h06min	11h36min	1.33	72.69
11	1h29min	13h05min	1.24	74.54
12	2h35min	14h11min	1.22	74.95
13	4h23min	15h59min	1.16	76.18

Table 46-IPA and carboxylic acid esterification study2, 100°C, 2.1µm, 06.02.2015

Entry	Sampling Time	Cumulative Time	Acid Value	Conversion
1	0h00min	0h00min	4.9	0.00
2	1h20min	1h20min	4.27	12.86
3	2h31min	2h31min	3.51	28.37
4	3h33min	3h33min	3.08	37.14
5	5h18min	5h18min	2.64	46.12
6	1h43min	7h43min	2.1	57.14
7	3h00min	8h00min	1.86	62.04
8	4h41min	9h59min	1.71	65.10
9	6h30min	11h48min	1.68	65.71
10	1h51min	13h39min	1.56	68.16
11	4h16min	16h4min	1.5	69.39
12	5h46min	17h34min	1.43	70.82
13	6h48min	18h36min	1.49	69.59

Table 47-IPA and carboxylic acid esterification study3, 100°C, 2.1µm, 11.02.2015

Entry	Sampling Time	Cumulative Time	Acid Value	Conversion
1	0h00min	0h00min	4.95	0.00
2	1h18min	1h18min	4.28	13.54
3	2h44min	2h44min	3.36	32.12
4	3h51min	3h51min	2.99	39.60
5	4h42min	4h42min	2.82	43.03
6	6h00min	6h00min	2.72	45.05
7	1h19min	7h19min	2.42	51.11
8	2h04min	8h04min	2.39	51.72
9	3h47min	9h47min	2.26	54.34
10	4h55min	10h55min	2.14	56.77
11	6h56min	12h56min	2.08	57.98
12	1h17min	14h13min	2.13	56.97
13	2h58min	15h54min	2.06	58.38
14	4h15min	17h11min	2.03	58.99

Table 48-Peptide 2 peptide dewatering study (5wt% solids), 80°C, 2.1µm

Entry	Sample Time	Total Time	Fux (kg h^{-1}m^{-2})	Date
1	1h05min	1h05min	5.82	16.12.2014
2	1h09min	2h14min	4.60	16.12.2015
3	1h20min	3h34min	4.60	16.12.2016
4	2h05min	5h39min	4.66	16.12.2017
5	1h18min	6h57min	4.16	17.12.2014
6	1h07min	8h49min	4.50	17.12.2014
7	1h34min	10h23min	4.55	17.12.2014
8	1h30min	11h53min	4.14	17.12.2014
9	1h25min	13h18min	4.10	17.12.2014
10	1h12min	14h30min	4.00	18.12.2014
11	0h38min	15h08min	4.00	18.12.2014
12	1h01min	16h09min	3.94	18.12.2014
13	1h43min	17h52min	3.54	18.12.2014
14	2h06min	19h58min	3.00	19.12.2014
15	1h00min	20h58min	3.00	19.12.2014
16	1h33min	22h31min	2.90	19.12.2014
17	1h56min	24h27min	2.43	19.12.2014
18	1h42min	26h09min	2.32	19.12.2014

Table 49-Peptide 1 peptide dewatering study (2-8wt% solids), 80°C, 2.1µm

Entry	Solids (wt%)	Sample time	Total time	Fux (kg h^{-1}m^{-2})	Date
1	2	0h00min	0h00min	0.00	19.11.2014
2	2	1h05min	1h06min	4.29	19.11.2014
3	2	1h09min	2h016min	3.19	19.11.2014
4	2	1h20min	3h29min	2.85	19.11.2014
5	2	2h05min	5h06min	2.40	19.11.2014
6	2	1h18min	7h28min	2.60	20.11.2014
7	2	2h42min	10h00min	2.50	20.11.2014
8	2	1h07min	11h54min	2.18	21.11.2014
9	2	1h34min	13h16min	1.90	21.11.2014
10	4	1h30min	14h35min	1.77	21.11.2014
11	4	1h25min	16h19min	1.71	24.11.2014
12	4	0h38min	19h15min	1.34	24.11.2014
13	8	1h01min	20h52min	1.17	25.11.2014
14	8	1h43min	22h40min	1.00	26.11.2014
15	8	2h06min	24h11min	0.90	26.11.2014
16	8	1h33min	26h50min	0.70	26.11.2014
17	8	1h56min	28h17min	0.59	26.11.2014
18	8	1h42min	29h39min	0.44	26.11.2014
19	8	2h02min	31h41min	0.33	27.11.2014
20	8	2h17min	33h58min	0.17	27.11.2014

Table 50-Peptide 3 peptide dewatering study (2wt% solids), 70°C, 2.1μm, 07.01.2015

Entry	Sample time	Total time	Fux (kg h^{-1}m^{-2})
1	0h00min	0h00min	0
2	1h21min	1h21min	1.04
3	1h23min	2h44min	0.83
4	2h09min	4h53min	0.76
5	1h05min	5h58min	0.68
6	2h07min	7h20min	0.52
7	2h15min	9h27min	0.74
8	3h15min	12h42min	0.59
9	1h05min	13h47min	0.52
10	2h13min	16h01min	0.62
11	0h51min	16h52min	0.52
12	2h51min	18h52min	0.61

9.2 Appendix B Detailed Distillation Process Information

Column 1	
Total number of stages	20 (including condenser and reboiler)
IPA/Water Feed stage	16
IPA/Water Feed Flowrate (kg/h)	1000
IPA/Water Feed Composition (wt%)	70 (IPA) , 30 (H_2O)
DMSO Feed Stage	3
DMSOP Feed Flowrate (kg/h)	289.4
Distillate Flowrate (kg/h)	736.84
Distillate Composition (wt%)	94.99 (IPA), 4.97 (H_2O), 0.03 (DMSO)
Bottom Product Flowrate (kg/h)	552.56
Bottom Product Composition (wt%)	52.34 (DMSO), 47.65 (H_2O), 0.00 (IPA)
Molar Reflux Ratio	1.088
Reboiler Duty	340.00kW
Condenser Duty	-322.6 kW
C1HE1	
Inlet Hot (°C)	190.7
Outlet Hot (°C)	152.5
Inlet Cold (°C)	25
Outlet Cold (°C)	72
Heat Recovered (kW)	7.1
C1HE2	
Inlet Hot (K)	200
Outlet Hot (K)	108.245
Inlet Cold (K)	25
Outlet Cold (K)	72
Heat Recovered (kW)	48.82
Column 2	
Total number of stages	10 (including condenser and reboiler)
Feed stage	4
Feed Flowrate (kg/h)	552.56
Feed Composition (wt%)	52.34 (DMSO), 47.65 (H_2O), 0.00 (IPA)
Distillate Flowrate (kg/h)	263.32
Distillate Composition (wt%)	99.99 (H_2O), 0.01 (DMSO)
Bottom Product Flowrate (kg/h)	289.21
Bottom Product Composition (wt%)	99.99 (DMSO), 0.01 (H_2O)
Molar Reflux Ratio	0.3205
Reboiler Duty (kW)	218.80
Condenser Duty (kW)	- 239.74

9.3 Appendix C Detailed Pervaporation Cell Drawings
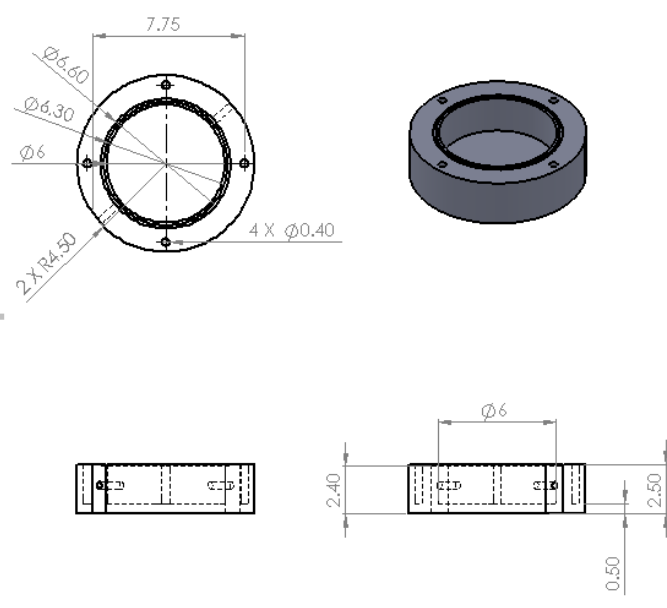
Figure 69-Pervaporation cell process side drawing
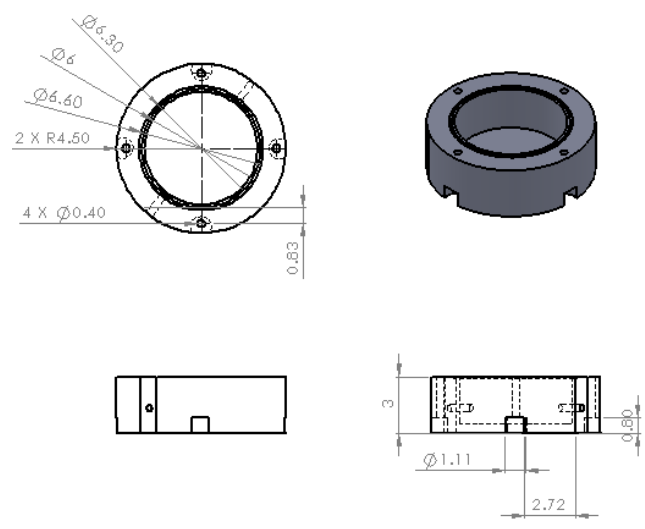
Figure 70 – Pervaporation cell process side drawing
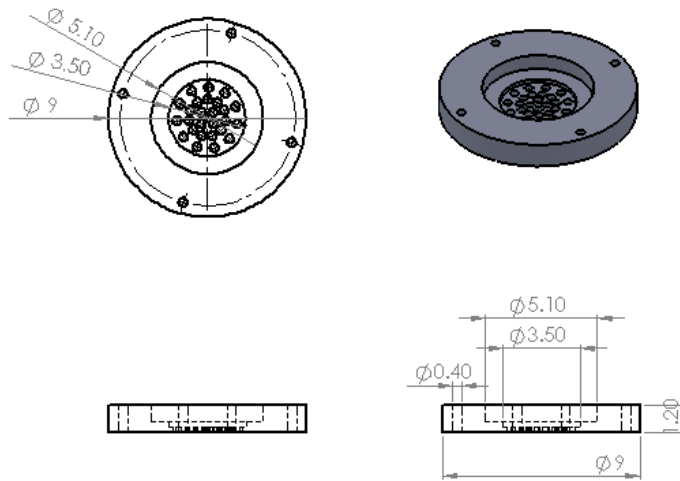
Figure 71 - Pervaporation cell membrane saddle drawing
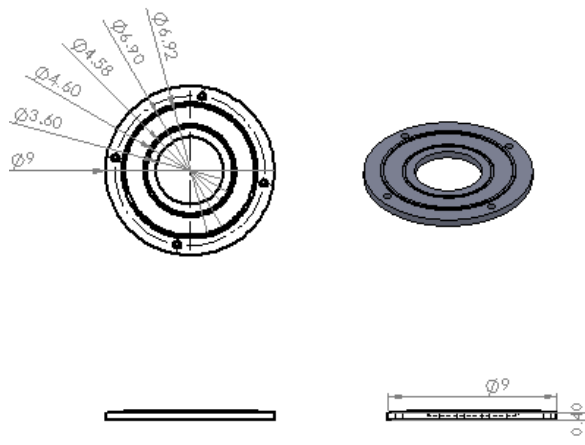
Figure 72 - Pervaporation cell membrane saddle drawing
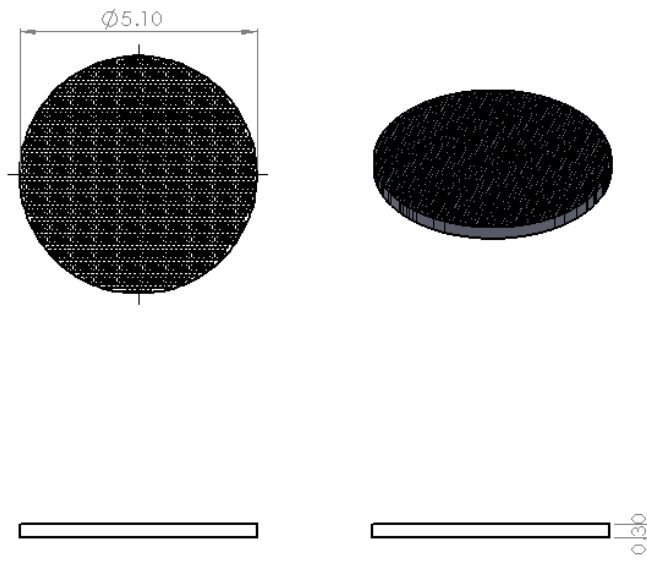
Figure 73-Porous stainless steel support drawing
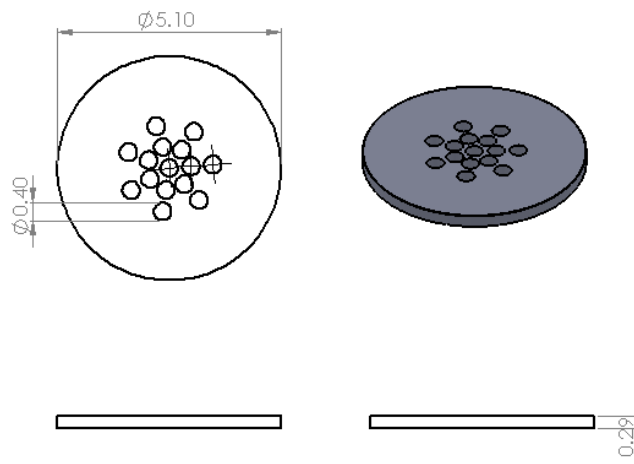
Figure 74 –Stainless steel support drawing
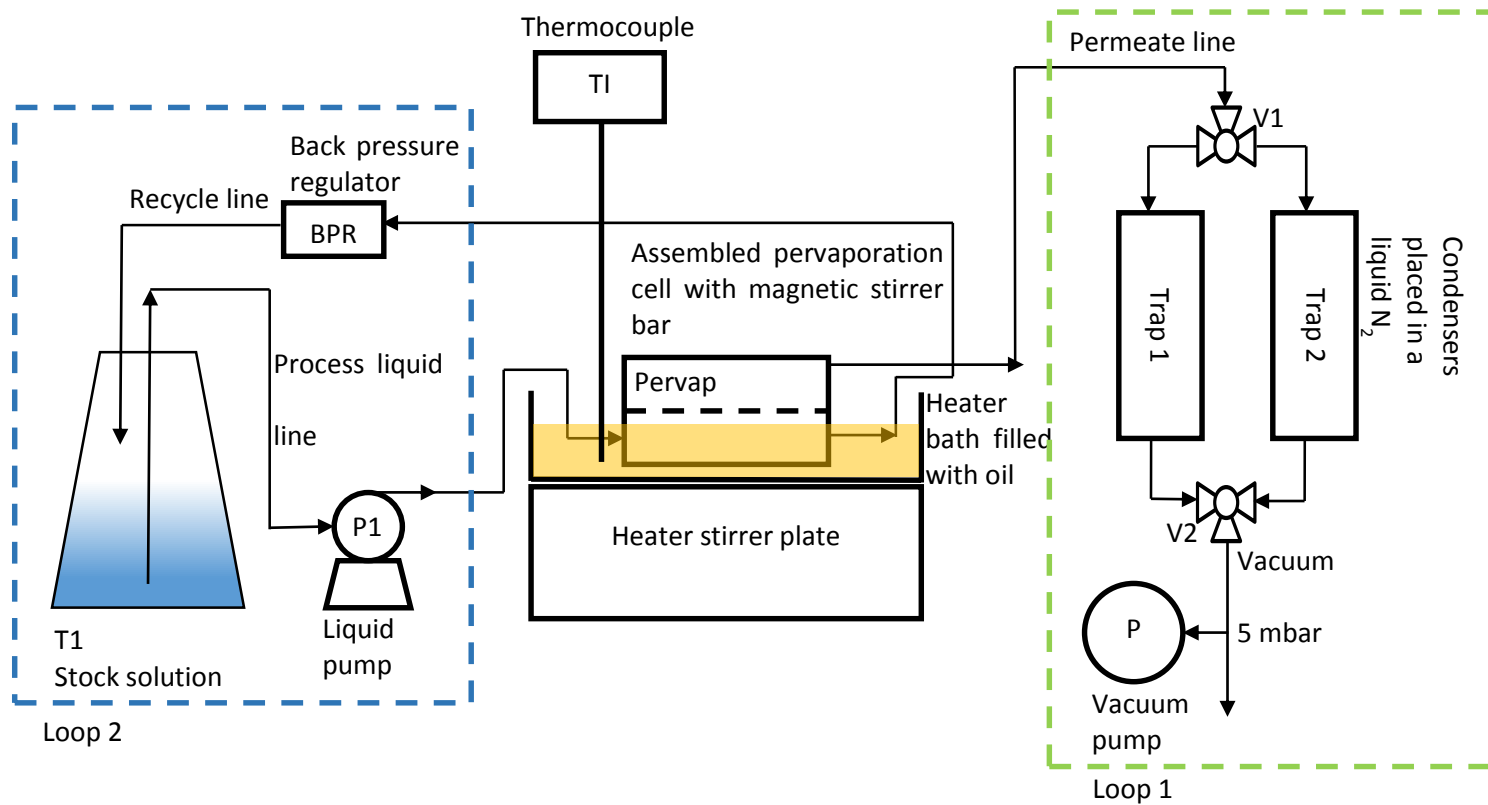
Start up

Loop 1

1. Ensure that valve 1 (V1) and valve 2 (V2) are completely closed.
2. Turn on the vacuum pump (P2), and wait until the operating line is under vacuum
3. Open the desired operating line using a three way valve (valve 2); wait until the line is under vacuum.
4. Initiate the remainder of the line by operating a three way valve (valve 1); wait until the line is under vacuum. At this stage the desired operating line is under vacuum conditions
5. Proceed to the "Loop 2"

Loop 2

1. Close pervaporation cell's outlet and inlet. Wait for 10 minutes and measure the pressure inside the pervaporation cell's process side. A significant drop in pressure indicates either a flaw on a membrane surface or incorrectly fitted membrane. Resolve the pressure drop before proceeding further.
2. Load the conical flask (T1) with desired amount and composition liquid
3. Switch on the pump (P1) and fill the pervaporation cell
4. Place the pervaporation cell in a hot oil bath located on a heater stirrer plate.
5. Initiate stirring on a heater stirrer plate
6. Lower the cold finger connected to a vacuum line into a liquid nitrogen dewar

Sampling

1. Isolate the cold finger submerged into a liquid nitrogen using V1 and V2. Lift it out of the drawer
2. Initiate vacuum on the parallel line by operating V1 and V2. Wait until the pressure gauge indicates that the line is under vacuum.
3. Lower the cold finger into the liquid nitrogen dewar
4. Wait until the sample is in a liquid phase in the cold finger and then extract it using a syringe and a needle
5. Weight and analyse the sample

Shutdown

1. Close both three way valves (V 1 and V 2)
2. Ensure both cold fingers are lifted up and are not in contact with the liquid nitrogen
3. Stop the vacuum pump (P2)
4. Stop the liquid pump (P1)
5. Lift the pervaporation cell out of the oil bath and drain the liquid from the inside
6. Ensure all electrical appliances are switched off

Notes

1. The direction of the arrow on a three way valve indicates the direction of the flow.
2. When the arrow is not pointing to either of the sides the valve is in its closed position
3. Ensure pump has upper and lower pressure cut off limits set
4. The back pressure regulator rating must not be lower than the lowest pressure limit or higher than the highest pressure limit. If these conditions are not met pump will not operate
5. Check both cold fingers for any chips and cracks before operating the apparatus

10 Reference

1.   Nair, R.R., et al., *Unimpeded Permeation of Water Through Helium-Leak–Tight Graphene-Based Membranes.* Science, 2012. **335**(6067): p. 442-444.

2.   Wijmans, J.G. and R.W. Baker, *The solution-diffusion model: a review.* J. Membr. Sci., 1995. **107**: p. 1-21.

3.   Wei, N., X. Peng, and Z. Xu, *Understanding Water Permeation in Graphene Oxide Membranes.* ACS Applied Materials & Interfaces, 2014. **6**(8): p. 5877-5883.

4.   Höök, M. and X. Tang, *Depletion of fossil fuels and anthropogenic climate change—A review.* Energy Policy, 2013. **52**(0): p. 797-809.

5.   Durbin, J., *A 'whole building' path to climate control.* Health Estate, 2010. **64**: p. 71-3.

6.   Babi, D.K., et al., *Sustainable process synthesis–intensification.* Computers & Chemical Engineering, (0).

7.   Van Gerven, T. and A. Stankiewicz, *Structure, Energy, Synergy, Time—The Fundamentals of Process Intensification.* Industrial & Engineering Chemistry Research, 2009. **48**(5): p. 2465-2474.

8.   Servel, C., et al., *Improved Energy Efficiency of a Hybrid Pervaporation/Distillation Process for Acetic Acid Production: Identification of Target Membrane Performances by Simulation.* Industrial & Engineering Chemistry Research, 2014.

9.   Commissions, E., *Membrane technologies for water applications*, in *Highlights from a selection of European research projects.* 2010.

10. Diban, N., et al., *Membrane Reactors for in Situ Water Removal: A Review of Applications.* Industrial & Engineering Chemistry Research, 2013. **52**(31): p. 10342-10354.

11. Baker, R.W., *Membrane Technology and Applications.* 2012: Wiley.

12. Joo, S.H. and B. Tansel, *Novel technologies for reverse osmosis concentrate treatment: A review.* Journal of Environmental Management, 2015. **150**: p. 322-335.

13. Mahdi, T., et al., *State-of-the-Art Technologies for Separation of Azeotropic Mixtures.* Separation & Purification Reviews, 2014. **44**(4): p. 308-330.

14. Chapman, P.D., et al., *Membranes for the dehydration of solvents by pervaporation.* Journal of Membrane Science, 2008. **318**(1–2): p. 5-37.

15. Zhao, J., et al., *Fabricating graphene oxide-based ultrathin hybrid membrane for pervaporation dehydration via layer-by-layer self-assembly driven by multiple interactions.* Journal of Membrane Science, 2015. **487**(Copyright (C) 2015 American Chemical Society (ACS). All Rights Reserved.): p. 162-172.

16. Nair, R., P. Budd, and A. Geim, *Separation of water using a membrane.* 2014, Google Patents.

17. Tang, Y.P., D.R. Paul, and T.S. Chung, *Free-standing graphene oxide thin films assembled by a pressurized ultrafiltration method for dehydration of ethanol.* Journal of Membrane Science, 2014. **458**(0): p. 199-208.

18. Shao, P. and R.Y.M. Huang, *Polymeric membrane pervaporation.* Journal of Membrane Science, 2007. **287**(2): p. 162-179.

19. Smitha, B., et al., *Separation of organic–organic mixtures by pervaporation—a review.* Journal of Membrane Science, 2004. **241**(1): p. 1-21.

20. Guo, W.F., T.-S. Chung, and T. Matsuura, *Pervaporation study on the dehydration of aqueous butanol solutions: a comparison of flux vs. permeance, separation factor vs. selectivity.* Journal of Membrane Science, 2004. **245**(1–2): p. 199-210.

21. Kanti, P., et al., *Dehydration of ethanol through blend membranes of chitosan and sodium alginate by pervaporation.* Separation and Purification Technology, 2004. **40**(3): p. 259-266.

22. Sander, U. and P. Soukup, *Design and operation of a pervaporation plant for ethanol dehydration.* J. Membr. Sci., 1988. **36**(Copyright (C) 2012 American Chemical Society (ACS). All Rights Reserved.): p. 463-75.

23. Bolto, B., M. Hoang, and Z. Xie, *A review of membrane selection for the dehydration of aqueous ethanol by pervaporation.* Chem. Eng. Process., 2011. **50**: p. 227-235.

24. Zhang, L., et al., *Ion exchange membranes blended by cellulose cuoxam with alginate.* Journal of Membrane Science, 1997. **124**(2): p. 195-201.

25. Yeom, C.K. and K.H. Lee, *Vapor permeation of ethanol-water mixtures using sodium alginate membranes with crosslinking gradient structure.* Journal of Membrane Science, 1997. **135**(2): p. 225-235.

26. Yang, G., et al., *Effects of Ca2+ bridge cross-linking on structure and pervaporation of cellulose/alginate blend membranes.* Journal of Membrane Science, 2000. **175**(1): p. 53-60.

27. Gimenes, M.L., L. Liu, and X. Feng, *Sericin/poly(vinyl alcohol) blend membranes for pervaporation separation of ethanol/water mixtures.* Journal of Membrane Science, 2007. **295**(1–2): p. 71-79.

28. Am, E.D.J. and Editor, *Chemical Engineering In The Pharmaceutical Industry: R & D To Manufacturing.* 2011: John Wiley & Sons, Inc. 887 pp.

29. See Toh, Y.H., F.W. Lim, and A.G. Livingston, *Polymeric membranes for nanofiltration in polar aprotic solvents.* Journal of Membrane Science, 2007. **301**(1–2): p. 3-10.

30. Verkerk, A.W., et al., *Properties of high flux ceramic pervaporation membranes for dehydration of alcohol/water mixtures.* Separation and Purification Technology, 2001. **22–23**(0): p. 689-695.

31. Svang-Ariyaskul, A., et al., *Blended chitosan and polyvinyl alcohol membranes for the pervaporation dehydration of isopropanol.* Journal of Membrane Science, 2006. **280**(1–2): p. 815-823.

32. Huang, R.Y.M. and Editor, *Membrane Science and Technology Series, 1: Pervaporation Membrane Separation Processes.* 1991: Elsevier. 549 pp.

33. Ge, J., et al., *The effect of structure on pervaporation of chitosan membrane.* Journal of Membrane Science, 2000. **165**(1): p. 75-81.

34. Huang, Z., et al., *Pervaporation study of aqueous ethanol solution through zeolite-incorporated multilayer poly(vinyl alcohol) membranes: Effect of zeolites.* Journal of Membrane Science, 2006. **276**(1–2): p. 260-271.

35. Lee, K.-R., R.-Y. Chen, and J.-Y. Lai, *Plasma deposition of vinyl acetate onto Nylon-4 membrane for pervaporation and evapomeation separation of aqueous alcohol mixtures.* Journal of Membrane Science, 1992. **75**(1–2): p. 171-180.

36.   Yeom, C.K. and K.H. Lee, *Characterization of sodium alginate and poly(vinyl alcohol) blend membranes in pervaporation separation.* Journal of Applied Polymer Science, 1998. **67**(5): p. 949-959.

37.   Bettens, B., et al., *Transport of Pure Components in Pervaporation through a Microporous Silica Membrane.* The Journal of Physical Chemistry B, 2005. **109**(11): p. 5216-5222.

38.   Yu, J., et al., *Method for producing hollow molecular sieve fiber having microporous-mesoporous-macroporous structure by coaxial spinning.* 2008, Jilin University, Peop. Rep. China . p. 20pp.

39.   Verkerk, A.W., et al., *Description of dehydration performance of amorphous silica pervaporation membranes.* Journal of Membrane Science, 2001. **193**(2): p. 227-238.

40.   Sommer, S. and T. Melin, *Influence of operation parameters on the separation of mixtures by pervaporation and vapor permeation with inorganic membranes. Part 1: Dehydration of solvents.* Chemical Engineering Science, 2005. **60**(16): p. 4509-4523.

41.   van Gemert, R.W. and F. Petrus Cuperus, *Newly developed ceramic membranes for dehydration and separation of organic mixtures by pervaporation.* Journal of Membrane Science, 1995. **105**(3): p. 287-291.

42.   Sekulić, J., et al., *Microporous silica and doped silica membrane for alcohol dehydration by pervaporation.* Desalination, 2002. **148**(1–3): p. 19-23.

43.   Okamoto, K.-i., H. Kita, and K. Horii, *Zeolite NaA Membrane: Preparation, Single-Gas Permeation, and Pervaporation and Vapor Permeation of Water/Organic Liquid Mixtures.* Industrial & Engineering Chemistry Research, 2000. **40**(1): p. 163-175.

44.   Kondo, M., et al., *Tubular-type pervaporation module with zeolite NaA membrane.* Journal of Membrane Science, 1997. **133**(1): p. 133-141.

45.   Hasegawa, Y., et al., *Influence of acid on the permeation properties of NaA-type zeolite membranes.* Journal of Membrane Science, 2010. **349**(1–2): p. 189-194.

46.   van Veen, H.M., et al., *Pushing membrane stability boundaries with HybSi® pervaporation membranes.* Journal of Membrane Science, 2011. **380**(1–2): p. 124-131.

47.   Agirre, I., et al., *Acetalization reaction of ethanol with butyraldehyde coupled with pervaporation. Semi-batch pervaporation studies and resistance of HybSi® membranes to catalyst impacts.* Journal of Membrane Science, 2011. **371**(1–2): p. 179-188.

48.   Liu, G., et al., *Polymer/Ceramic Composite Membranes and Their Application in Pervaporation Process.* Chin. J. Chem. Eng., 2012. **20**(1): p. 62-70.

49.   Gao, Z., Y. Yue, and W. Li, *Application of zeolite-filled pervaporation membrane.* Zeolites, 1996. **16**(1): p. 70-74.

50.   Zhang, Q.G., et al., *Dehydration of Isopropanol by Novel Poly(vinyl alcohol)−Silicone Hybrid Membranes.* Industrial & Engineering Chemistry Research, 2007. **46**(3): p. 913-920.

51.   Kariduraganavar, M.Y., et al., *Organic−Inorganic Hybrid Membranes: Solving the Trade-off Phenomenon Between Permeation Flux and Selectivity in Pervaporation.* Industrial & Engineering Chemistry Research, 2009. **48**(8): p. 4002-4013.

52. Uragami, T., et al., *Structure and Permeation Characteristics of an Aqueous Ethanol Solution of Organic−Inorganic Hybrid Membranes Composed of Poly(vinyl alcohol) and Tetraethoxysilane.* Macromolecules, 2002. **35**(24): p. 9156-9163.

53. White, L.S., *Development of large-scale applications in organic solvent nanofiltration and pervaporation for chemical and refining processes.* Journal of Membrane Science, 2006. **286**(1–2): p. 26-35.

54. Morigami, Y., et al., *The first large-scale pervaporation plant using tubular-type module with zeolite NaA membrane.* Separation and Purification Technology, 2001. **25**(1–3): p. 251-260.

55. Hasanoglu, A., et al., *The esterification of acetic acid with ethanol in a pervaporation membrane reactor.* Desalination, 2009. **245**: p. 662-669.

56. Waldburger, R.M. and F. Widmer, *Membrane reactors in chemical production processes and the application to the pervaporation-assisted esterification.* Chemical Engineering & Technology, 1996. **19**(2): p. 117-126.

57. Dreyer, D.R., et al., *The chemistry of graphene oxide.* Chemical Society Reviews, 2010. **39**(1): p. 228-240.

58. Huang, H., Y. Ying, and X. Peng, *Graphene oxide nanosheet: an emerging star material for novel separation membranes.* Journal of Materials Chemistry A, 2014. **2**(34): p. 13772-13782.

59. He, H., et al., *Solid-State NMR Studies of the Structure of Graphite Oxide.* The Journal of Physical Chemistry, 1996. **100**(51): p. 19954-19958.

60. Szabó, T., et al., *Evolution of Surface Functional Groups in a Series of Progressively Oxidized Graphite Oxides.* Chemistry of Materials, 2006. **18**(11): p. 2740-2749.

61. Dikin, D.A., et al., *Preparation and characterization of graphene oxide paper.* Nature, 2007. **448**(7152): p. 457-460.

62. Paredes, J.I., et al., *Graphene Oxide Dispersions in Organic Solvents.* Langmuir, 2008. **24**(19): p. 10560-10564.

63. Talyzin, A.V., et al., *The structure of graphene oxide membranes in liquid water, ethanol and water-ethanol mixtures.* Nanoscale, 2014. **6**(1): p. 272-281.

64. Huang, H., et al., *Ultrafast viscous water flow through nanostrand-channelled graphene oxide membranes.* Nat Commun, 2013. **4**.

65. Dong, Z., et al., *High performance ceramic hollow fiber supported PDMS composite pervaporation membrane for bio-butanol recovery.* Journal of Membrane Science, 2014. **450**(0): p. 38-47.

66. Brodie, B.C., *On the Atomic Weight of Graphite.* Philosophical Transactions of the Royal Society of London, 1859. **149**: p. 249-259.

67. Hummers, W.S. and R.E. Offeman, *Preparation of Graphitic Oxide.* Journal of the American Chemical Society, 1958. **80**(6): p. 1339-1339.

68. Marcano, D.C., et al., *Improved Synthesis of Graphene Oxide.* ACS Nano, 2010. **4**(8): p. 4806-4814.

69. Chen, J., et al., *An improved Hummers method for eco-friendly synthesis of graphene oxide.* Carbon, 2013. **64**(0): p. 225-229.

70. Berg, D. and L.C. Flowers, *Graphitic oxide memberane for desalinating water.* 1969, Google Patents.

71.   Yeh, T.-M., et al. *High flux ethanol dehydration using multilayered graphene oxide membranes.* 2013. American Chemical Society.

72.   Yeh, T.-M., et al., *Polymeric nanofibrous composite membranes for energy efficient ethanol dehydration.* J. Renewable Sustainable Energy, 2012. **4**: p. 041406/1-041406/9.

73.   Liu, R., et al., *Graphene oxide membrane for liquid phase organic molecular separation.* Carbon, 2014. **77**(0): p. 933-938.

74.   Tang, Y., et al., *Development of flat-sheet membranes for C1–C4 alcohols dehydration via pervaporation from sulfonated polyphenylsulfone (sPPSU).* Journal of Membrane Science, 2012. **415–416**(0): p. 686-695.

75.   Huang, K., et al., *A Graphene Oxide Membrane with Highly Selective Molecular Separation of Aqueous Organic Solution.* Angewandte Chemie International Edition, 2014. **53**(27): p. 6929-6932.

76.   Qiao, X., et al., *Dehydration of isopropanol and its comparison with dehydration of butanol isomers from thermodynamic and molecular aspects.* Journal of Membrane Science, 2005. **252**(1–2): p. 37-49.

77.   Okada, T. and T. Matsuura, *A new transport model for pervaporation.* Journal of Membrane Science, 1991. **59**(2): p. 133-149.

78.   Sukitpaneenit, P., T.-S. Chung, and L.Y. Jiang, *Modified pore-flow model for pervaporation mass transport in PVDF hollow fiber membranes for ethanol–water separation.* Journal of Membrane Science, 2010. **362**(1–2): p. 393-406.

79.   Gilliland, E.R., R.F. Baddour, and J.L. Russell, *Rates of flow through microporous solids.* AIChE Journal, 1958. **4**(1): p. 90-96.

80.   Jia, Z. and Y. Wang, *Covalently crosslinked graphene oxide membranes by esterification reactions for ions separation.* Journal of Materials Chemistry A, 2015. **3**(8): p. 4405-4412.

81.   Okada, T., M. Yoshikawa, and T. Matsuura, *A study on the pervaporation of ethanol/water mixtures on the basis of pore flow model.* Journal of Membrane Science, 1991. **59**(2): p. 151-168.

82.   Wijmans, J.G. and R.W. Baker, *A simple predictive treatment of the permeation process in pervaporation.* Journal of Membrane Science, 1993. **79**(1): p. 101-113.

83.   Wijmans, J.G., et al., *The role of boundary layers in the removal of volatile organic compounds from water by pervaporation.* J. Membr. Sci., 1996. **109**: p. 135-46.

84.   Bridgeman, O.C. and E.W. Aldrich, *Vapor Pressure Tables for Water.* Journal of Heat Transfer, 1964. **86**(2): p. 279-286.

85.   Baker, R., *Membrane Technology and Applications, 2nd Edition.* 2004: John Wiley & Sons. 568 pp.

86.   Feng, X. and R.Y.M. Huang, *Concentration polarization in pervaporation separation processes.* Journal of Membrane Science, 1994. **92**(3): p. 201-208.

87.   Bhattacharya, S. and S.-T. Hwang, *Concentration polarization, separation factor, and Peclet number in membrane processes.* Journal of Membrane Science, 1997. **132**(1): p. 73-90.

88.   Nagy, E. and E. Kulcsar, *The effect of the concentration polarization and the membrane layer mass transport on membrane separation.* Desalin. Water Treat., 2010. **14**: p. 220-226.

89. Jaffrin, M.Y., B.B. Gupta, and P. Paullier, *Energy saving pulsatile mode cross flow filtration.* Journal of Membrane Science, 1994. **86**(3): p. 281-290.

90. Da Costa, A.R., A.G. Fane, and D.E. Wiley, *Spacer characterization and pressure drop modelling in spacer-filled channels for ultrafiltration.* Journal of Membrane Science, 1994. **87**(1–2): p. 79-98.

91. Nagy, E., *Coupled effect of the membrane properties and concentration polarization in pervaporation: unified mass transport model.* Separation and Purification Technology, 2010. **73**: p. 194-201.

92. Jiraratananon, R., A. Chanachai, and R.Y.M. Huang, *Pervaporation dehydration of ethanol–water mixtures with chitosan/hydroxyethylcellulose (CS/HEC) composite membranes: II. Analysis of mass transport.* Journal of Membrane Science, 2002. **199**(1–2): p. 211-222.

93. Schofield, R.W., A.G. Fane, and C.J.D. Fell, *Gas and vapour transport through microporous membranes. I. Knudsen-Poiseuille transition.* Journal of Membrane Science, 1990. **53**(1–2): p. 159-171.

94. Noworyta, A., M. Kubasiewicz-Ponitka, and A. Koziol, *Mass and heat transport resistance in pervaporation process.* Desalination and Water Treatment, 2011. **26**(1-3): p. 226-235.

95. Cavanagh, E.J., M.J. Savelski, and C.S. Slater, *Optimization of environmental impact reduction and economic feasibility of solvent waste recovery using a new software tool.* Chemical Engineering Research and Design, 2014. **92**(10): p. 1942-1954.

96. Baker, R.W., et al., *The effect of concentration polarization on the separation of volatile organic compounds from water by pervaporation.* Journal of Membrane Science, 1997. **137**(1–2): p. 159-172.

97. Taherian, F., et al., *What Is the Contact Angle of Water on Graphene?* Langmuir, 2013. **29**(5): p. 1457-1465.

98. Hao, L. and D.G. Leaist, *Binary Mutual Diffusion Coefficients of Aqueous Alcohols. Methanol to 1-Heptanol.* Journal of Chemical and Engineering Data, 1996. **41**(2): p. 210-213.

99. Li, H., et al., *Ultrathin, Molecular-Sieving Graphene Oxide Membranes for Selective Hydrogen Separation.* Science, 2013. **342**(6154): p. 95-98.

100. Yeh, T.-M., et al., *High Flux Ethanol Dehydration using Nanofibrous Membranes Containing Graphene Oxide Barrier Layer.* Journal of Materials Chemistry A, 2013.

101. Bayer, T., et al., *Characterization of a graphene oxide membrane fuel cell.* Journal of Power Sources, 2014. **272**: p. 239-247.

102. Shen, J., et al., *Fast and Facile Preparation of Graphene Oxide and Reduced Graphene Oxide Nanoplatelets.* Chem. Mater., 2009. **21**: p. 3514-3520.

103. Acik, M., et al., *The role of oxygen during thermal reduction of graphene oxide studied by infrared absorption spectroscopy.* The Journal of Physical Chemistry C, 2011. **115**(40): p. 19761-19781.

104. Bian, J., et al., *Processing and assessment of high-performance poly(butylene terephthalate) nanocomposites reinforced with microwave exfoliated graphite oxide nanosheets.* Eur. Polym. J., 2013. **49**: p. 1406-1423.

105. Kumarasinghe, A.R., et al., *Self-Assembled Multilayer Graphene Oxide Membrane and Carbon Nanotubes Synthesized Using a Rare Form of Natural Graphite.* J. Phys. Chem. C, 2013. **117**: p. 9507-9519.

106. Jeong, H.-K., et al., *Thermal stability of graphite oxide.* Chem. Phys. Lett., 2009. **470**: p. 255-258.

107. Gong, C., et al., *Graphitization of Graphene Oxide with Ethanol during Thermal Reduction.* The Journal of Physical Chemistry C, 2012. **116**(18): p. 9969-9979.

108. Wang, A.-X., et al., *Preparation and characterization of novel spica-like hierarchical vaterite calcium carbonate and a hydrophilic poly(vinylidene fluoride)/calcium carbonate composite membrane.* CrystEngComm, 2014. **16**(24): p. 5198-5205.

109. Rattana, et al., *Preparation and characterization of graphene oxide nanosheets.* Procedia Engineering, 2012. **32**(0): p. 759-764.

110. Szabó, T., et al., *Enhanced acidity and pH-dependent surface charge characterization of successively oxidized graphite oxides.* Carbon, 2006. **44**(3): p. 537-545.

111. Zuo, P.-P., et al., *Fabrication of biocompatible and mechanically reinforced graphene oxide-chitosan nanocomposite films.* Chemistry Central Journal, 2013. **7**(1): p. 39.

112. Deshmukh, K. and G.M. Joshi, *Novel nanocomposites of graphene oxide reinforced poly (3,4-ethylenedioxythiophene)-block-poly (ethylene glycol) and polyvinylidene fluoride for embedded capacitor applications.* RSC Advances, 2014. **4**(71): p. 37954-37963.

113. Han, Y.-J., et al., *Hydrophilic chitosan-modified polybenzoimidazole membranes for pervaporation dehydration of isopropanol aqueous solutions.* Journal of Membrane Science, 2014. **463**(0): p. 17-23.

114. Ganetsos, G. and P.E. Barker, *Large-scale chromatography in industrial processing.* Journal of Chemical Technology & Biotechnology, 1991. **50**(1): p. 101-108.

115. Pei, S., et al., *Direct reduction of graphene oxide films into highly conductive and flexible graphene films by hydrohalic acids.* Carbon, 2010. **48**(15): p. 4466-4474.

116. Peng, X., et al., *Zeolite membrane-assisted preparation of high fatty esters.* Separation and Purification Technology, 2012. **89**: p. 84-90.

117. Korkmaz, S., Y. Salt, and S. Dincer, *Esterification of Acetic Acid and Isobutanol in a Pervaporation Membrane Reactor Using Different Membranes.* Ind. Eng. Chem. Res., 2011. **50**: p. 11657-11666.

118. Paradis, G.G., et al., *From hydrophilic to hydrophobic HybSi® membranes: A change of affinity and applicability.* Journal of Membrane Science, 2013. **428**: p. 157-162.

119. Zinadini, S., et al., *Preparation of a novel antifouling mixed matrix PES membrane by embedding graphene oxide nanoplates.* Journal of Membrane Science, 2014. **453**: p. 292-301.

120. Chan, R. and V. Chen, *Characterization of protein fouling on membranes: opportunities and challenges.* Journal of Membrane Science, 2004. **242**(1–2): p. 169-188.

121. Makardij, A., X.D. Chen, and M.M. Farid, *Microfiltration and Ultrafiltration of Milk: Some Aspects of Fouling and Cleaning.* Food and Bioproducts Processing, 1999. **77**(2): p. 107-113.

122. Fan, X., et al., *Deoxygenation of exfoliated graphite oxide under alkaline conditions: a green route to graphene preparation.* Advanced Materials, 2008. **20**(23): p. 4490-4493.

123. Sommer, S. and T. Melin, *Design and Optimization of Hybrid Separation Processes for the Dehydration of 2-Propanol and Other Organics.* Industrial & Engineering Chemistry Research, 2004. **43**(17): p. 5248-5259.

124. Rodriguez, N.R. and M.C. Kroon, *Isopropanol dehydration via extractive distillation using low transition temperature mixtures as entrainers.* The Journal of Chemical Thermodynamics, 2015. **85**: p. 216-221.

125. Brunjes, A.S. and M.J.P. Bogart, *Vapor-Liquid Equilibria for Commercially Important Systems of Organic Solvents: The Binary Systems Ethanol-n-Butanol, Acetone-Water and Isopropanol-Water.* Industrial & Engineering Chemistry, 1943. **35**(2): p. 255-260.

126. Rodríguez-Donis, I., V. Gerbaud, and X. Joulia, *Entrainer Selection Rules for the Separation of Azeotropic and Close-Boiling-Temperature Mixtures by Homogeneous Batch Distillation Process.* Industrial & Engineering Chemistry Research, 2001. **40**(12): p. 2729-2741.

127. Arifin, S. and I.L. Chien, *Design and Control of an Isopropyl Alcohol Dehydration Process via Extractive Distillation Using Dimethyl Sulfoxide as an Entrainer.* Industrial & Engineering Chemistry Research, 2008. **47**(3): p. 790-803.

128. Gmehling, J. and C. Möllmann, *Synthesis of Distillation Processes Using Thermodynamic Models and the Dortmund Data Bank.* Industrial & Engineering Chemistry Research, 1998. **37**(8): p. 3112-3123.

129. Chien, I.L., K.-L. Zeng, and H.-Y. Chao, *Design and Control of a Complete Heterogeneous Azeotropic Distillation Column System.* Industrial & Engineering Chemistry Research, 2004. **43**(9): p. 2160-2174.

130. Arifin, S. and I.L. Chien, *Combined Preconcentrator/Recovery Column Design for Isopropyl Alcohol Dehydration Process.* Industrial & Engineering Chemistry Research, 2007. **46**(8): p. 2535-2543.

131. Fien, G.-J.A.F. and Y.A. Liu, *Heuristic Synthesis and Shortcut Design of Separation Processes Using Residue Curve Maps: A Review.* Industrial & Engineering Chemistry Research, 1994. **33**(11): p. 2505-2522.

132. Huang, Y., R.W. Baker, and L.M. Vane, *Low-Energy Distillation-Membrane Separation Process.* Industrial & Engineering Chemistry Research, 2010. **49**(8): p. 3760-3768.

133. Peshev, D. and A.G. Livingston, *OSN Designer, a tool for predicting organic solvent nanofiltration technology performance using Aspen One, MATLAB and CAPE OPEN.* Chemical Engineering Science, 2013. **104**: p. 975-987.

134. Lipnizki, F., R.W. Field, and P.-K. Ten, *Pervaporation-based hybrid process: a review of process design, applications and economics.* Journal of Membrane Science, 1999. **153**(2): p. 183-210.

135. Marchetti, P., et al., *Molecular Separation with Organic Solvent Nanofiltration: A Critical Review.* Chemical Reviews, 2014. **114**(21): p. 10735-10806.

136. Marchetti, P. and A.G. Livingston, *Predictive membrane transport models for Organic Solvent Nanofiltration: How complex do we need to be?* Journal of Membrane Science, 2015. **476**: p. 530-553.

137. Hickey, P.J. and C.H. Gooding, *Mass transfer in spiral wound pervaporation modules.* Journal of Membrane Science, 1994. **92**(1): p. 59-74.

138. Belaissaoui, B., D. Willson, and E. Favre, *Membrane gas separations and post-combustion carbon dioxide capture: Parametric sensitivity and process integration strategies.* Chemical Engineering Journal, 2012. **211–212**: p. 122-132.

139. Matsumiya, N., et al., *Evaluation of energy consumption for separation of CO2 in flue gas by hollow fiber facilitated transport membrane module with permeation of amine solution.* Separation and Purification Technology, 2005. **46**(1–2): p. 26-32.

140. Joshi, R.K., et al., *Precise and Ultrafast Molecular Sieving Through Graphene Oxide Membranes.* Science, 2014. **343**(6172): p. 752-754.

141. Cséfalvay, E., et al., *Experimental data based modelling and simulation of isopropanol dehydration by pervaporation.* Desalination, 2008. **229**(1–3): p. 94-108.

142. Verweij, H., *Inorganic membranes.* Current Opinion in Chemical Engineering, 2012. **1**(2): p. 156-162.

143. Frankberg, E.J., et al., *Measuring Synthesis Yield in Graphene Oxide Synthesis by Modified Hummers Method.* Fullerenes, Nanotubes and Carbon Nanostructures, 2014. **23**(9): p. 755-759.

144. Botas, C., et al., *The effect of the parent graphite on the structure of graphene oxide.* Carbon, 2012. **50**(1): p. 275-282.

145. Sun, X., et al., *Grafting of graphene oxide with poly(sodium 4-styrenesulfonate) by atom transfer radical polymerization.* Materials Chemistry and Physics, 2013. **138**(2–3): p. 434-439.

146. Zhang, L., et al., *Size-controlled synthesis of graphene oxide sheets on a large scale using chemical exfoliation.* Carbon, 2009. **47**(14): p. 3365-3368.

147. Li, Y., et al., *The effect of the ultrasonication pre-treatment of graphene oxide (GO) on the mechanical properties of GO/polyvinyl alcohol composites.* Carbon, 2013. **55**: p. 321-327.